

Lehrstuhl E15
Univ.-Prof. Dr. F. von Feilitzsch
Institut für Astro-Teilchenphysik
der Technischen Universität München

Study On Neutron-Induced Background in the Dark Matter Experiment CRESST

Hesti R.T. Wulandari

Vollständiger Abdruck der von der Fakultät für Physik der Technischen
Universität München zur Erlangung des akademischen Grades eines

Doktors der Naturwissenschaften

genehmigten Dissertation.

Vorsitzender: Univ.-Prof. Dr. M. Drees
Prüfer der Dissertation: 1. Univ.-Prof. Dr. F. von Feilitzsch
 2. Univ.-Prof. Dr. N. Schmitz, em.

Die Dissertation wurde am 13.06.03 bei der Technischen Universität München
eingereicht und durch die Fakultät für Physik am 09.07.03 angenommen.

To Ageng

Overview

*There are more things in heaven and on earth, Horatio,
than are dreamt of in your philosophy.
- Hamlet -*

The mystery of dark matter dates back to the 1930s, when astronomer Fritz Zwicky found that rotation rates of galaxies were much higher than expected from their estimated masses. He concluded that the only way to explain those high rotation rates was that the galaxies were much more massive than estimated because of the existence of invisible, dark matter (or better: dark component).

Today, 70 years after Zwicky's observation, dark matter remains a mystery. A host of observational data suggests and supports its existence. We are quite sure now, that almost 70% of the dark component is not in the form of matter at all but in the form of so-called dark energy instead. We also know that only a small part of the dark matter consists of baryons, and that this non-baryonic dark matter is "cold" - non relativistic at the time matter began to dominate the energy density of the Universe. But dark matter has not yet been detected (at least not yet in a convincing, undisputable way) and its nature remains unknown.

Although not easy, looking for this invisible matter is worthwhile. The discovery of dark matter will not only reveal its nature and help us understand the evolution of the Universe, but also provide much information about physics beyond the Standard Model of particle physics. Therefore, a large number of experiments have been devoted and are being planned to search for this challenging dark matter.

Among many proposed candidates, the WIMP is the favorite one. In direct searches for WIMPs, neutrons are a particularly important background source because they produce the same signals as WIMPs do. The use of light-phonon detector in the second phase of CRESST, which enables discrimination between electron recoils and nuclear recoils, will leave neutron flux in Gran Sasso as the main background for the experiment. This neutron background will in turn limit the sensitivity of the experiment.

It is obvious that CRESST II and other current and future direct dark matter searches have to cope with neutron background to reach high sensitivity. Understanding neutron background and the way to overcome it, is hence very crucial for the current and next generations of direct search

experiments.

There are two major sources for neutrons underground, namely the local radioactivity and cosmic-ray muons. Neutrons associated with the local radioactivity are produced by fission and (α, n) reactions due to uranium and thorium activities in the surrounding rock and concrete. Low energy neutrons can also be induced by spontaneous fission of ^{238}U in the shielding material and in the setup. High energy neutrons are produced by muons in the rock and in the shielding material (especially lead).

The present work is devoted to study all possible sources of neutron background relevant for CRESST. To perform this task modifications of several Monte Carlo codes and developments of tools have been done, which enable calculation and simulation of neutron production from different sources, transport of these neutrons down to the detector level and finally produce the recoil spectra. This thesis is presented in the following order:

The first Chapter will discuss the existence of dark matter and dark energy, candidates for dark matter, techniques of dark matter detection, and results of several current experiments.

The detection concept of CRESST, the experimental setup in the Gran Sasso underground laboratory and the current status of the CRESST experiment will be explained in Chapter 2.

In Chapter 3, background induced by low energy neutrons will be discussed. Calculation of neutron production rate in the surrounding rock and concrete, the expected flux at the experimental site and the estimation of background induced by low energy neutrons in the CRESST setup will be presented. In addition, discussion on neutrons from fission reaction in the shielding material will also be covered.

Chapter 4 is devoted to background induced by high energy neutrons produced by muons in the rock and in the experimental setup. This chapter starts with a general description of muons, their origins, interactions with matter, muons underground, mechanism of neutron production, and results of measurements. Then, muon-induced neutrons and simulations in relevance with the CRESST experiment are discussed.

In Chapter 5, the long term perspective of the CRESST experiment will be presented. Some future experiments will also be briefly discussed.

Finally, results of the present work will be summarized in Chapter 6. Contributions of neutrons from different origins are compared to show the level of danger they may cause. Some suggestions to overcome the problems caused by neutron background are presented.

H.R.T. Wulandari
May, 2003

Zusammenfassung

CRESST sucht mit Hilfe von Tieftemperatur-Detektoren nach WIMPs (Weakly Interacting Massive Particles) als Kandidaten für die Dunkle Materie im Universum. Für die zweite Phase von CRESST werden neue Detektoren verwendet, die eine deutliche Unterscheidung zwischen Elektron- und Kernrückstößen durch simultanes Messen von Phononen und Szintillationslicht ermöglichen. Jedoch induzieren auch Neutronen, so wie WIMPs, Kernrückstöße, weshalb der Neutronenuntergrund nicht unterdrückt werden kann und so die Sensitivität des Experimentes begrenzen würde.

Neutronen werden durch Radioaktivität und Myonen im umgebenden Gestein und in der Abschirmung produziert. Das Ziel der vorliegenden Arbeit war die Anpassung und Erweiterung von Simulations-Programmen, die eine Analyse der verschiedene Neutronenquellen bezüglich der Erzeugung von Rückstoßsignalen in den Detektoren von CRESST erlauben. Die wesentlichen Quellen des Neutronenuntergrundes sollten damit untersucht werden. Zur Bestimmung des Neutronenuntergrundes wurde die Neutronenproduktion durch verschiedene Quellen simuliert oder abgeschätzt, danach diese Neutronen in Computersimulationen bis zu den Detektoren transportiert und die Erzeugung von Rückstoßsignalen untersucht. Dazu war die Kombination und Erweiterung von verschiedenen Simulations-paketen wie MCNP und FLUKA notwendig. Keines der üblichen Simulationspaket kann Neutronen in allen für die Untersuchungen notwendigen Energiebereichen bearbeiten und es existiert keines, das auf die Analyse von Rückstoßenergien vorbereitet ist.

Es wurde festgestellt, dass schon im Bereich der heutigen Sensitivität von einigen 10^{-6} pb für den Wirkungsquerschnitt für spinunabhängige Wechselwirkung zwischen WIMP und Proton mit Neutronenuntergrund zu rechnen ist. Ohne Neutronenabschirmung könnte CRESST II seine Ziele daher nicht erreichen.

Mit einer 50 cm dicken Schicht aus Polyethylen als Neutronenmoderator können niederenergetische Neutronen aus dem umgebendes Gestein bis zu einem Faktor 1000 unterdrückt werden. Es fangen dann aber Neutronen aus anderen Quellen (vor allem Neutronen, die durch Myonen in der

Abschirmung erzeugt werden) an, den Untergrund zu dominieren. Die Sensitivität wäre auf etwa 10^{-7} pb begrenzt und würde die Ziele der zweiten Phase von CRESST von einigen 10^{-8} pb gefährden, weshalb auch ein Myon-Veto benötigt wird. Allerdings wird ein Myon-Veto nur wirksam, wenn die Neutronen aus den anderen Quellen beseitigt werden können. Es ist zu erwarten, dass der durch hochenergetische Neutronen im umgebenden Gestein induzierte Untergrund wird reduziert werden kann, wenn Mehrfachstreuung berücksichtigt wird. Auch dies sollte in Zukunft mit den in dieser Arbeit bereit gestellten Simulationswerkzeugen möglich sein.

Es ist offensichtlich, dass der Schutz gegen den von Neutronen induzierten Untergrund eines der Schlüsselthemen der zukünftige Experimente ist. Deshalb wird dieses Thema zur Zeit intensiv in vielen Arbeitsgruppen studiert, auch in ETNO μ siq (European Team for Neutron and μ Simulation and Qualification), die aus den CRESST-, EDELWEISS- und UKDM- Kollaborationen besteht.

Contents

<i>Overview</i>	iii
<i>Zusammenfassung</i>	v
1. Dark Matter Problems	1
1.1 Ω and Cosmology	1
1.2 Determinations of Ω_m and Λ : Observational Evidence for Dark Matter and Dark Energy in the Universe	3
1.2.1 Luminosity Density x M/L	4
1.2.1.1 Mass Density in the Solar Neighborhood	4
1.2.1.2 Rotation Curves and Dark Matter in Galaxies	4
1.2.1.3 Dark Matter in Clusters of Galaxies	4
1.2.2 Baryonic Fractions in Galaxy Clusters	5
1.2.3 Large Scale Velocity Flows	6
1.2.4 Power Spectrum of Mass Inhomogeneity	6
1.2.5 Cosmic Microwave Background (CMB) Anisotropy . .	7
1.2.6 Type Ia Supernova Hubble Diagram	7
1.2.7 Summary of the Evidence for Dark Matter and Dark Energy	8
1.3 Dark Matter Candidates	8
1.3.1 Baryonic Candidates	8
1.3.2 Non-baryonic Candidates	9
1.3.2.1 Hot Dark Matter	9
1.3.2.2 Cold Dark Matter	10
1.4 WIMP Detection	12
1.4.1 Indirect Detection	12
1.4.2 Direct Detection	12
1.4.2.1 Elastic Scattering Cross Section	13
1.4.2.2 Expected Event Rate and Energy Spectrum .	14
1.4.2.3 Current Experiments	17
1.4.2.4 Neutron Background	20

2.	The CRESST Experiment	23
2.1	Detection Concept	23
2.2	CRESST Setup at LNGS	26
2.3	Results of CRESST Phase I	28
2.4	CRESST Phase II	31
3.	Background Induced by Low Energy Neutrons	35
3.1	Neutron Flux Measurements at LNGS	35
3.2	Calculation and Simulation of the Low Energy Neutron Flux from Fission and (α,n) Reactions in the Surrounding Rock/Concrete	38
3.2.1	Neutron Production by Spontaneous Fission	38
3.2.2	Neutron Production by (α,n) Reactions	39
3.2.3	Flux of Low Energy Neutrons at LNGS	46
3.3	Neutron Background in the Current Setup of CRESST: The Need for Neutron Shielding	48
3.3.1	MCNP4B and Recoil Spectrum	48
3.3.2	Neutron Background Expectation in CRESST I and in CRESST II without Neutron Moderator	49
3.4	Neutron Moderator	51
3.4.1	Efficiency of Shielding and Alternatives	51
3.4.2	Simulation with a Realistic Setup	54
3.5	Water Content Variation	55
3.6	Neutrons Produced by Fission in the Lead Shield	57
4.	Muon-induced Neutron Background	59
4.1	Muons and Cosmic Rays	59
4.2	Interactions of Muons with Matter	61
4.2.1	Ionization	61
4.2.2	Bremsstrahlung	62
4.2.3	Direct e^+e^- Pair Production	63
4.2.4	Photonuclear Interactions (Deep Inelastic Scattering with Nuclei)	64
4.3	Muons Underground	65
4.3.1	Vertical Muon Intensity	66
4.3.2	Local Muon Energy and Intensity at LNGS	68
4.4	Muon-induced Neutrons Underground	69
4.5	High Energy Neutrons Induced by Muons in the LNGS Rock (Dementyev's Spectrum)	71
4.5.1	Spectrum of Neutrons Entering the Experimental Hall	71
4.5.2	Count Rates Obtained with the Dementyev's Spectrum	73
4.6	Full Simulations of Muon-induced Neutrons for CRESST . .	78
4.6.1	Monte Carlo Codes Used for the Simulations	78

4.6.2	Muon Flux and Energy Spectrum	79
4.6.3	Simulations of Muon-induced Neutrons	80
4.6.4	Energy Spectrum of Neutrons Entering the LNGS Hall	84
4.6.5	Effect of Shielding Materials	88
4.6.6	Recoil Spectrum and Count Rate	89
4.6.6.1	Recoil Spectrum and Count Rate Induced by High Energy Neutrons from the Rock	90
4.6.6.2	Recoil Spectrum and Count Rate Induced by Neutrons Produced by Muons in the Experimental Setup	91
5.	The Long Term Perspective for CRESST and Future Experiments	93
5.1	Long Term Perspective for CRESST	93
5.2	Upgrading of Current Experiments	95
5.3	Future Direct Detection Projects	95
6.	Summary and Outlook	99
	<i>List of Figures</i>	105
	<i>List of Tables</i>	109
	<i>Bibliography</i>	111
	<i>Acknowledgments</i>	121

Chapter 1

Dark Matter Problems

The determination of the value and composition of the energy density of the Universe is the central problem of modern cosmology. It has been suggested since decades by observational results that the dominant component of the Universe is “dark”, *i.e.* does not emit or absorb electromagnetic radiation. The existence of this dark component is observed by its gravitational effects. There is overwhelming evidence from cosmological observation for their existence, ranging from small galaxies to the Universe as a whole. Furthermore, observations in the last twenty years strongly support the idea that almost all of dark matter is non baryonic and a large number of candidates has been proposed. Arguments have even been put forward since the last couple of years, that a large fraction of the dark component of the energy density in the Universe is not in the form of matter at all, but instead in the form of vacuum energy density (“dark energy”).

This chapter covers the evidence for the existence of dark matter and dark energy, candidates for dark matter, techniques of dark matter detection, and results of several current experiments.

1.1 Ω and Cosmology

In the standard cosmological model the evolution of the Universe is described by the Friedmann-LeMaître equations:

$$\left(\frac{\dot{R}}{R}\right)^2 \equiv H^2 = \frac{8\pi G}{3}\rho_m - \frac{k}{R^2} + \frac{\Lambda}{3} \quad (1.1)$$

$$\frac{\ddot{R}}{R} = -\frac{4}{3}\pi G(\rho_m + 3p) + \frac{\Lambda}{3} \quad (1.2)$$

where R is the cosmic scale factor in the Robertson-Walker metric, H is the Hubble parameter that indicates the expansion rate of the Universe, ρ_m and p are the matter density and pressure respectively, k is the curvature radius, and Λ is the cosmological constant.

At the present epoch $H = H_0$ and Eq. (1.1) can be rewritten as:

$$\frac{k}{H_0^2 R^2} = \Omega_m + \Omega_\Lambda - 1 \quad (1.3)$$

with

$$\Omega_m = \rho_m / \rho_c, \quad \Omega_\Lambda = \frac{\Lambda}{3H_0^2} \quad (1.4)$$

The critical density has been defined as:

$$\rho_c = \frac{3H_0^2}{8\pi G} \quad (1.5)$$

The value of the critical density is $\rho_c = 1.88 \times 10^{-29} \text{ g cm}^{-3} h^2$, where $h = H_0 / (100 \text{ km s}^{-1} \text{ Mpc}^{-1})$. The Hubble parameter has been measured with different methods and the results are in the range of $0.6 \lesssim h \lesssim 0.8$. The first WMAP (Wilkinson Microwave Anisotropy Probe, the new name for MAP) measurements of the age of the Universe and $\Omega_m h^2$ yield $H_0 = 71^{+4}_{-3} \text{ km s}^{-1} \text{ Mpc}^{-1}$ [Ben03], which is consistent with the Hubble Space Telescope (HST) Key Project value of $H_0 = 72 \pm 3 \pm 7 \text{ km s}^{-1} \text{ Mpc}^{-1}$ [Fre01]. Most of the methods use distance ladders (both traditional ladders like cepheids and RR Lyr or secondary ladders like type Ia SNe, surface brightness fluctuation (SBF) in galaxy images and the Tully-Fischer relation) and take the distance to the Large Magellanic Cloud (LMC) to be 50 kpc ($m - M = 18.5$) as the zero point. Here $m - M$ is the distance modulus, where m is the apparent magnitude of an object and M is the absolute magnitude (magnitude at 10 pc). Before 1997 few doubts were cast on the distance to LMC. But Hipparcos astrometric satellite revealed that the distance to LMC was more uncertain (20% in distance) than what was thought, and therefore introducing new uncertainties into the determination of H_0 (see discussion in [Hag02]). However, recent measurements using techniques called “physical methods” (e.g. gravitational lens timing, Sunyaev-Zeldovich (SZ effect)), which allow distance estimates without depending on astronomical ladders, yield independent estimates that are consistent with the range obtained with distance ladders, but with larger uncertainties at present. In this work, the value of $h = 0.71$ is used when a numerical value is needed in the discussion.

The total density parameter of the Universe today, $\Omega = \Omega_m + \Omega_\Lambda$, is directly related to its present curvature. There are three possible cases:

$k = +1$	\longleftrightarrow	$\Omega > 1$	closed Universe
$k = 0$	\longleftrightarrow	$\Omega = 1$	flat Universe
$k = -1$	\longleftrightarrow	$\Omega < 1$	open Universe

At the present time $p = 0$ and Eq. (1.2) can be rewritten as:

$$\frac{\ddot{R}}{H_0^2 R} = -\frac{\Omega_m}{2} + \Omega_\Lambda \quad (1.6)$$

The two cosmological equations, *i.e.* Eq. (1.1) and Eq. (1.2), together with the values of Ω_m and Ω_Λ determine the ultimate fate of the Universe. For $\Lambda = 0$, the acceleration (Eq. (1.6)) is always negative or the expansion of the Universe is always slowing down. If $k \leq 0$ then $H^2 > 0$ for all time, which means that flat and open universes expand forever. Consider now the case $\Lambda \neq 0$. For $\Lambda > 0$, Ω_Λ gives positive acceleration in Eq. (1.6). Flat and open universes expand forever, because $H^2 > 0$ for all time (see Eq. (1.1)). For a closed Universe, the cosmological constant term can dominate if $|k/R^2|$ is small enough (the Universe is not too closed) before the Universe can reach the turnaround point. So, there are closed universes that expand forever. On the contrary, if the Universe does reach the turnaround point, it continues to collapse because the cosmological constant term becomes less important as R becomes small again (see Eq. (1.1)). Negative Λ is not discussed here, because there appears to be no observational evidence for it.

1.2 Determinations of Ω_m and Λ : Observational Evidence for Dark Matter and Dark Energy in the Universe

As discussed in the previous section, the Hubble constant H_0 , the mass density parameter Ω_m and the cosmological constant Λ set the scale and characterize the mass-energy content and curvature of the Universe. For zero curvature (flat Universe) $\Omega_m + \Omega_\Lambda = 1$. The case with $\Omega_m = 1$ and $\Omega_\Lambda = 0$ is referred to as the Einstein-de Sitter (EdS) Universe. All simple inflationary models predict that the Universe is flat, *i.e.* that $\Omega = \Omega_m + \Omega_\Lambda = 1$. Since there is no known physical reason for a non-zero cosmological constant, it was often said that inflation favors $\Omega = 1$.

Big Bang Nucleosynthesis (BBN) gives a limit on the average baryonic content of the Universe. To agree with the measured abundances of helium, deuterium, and lithium, the baryonic content of the Universe must be between $0.018 \lesssim \Omega_b h^2 \lesssim 0.022$ [Tur99]. Given $h = 0.71$ this means $\Omega_b \simeq 0.04$.

In these sections several methods to determine Ω_m and Λ will be discussed in order to show observational evidence for the existence of dark matter and dark energy.

1.2.1 Luminosity Density $\times M/L$

Most determinations of Ω_m are made by measuring the mass-to-light ratio M/L of some systems and then multiply it by the average luminosity density of the Universe \mathcal{L}_B (see discussion in [Bot98]):

$$\Omega_m \equiv \frac{\rho_m}{\rho_c} = \frac{(M/L)\mathcal{L}_B}{\rho_c} = \frac{h^{-1}}{1500} \frac{M/L}{M_\odot/L_\odot} \quad (1.7)$$

where $\rho_c = 2.8 \times 10^{11} h^2 M_\odot \text{Mpc}^{-3}$ and $\mathcal{L}_B = (1.9 \pm 0.1) \times 10^8 h L_\odot \text{Mpc}^{-3}$ is the average luminosity density in the B-band. The use of this determination to get mass density at different scales is described below.

1.2.1.1 Mass Density in the Solar Neighborhood

In the solar neighborhood $M/L \approx 5 M_\odot/L_\odot$, giving $\Omega_{lum} = 0.003 h^{-1} = 0.004$ (for $h = 0.71$). If the solar neighborhood is typical, then the amount of luminous matter (stars, dust, and gas) is far below the critical value.

1.2.1.2 Rotation Curves and Dark Matter in Galaxies

The velocities of neutral hydrogen clouds as a function of the distance from the center of the galaxy can be measured by using the Doppler shift in their 21 cm emission lines. Persic and Salucci [Sal97] have collected the rotation curves of around 1000 spiral galaxies. In almost all cases, after a rise near $r = 0$, the velocities remain constant as far as can be measured. A typical rotation curve of a spiral galaxy is shown in Figure 1.1.

By Newton's law for circular motion the velocity as a function of r is:

$$v(r) = \sqrt{\frac{GM(r)}{r}} \quad (1.8)$$

where $M(r) = 4\pi \int_0^r r'^2 \rho(r') dr'$. If all matter follows the distribution of visible matter, then after r becomes greater than the extent of the mass, one expects the velocity to drop $\propto r^{-1/2}$. But $v(r) \sim \text{constant}$ implies mass $M(r) \propto r$ and density $\rho(r) \propto r^{-2}$, which can be obeyed if an additional spherically symmetric halo component is assumed. Clearly, the flat rotation curves imply the existence of a dark matter component. In the halo [Bot98] M/L is about $70 h M_\odot/L_\odot R_{halo}/100 \text{kpc}$, where $40 \text{kpc} \leq R_{halo} \leq 100 \text{kpc}$. Then we get $\Omega_{halo} \sim 0.04 R_{halo}/100 \text{kpc}$. This provides evidence for dark matter at the level of individual galaxies.

1.2.1.3 Dark Matter in Clusters of Galaxies

The Mass-to-light ratio in clusters of galaxies can be derived from X-ray emission by hot gas in intra cluster plasma [Bri92], from strong gravitational lensing [Tys95], and from velocity dispersion of the galaxies [Whi93].

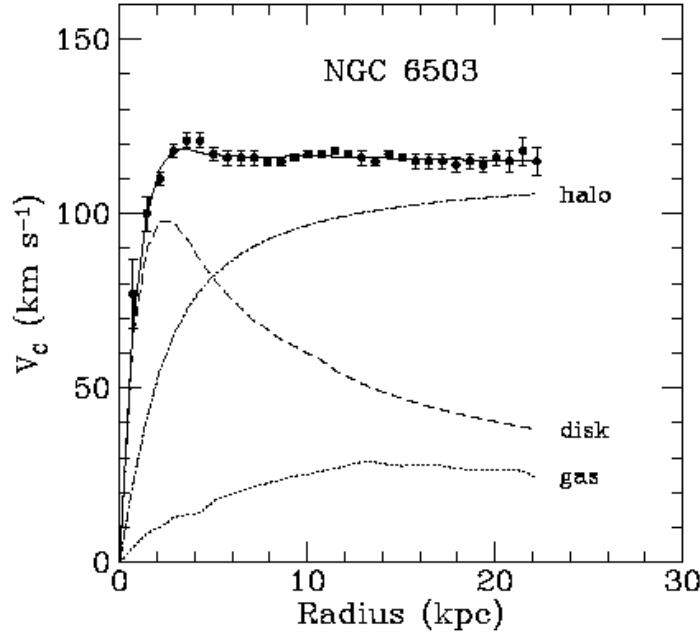


Fig. 1.1 Rotation curve for the spiral galaxy NGC6503. The points are the measured circular rotation velocities as a function of the distance from the center of the galaxy. The dashed and dotted curves are the contribution to the rotational velocity due to the observed disk and gas respectively, and the dot-dashed curve is the contribution from the dark halo.

For rich clusters of galaxies with masses $\sim (10^{14} - 10^{15})h^{-1}M_\odot$, like the Coma Cluster [Whi93], within $1.5h^{-1}\text{Mpc}$ radius M/L is about $(300 \pm 100)hM_\odot/L_\odot$, providing $\Omega_{\text{cluster}} \simeq 0.20 \pm 0.07$.

1.2.2 Baryonic Fractions in Galaxy Clusters

The baryon-to-matter ratio in clusters can be determined by X-ray measurements alone and by measurements of the Sunyaev-Zeldovich (SZ) distortion of the cosmic microwave background (CMB) combined with X-ray measurements [Tur02]. For X-ray measurement alone Mohr *et al.* [Moh98] for example determined the cluster baryon fraction from a sample of 45 clusters as $\Omega_b/\Omega_{\text{cluster}} = (0.07 \pm 0.007)h^{-3/2}$. The determination of the baryonic fraction with SZ/X-ray measurement is for example given by Grego *et al.* [Gre01] as $\Omega_b/\Omega_{\text{cluster}} = (0.08 \pm 0.01)h^{-1}$. Primordial nucleosynthesis limits $\Omega_b \lesssim 0.02h^{-2}$, so that $\Omega_{\text{cluster}} \lesssim 0.3$ (for $h = 0.71$).

1.2.3 Large Scale Velocity Flows

To get the sample which is representative of the entire Universe, it would be best to measure the amount of dark matter on the largest possible scale. An example comes from the observation of the local group of galaxies moving at the speed of $627 \pm 22 \text{ km s}^{-1}$ with respect to the cosmic microwave background (CMB).

Interpreting this effect as due to gravity, the velocity is oriented toward the regions of excess of matter. Thus, taking into account the expansion of the Universe, one has

$$v \propto \Omega_m^{0.6} \frac{\delta\rho}{\rho} = \frac{\Omega_m^{0.6}}{b} \frac{\delta n}{n}$$

where the factor $\Omega_m^{0.6}$ is due to expansion, and the linear bias factor b has been introduced to relate the observed excess in galaxy number counts $\delta n/n$ to the excess in mass density $\delta\rho/\rho$. Using galaxy counts from the IRAS satellite surveys, Yahil *et.al.* [Yah86] find that the direction of the $\delta n/n$ excess agrees with the direction of the velocity vector to within about 20 degrees, and that $\beta \equiv \Omega_m^{0.6}/b = 0.9 \pm 0.2$. The problem with this technique, which is also known as peculiar velocity technique, is that an accurate value of Ω_m will not be obtained unless the mass distribution is surveyed to a volume sufficiently large to include all the inhomogeneities that give rise to the peculiar velocity. The present limit on β is 0.5 to 0.9, which give $\Omega_m = 0.3$ to 0.8 if no biasing is assumed [Dek99].

1.2.4 Power Spectrum of Mass Inhomogeneity

The simplest model for the generation of cosmic structure is gravitational perturbation. This perturbation of density is described by the Fourier power spectrum. The shape of the power spectrum depends upon $\Omega_m h$ and Ω_b/Ω_m . It can be measured by weak-gravitational lensing and through the distribution of galaxies (redshift surveys).

Currently, the best determination of the parameters $\Omega_m h$ and Ω_b/Ω_m comes from an analysis of 160,000 redshifts in the 2-degree Field Galaxy Redshift Survey (2dFGRS) [Per01]. The numbers reported by 2dFGRS are consistent with the early result from the Sloan Digital Sky Survey (SDSS), $\Omega_m h = 0.19 \pm 0.04$ [Dod01], which give $\Omega_m \approx 0.3$ with $h = 0.71$. No significant result on the Ω_b/Ω_m is reported at the moment. Significant improvement in both $\Omega_m h$ and Ω_b/Ω_m can be expected when 2dFGRS and SDSS have analyzed all their samples of 250,000 and 600,000 redshifts respectively.

1.2.5 Cosmic Microwave Background (CMB) Anisotropy

The structure of the acoustic peaks in the CMB angular power spectrum depends upon the total density and the baryon density. The ratio of the heights of odd to even peaks, particularly the ratio of the height of the first to the second peak, pins down the baryon density (see for example [Hu97]). The position of the first peak is particularly sensitive to the total density Ω . The position of the first peak as estimated using CMBFAST [Sel96] is:

$$\ell_1 \approx 220 \left(\frac{1 - \Omega_\Lambda}{\Omega_m} \right) \quad (1.9)$$

This means that the position of the acoustic peak is at $\ell \approx 220$ if $\Omega_m + \Omega_\Lambda = 1$, but it shifts to a high ℓ as $\Omega_m^{-1/2}$ if $\Omega_\Lambda = 0$.

Recent experimental results from balloon flights Boomerang [Net02] and MAXIMA [Lee01], the new generation of interferometric experiments DASI [Hal01] and CBI [Pad01], and the WMAP satellite [Ben03] have dramatically improved the power spectrum measurements. It is now clear that the spectrum as a whole possesses the series of acoustic peaks which are expected for adiabatic-type perturbations.

Boomerang's reported constraint on the total density $\Omega = 1.02 \pm 0.06$ [Net02] implies that the Universe is close to flat. Limits from MAXIMA [Sto01] and DASI [Pry02] are similar. The first result from WMAP is $\Omega = 1.02 \pm 0.02$ [Ben03]. Boomerang reported a baryon density of $\Omega_b h^2 = 0.022 \pm 0.004$, while the best fit value of WMAP is $\Omega_b h^2 = 0.0224 \pm 0.0009$ [Ben03], both consistent with the prediction of big bang nucleosynthesis. The best fits of those experiments are close to the Λ -dominated cold dark matter model and consistent with independent observations indicating that the matter density $\Omega_m \simeq 0.3$. For example, WMAP's best fit is $\Omega_m \simeq 0.27 \pm 0.04$ and $\Omega_\Lambda \simeq 0.73 \pm 0.04$ [Ben03].

1.2.6 Type Ia Supernova Hubble Diagram

Type Ia supernovae can be used as standard candles to get information on the relationship between redshift and distance (Hubble diagram). This standard candle test is applied by the Supernova Cosmology Project [Per99] and the High-z Supernova Search [Rie98]. The results of these two projects constrain the combination of Ω_m and Ω_Λ as

$$0.8 \Omega_m - 0.6 \Omega_\Lambda \simeq -0.2 \pm 0.1 \quad (1.10)$$

Under the assumption of a flat Universe, the Supernova Cosmology Project reported $\Omega_m = 0.28^{+0.10}_{-0.09}$ (stat.) $^{+0.05}_{-0.04}$ (syst.) [Per99], while the High-z Supernova Search result gives $\Omega_m = 0.28 \pm 0.10$ (stat.) [Rie98].

1.2.7 *Summary of the Evidence for Dark Matter and Dark Energy*

Different methods to determine Ω_m and Ω_Λ show convergent results now. They tell us that the Universe is flat and that dark energy is the dominant constituent. The status of matter densities is summarized below (with $0.6 \lesssim h \lesssim 0.8$):

Luminous matter (stars, gas, dust):

$$\Omega_{lum} \lesssim 0.01$$

Baryonic matter:

$$0.03 \lesssim \Omega_b \lesssim 0.06$$

Data from a host of observational data point to:

$$0.2 \lesssim \Omega_m \lesssim 0.4$$

The limits above show that matter consists mainly of non-luminous matter (dark matter). A small part of this dark matter is baryonic, but most of it is non-baryonic. In the following section, candidates for dark matter will be discussed.

1.3 Dark Matter Candidates

A large number of candidates for dark matter has been proposed with masses ranging from 10^{-5} eV = 1.8×10^{-41} kg = $9 \times 10^{-72} M_\odot$ (axions) up to $10^4 M_\odot$ (black holes). In this section the problems of baryonic and non-baryonic dark matter and several possible candidates for both cases are discussed.

1.3.1 *Baryonic Candidates*

The most popular baryonic candidates are the Massive Compact Halo Objects (MACHOs). These include brown dwarfs, jupiters, white dwarfs, neutron stars and black holes. Brown dwarfs are spheres of H and He with masses below $0.08 M_\odot$, too small to begin hydrogen burning. Jupiters are similar, but with masses $\sim 10^{-3} M_\odot$. White dwarfs, neutron stars and black holes are remnants of early generations of massive stars.

The experiments MACHO [Alc00], EROS [Ren97] and OGLE [Uda97] employed the technique of microlensing to look for MACHOs at $z \sim 0$ towards the Large Magellanic Cloud (LMC), the Small Magellanic Cloud (SMC), and the galactic bulge. All three experiments have detected events. The results show that MACHOs with masses from $10^{-6} M_\odot$ to $0.1 M_\odot$ are not a significant component of our Galaxy's halo. An all-MACHO halo is ruled out at 95% CL [Alc00]. However, the results also indicate that

MACHOs with masses of approximately $0.4M_{\odot}$ comprise roughly 20% of the total mass of the halo. A region with 68% CL extends from $0.2M_{\odot}$ to $0.9M_{\odot}$ [Alc00b], which is strange, because such objects should be luminous.

A population of white dwarfs has been observed in the halo of our Galaxy [Iba99] and is proposed as a candidate for dark matter, but there are problems with this scenario. For example, the star formation rate required to produce them is much higher than normally measured. Fields [Fie00] and Graff [Gra99] gave the bound on the contribution of white dwarf MACHOs to the baryon density as $\Omega_{WD} \lesssim 0.006h^{-1}$.

At high redshift a possible candidate is neutral hydrogen uniformly distributed or clumped in clouds in the intergalactic medium. Both give a very small fraction of baryons in the form of neutral hydrogen of order of $10^{-7} - 10^{-6}$ of the critical density (see discussion in [Gol01]).

1.3.2 Non-baryonic Candidates

The non-baryonic candidates are basically elementary particles which are either not yet discovered or have non-standard properties. Non-baryonic dark matter candidates are categorized into two groups: hot dark matter (HDM) and cold dark matter (CDM), according to whether they would be still relativistic or already non-relativistic at the time of entering the epoch of matter dominance.

1.3.2.1 Hot Dark Matter

The typical HDM candidates are neutrinos. The contribution of neutrinos to non-baryonic dark matter depends on neutrino mass. The present mean number density plus their partner ($\bar{\nu}$) in one family is $n_{\nu} = 113$ neutrinos cm^{-3} [Pee93]. If the neutrino rest mass in this family is m_{ν} , the mean mass density is $n_{\nu}m_{\nu}$. Taking into account contributions of all families, the density parameter Ω_{ν} is

$$\Omega_{\nu} = \frac{8\pi G}{3H_0^2} n_{\nu} \Sigma m_{\nu_i} = \frac{\Sigma m_{\nu_i}}{93eV} h^{-2} \quad (1.11)$$

For $\Omega_{\nu} = 1$ and $h = 0.71$ neutrino mass should be ~ 50 eV.

There is good motivation for non-zero neutrino mass from neutrino experiments. The global analysis of all solar neutrino experiments combined with CHOOZ and KamLAND data [Fog03] gives a neutrino mass square difference of Δm_{21}^2 in the range of $(0.6 - 0.8) \times 10^{-4} \text{ eV}^2$ (90% C.L.), with the best fit $0.7 \times 10^{-4} \text{ eV}^2$. The atmospheric neutrino experiment Superkamiokande gives $\Delta m_{32}^2 \sim 2.5 \times 10^{-3} \text{ eV}^2$ [Shi02]. A consistent picture for normal mass hierarchy scenario would be $m_1 = 0$, $m_2 \simeq 0.008 \text{ eV}$ and $m_3 \simeq 0.05 \text{ eV}$, which is not of particular cosmological interest. The LSND experiment claims Δm_{21}^2 in the range of 0.2 eV^2 to 15 eV^2 . The normal mass hierarchy

scenario would give a massless or nearly massless ν_1 and degenerate ν_2 and ν_3 with mass between 0.45 eV and 3.9 eV. A large part of the LSND 90% confidence level is excluded by the KARMEN experiment [Eit00], but a mass between 0.45 eV and 1.5 eV is still permitted. The MiniBooNe experiment will be able to test the whole LSND allowed region [Baz99].

1.3.2.2 Cold Dark Matter

In the CDM sector, the most plausible candidates are the so called *Weakly Interacting Massive particles* (WIMPs) and the axions. The WIMP term includes any neutral, massive (between a few GeV and a few TeV for thermal relics), and weakly interacting particles. The favorite WIMPs for CDM candidates are neutralinos. There are some other WIMPs which are less prominent like axinos, gravitinos, etc.

Axions

The axion is a very light pseudoscalar particle which gives a natural and beautiful solution to the CP violation problem in the strong interaction [Pec77]. The axion mass is given in terms of f_a (the scale of Peccei-Quinn symmetry breaking) by

$$m_a \simeq 6\mu\text{eV} \frac{10^{12}\text{GeV}}{f_a} \quad (1.12)$$

A priori the value of f_a is arbitrary and hence, that of m_a . The choice of $f_a = 10^{12}\text{GeV}$ gives $m_a \sim 10^{-5}\text{GeV}$.

There are three known mechanisms of cosmological production of axions, *i.e.* thermal production, misalignment production, and axionic string decay (see [Kol90] for explanation). Independent of the exact details of their production, axions are a cosmologically interesting dark matter candidate only if they are light. The energy density of axion is

$$\Omega_a \sim \left(\frac{10^{-5}\text{eV}}{m_a} \right)^{1.1} \quad (1.13)$$

Therefore, axions may close the Universe if they have correct mass.

The coupling of the axion with electromagnetic fields is of the form

$$\mathcal{L}_{a\gamma\gamma} \sim \frac{\alpha}{f_a} a \vec{E} \cdot \vec{B} \quad (1.14)$$

which gives an extremely long lifetime for the decay $a \rightarrow 2\gamma$. Here \vec{E} and \vec{B} are the electric and magnetic fields respectively, and α is the fine structure constant. Experiments are underway using the above interaction to transform the axion with an intense magnetic field into a wave in a resonant cavity. The region of axion mass to be searched is from the lowest

estimated over closure bound ($\sim 10^{-6}eV$) to the upper bound set by astrophysical arguments ($\sim 10^{-3}eV$). For discussion on the astrophysical upper limits on axion mass, see for example [Raf95].

Neutralinos

In the Minimal Supersymmetric Standard Model (MSSM) with broken PQ (Peccei-Quinn) symmetry we have five spin 1/2 neutral particles: the wino \widetilde{W}_3 , the bino \widetilde{B} , two Higgsinos (\widetilde{H}_1 and \widetilde{H}_2), and the axino \widetilde{a} . Generally, the Lightest Supersymmetric Particle (LSP) is a linear combination of this five fields (see [Ber97] and references therein)

$$\widetilde{\chi} = C_1 \widetilde{W}_3 + C_2 \widetilde{B} + C_3 \widetilde{H}_1 + C_4 \widetilde{H}_2 + C_5 \widetilde{a}$$

where \widetilde{B} and \widetilde{W}_3 are the supersymmetric partners of the U(1) gauge field B and the third component of the SU(2) gauge field W_3 that mix to make the photon and Z boson. Two extreme cases may occur, dependent on which term is dominant. If the axino state dominates, then the LSP is almost pure axino. Otherwise, if the first four terms are dominant, the LSP is the usual neutralino χ . In order to match the experimental limit on proton decay, it is generally assumed that a multiplicative quantum number called R-parity is conserved, with R=+1 for ordinary particles and R=-1 for their supersymmetric partners. The natural consequence of this is that the LSP is stable, having no R-conserving decay mode.

The neutralino is a neutral Majorana particle ($\overline{\chi} = \chi$). With a unitary relation between the coefficient C_i , the parameter space of neutralino states is described by three independent parameters, *e.g.* mass of the wino M_2 , the mixing parameter of two Higgsinos μ , and the ratio of two vacuum expectation values $\tan\beta = v_2/v_1$.

The phenomenology and cosmology of the neutralino are governed primarily by its mass and composition. The neutralino can be anything from a nearly pure bino to a nearly pure higgsino. A useful parameter for describing the neutralino composition is the gaugino fraction, $f_g = |C_1|^2 + |C_2|^2$ [Gri90]. If $f_g > 0.5$, then the neutralino is primarily gaugino and if $f_g < 0.5$, it is primarily higgsino.

The mass of the LSP is constrained from below by non-detection in accelerators like LEP, and from above by the requirement that supersymmetry fulfils its role of maintaining the mass hierarchy between the GUT scale and the electroweak scale.

Neutralinos could be produced through reactions such as $e^-e^+ \rightarrow \chi\overline{\chi}$. Of course, they can annihilate through the back reaction, $\chi\overline{\chi} \rightarrow e^-e^+$. As long as the temperature $T > m_\chi$, where m_χ is neutralino mass, the neutralino number density would be comparable to the number density of electrons, positrons and photons. However, once T drops below m_χ , the

neutralino abundance begins to drop. It will fall until the neutralino number density is so low that the annihilation rate, $\langle\sigma_A v\rangle n_\chi$, falls below the expansion rate H . This “freeze-out” occurs at a density determined by the neutralino annihilation cross section and implies that

$$\Omega_\chi h^2 \simeq \frac{10^{-37} \text{cm}^2}{\langle\sigma_A v\rangle} \quad (1.15)$$

where $\langle\sigma_A v\rangle$ is the thermally averaged annihilation cross section times the relative velocity. If $\langle\sigma_A v\rangle \sim 10^{-36} \text{cm}^2$ (corresponds to the electroweak scale), it is possible to fit Ω_χ with the expected number for matter density.

1.4 WIMP Detection

Only detection of neutralino WIMPs will be discussed in this section. The local halo density of our Galaxy is estimated to be 0.3 GeV/cm^3 with an uncertainty of a factor of around two [Jun96]. If we take the neutralino WIMPs as dominant component of the halo, the density corresponds to about 3000 LSPs of mass $m_\chi = 100 \text{ GeV}$ per m^3 . With typical velocities in the range of a few hundred km/s, we will get a quite large flux of WIMPs :

$$\Phi = v \rho_\chi / m_\chi \approx 10^9 (100 \text{ GeV}/m_\chi) \chi' \text{s/m}^2/\text{s} \quad (1.16)$$

Several techniques have been developed to detect WIMPs , but basically they can be categorized into two basic strategies: indirect and direct detections.

1.4.1 *Indirect Detection*

Indirect searches look for particles produced by WIMP pair-annihilation in the Galactic halo such as antiprotons, positrons and photons (*e.g.* MACRO, Baksan, Kamiokande and Soudan experiments) or multi-GeV energy neutrinos coming from the Sun and/or the core of the Earth (*e.g.* Baikal, AMANDA, ANTARES, NESTOR). The latter are detected *via* their conversion to muons, thus the signatures are the so called upward-going muons. A new way of looking for WIMPs at the Galactic center was also proposed. If there is a super-massive black hole in the Galactic center as is now suggested by some evidence, it will accrete WIMPs and increase their density in the core. They annihilate then more effectively and produce a much higher flux of neutrinos, photons and other products from the Galactic center [Gon99].

1.4.2 *Direct Detection*

Direct searches look for WIMP elastic scattering off nuclei, $\chi N \rightarrow \chi N$, in a detector. The main observable is the energy in the range of some keV to

about 100 keV deposited by the recoiling nucleus.

1.4.2.1 Elastic Scattering Cross Section

The elastic cross section $\sigma(\chi N)$ depends on the individual cross sections of WIMPs scattering off constituent quarks and gluons. For non relativistic majorana particles, these cross sections can be divided into two separate types: coherent (scalar) and incoherent (spin dependent) parts (see for example [Jun96] and references therein) for review on this topic). The following discussion is based on that paper. In general the differential cross section for incoherent (axial) interaction can be written as :

$$\frac{d\sigma_{spin}}{d|\mathbf{q}|^2} = \frac{\sigma_{0spin}}{4m_r^2v^2} F^2(|\mathbf{q}|) \quad (1.17)$$

with the transferred momentum $\mathbf{q} = m_r \mathbf{v}$, where \mathbf{v} is the velocity of the incident WIMP, $m_r = m_N m_\chi / (m_N + m_\chi)$ is the reduced mass with the nuclear mass m_N . $F^2(|\mathbf{q}|)$ is equal to $S(|\mathbf{q}|)/S(0)$, where S is obtained from detailed nuclear calculations. The form factor F is normalized so that $F(0) = 1$, and σ_{0spin} is the total cross section at zero momentum transfer:

$$\sigma_{0spin} = \frac{32}{\pi} G_F^2 m_r^2 \Lambda^2 J(J+1) \quad (1.18)$$

where J is the total angular momentum for the nucleus, and Λ is given by

$$\Lambda = (1/J)[a_p \langle S_p \rangle + a_n \langle S_n \rangle] \quad (1.19)$$

Here $\langle S_p \rangle$ and $\langle S_n \rangle$ are the expectation values of the nucleon group spin in the nucleus, and a_p and a_n are axial couplings.

The differential cross section for coherent interaction is:

$$\frac{d\sigma_{scalar}}{d|\mathbf{q}|^2} = \frac{\sigma_{0scalar}}{4m_r^2v^2} F^2(Q) \quad (1.20)$$

where $F(Q)$ is the form factor. The most commonly used form factor is the exponential form factor [Ahl87, Fre88]:

$$F(Q) = \exp(-Q/2Q_0) \quad (1.21)$$

where Q is the energy transferred from the WIMP to the nucleus, Q_0 is the nuclear ‘‘coherence energy’’. A more accurate form factor is the Woods-Saxon form factor [Eng95]. The total cross section at zero momentum transfer for coherent interaction is:

$$\sigma_{0scalar} = \frac{4m_r^2}{\pi} [Zf_p + (A-Z)f_n]^2 \quad (1.22)$$

where Z is the nuclear charge (the number of protons), $A - Z$ is the number of neutrons, f_p and f_n are the effective couplings of neutralinos to protons and neutrons respectively. Typically f_p is almost equal to f_n . Furthermore,

for heavy WIMPs, $m_\chi \gg m_N$, the reduced mass is then $m_r \simeq m_N$, so that $\sigma_{0\text{scalar}}$ can be simplified as $\sigma_{0\text{scalar}} \propto m_N^4$. However, the actual cross section must be obtained by integrating Eq. (1.20)

1.4.2.2 Expected Event Rate and Energy Spectrum

In general, the rate of events per unit mass of target of a WIMP with interaction cross section σ is given by

$$R = \frac{\sigma \langle v \rangle n}{m_N} \quad (1.23)$$

where $n = \rho_0/m_\chi$ is WIMP number density, σ is the elastic scattering cross section, $\langle v \rangle$ is the average speed of WIMP relative to the target, and m_N is the target nucleus mass.

More accurately, one should take into account the fact that the WIMPs move in the halo with a velocity distribution $f(v)$, that the differential cross section depends upon $f(v)$ through a form factor $d\sigma/d|\mathbf{q}|^2 \propto F^2(Q)$, and that detectors have a threshold energy E_T , below which they are insensitive to WIMP-nuclear recoils. In addition, the Earth moves through the Galactic halo and this motion should be taken into account via $f(v)$.

In general, the differential rate per unit detector mass can be written

$$dR = \frac{\rho_0}{m_\chi m_N} v f(v) \frac{d\sigma}{d|\mathbf{q}|^2} d|\mathbf{q}|^2 dv \quad (1.24)$$

where $f(v)$ is the distribution of speeds relative to the detector, obtained by integrating the three dimensional velocity distribution over all directions (it is normalized to $\int f(v)dv = 1$). The transferred momentum is $|\mathbf{q}|^2 = 2m_r^2v^2(1 - \cos\theta^*)$, where θ^* is the scattering angle in the center-of-mass frame, and $m_r = m_\chi m_N / (m_\chi + m_N)$. The energy deposited in the detector (energy transferred to the nucleus) is

$$Q = \frac{|\mathbf{q}|^2}{2m_N} = \frac{m_r^2 v^2}{m_N} (1 - \cos\theta^*) \quad (1.25)$$

To get the total rate, dR must be integrated over all possible incoming velocities and over deposited energies between threshold energy E_T and $E_{max} = 2m_r^2v^2/m_N$. Using Eqs. (1.17) or (1.20), (1.24), and (1.25), we get

$$\frac{dR}{dQ} = \frac{\sigma_0 \rho_0}{2m_\chi m_r^2} F^2(Q) \int_{v_{min}}^{\infty} \frac{f(v)}{v} dv \quad (1.26)$$

where

$$v_{min} = \sqrt{\frac{Q m_N}{2m_r^2}} \quad (1.27)$$

and $F(Q)$ is the form factor.

By using the energy transfer Q , all the dependence on WIMP velocity has been put into one integral. Now, to make calculation easier, define a dimensionless quantity

$$T(Q) = \frac{\sqrt{\pi}}{2} v_0 \int_{v_{min}}^{\infty} \frac{f(v)}{v} dv \quad (1.28)$$

so that the differential rate can be factorized into a form-factor term and a term which depends upon WIMP velocity

$$\frac{dR}{dQ} = \frac{\sigma_0 \rho_0}{\sqrt{\pi} v_0 m_\chi m_r^2} F^2(Q) T(Q) \quad (1.29)$$

where $v_0 \approx 220$ kms⁻¹ is the circular speed of the Sun around the Galactic center. The total rate of events per kilogram per day is

$$R = \int_{E_T}^{\infty} \frac{dR}{dQ} dQ \quad (1.30)$$

Analysis of data from WIMP direct detection experiments usually assumes the simplest possible halo model, *i.e.* an isothermal sphere with Maxwellian velocity distribution. However, there is no clear justification, observational or theoretical, for this assumption and galaxy halos are in fact thought to be triaxial, with anisotropic velocity distributions. Furthermore the local density distribution may be non smooth, but clumpy (see for example [Gre02]). However, the uncertainties from this simplification are small compared to the theoretical uncertainties in the WIMP-nucleon cross section. For a simple Maxwellian halo the velocity distribution is given by

$$f_1(v') d^3 v' = \frac{1}{v_0^3 \pi^{3/2}} \exp\left(-\frac{v'^2}{v_0^2}\right) d^3 v' \quad (1.31)$$

Leaving out the motion of the Sun and Earth and integrate over all directions to find the speed distribution we obtain

$$f(v') dv' = \frac{4v'^2}{v_0^3 \sqrt{\pi}} \exp\left(-\frac{v'^2}{v_0^2}\right) dv' \quad (1.32)$$

For this case, Eq. (1.28) gives simply

$$T(Q) = \exp\left(-\frac{v_{min}^2}{v_0^2}\right) \text{ (pure Maxwellian)} \quad (1.33)$$

where v_{min} is given by Eq. (1.27). For light WIMPs, where $F(Q) \approx 1$, the differential rate is

$$\frac{dR}{dQ} = \frac{\sigma_0 \rho_0}{\sqrt{\pi} v_0 m_\chi m_r^2} \exp\left(-\frac{Q m_N}{2 m_r^2 v_0^2}\right) \text{ (pure Maxwellian)} \quad (1.34)$$

and integrating it gives the total rate

$$R = \frac{\sigma_0 \rho_0}{m_\chi m_N} \frac{2}{\sqrt{\pi}} v_0 \exp\left(-\frac{E_T m_N}{2m_r^2 v_0^2}\right) \text{ (pure maxwellian)} \quad (1.35)$$

With $E_T = 0$, this result is exactly the naive rate given by Eq. (1.23), since $\langle v \rangle = (2/\sqrt{\pi})v_0$ for the speed distribution of Eq. (1.32)

More realistically, one should take into account the motion of the Sun around the Galactic halo and the Earth rotation around the Sun. These give rise to a yearly modulation in the event rate, which might serve as a convincing method of distinguishing signal and noise if many events are found [Fre88, Dru86]. Following Freese, Frieman, and Gould [Fre88], one subtracts the Earth velocity v_e from v' in Eq. (1.31) to get the velocity v of the WIMP in the Earth frame.

$$\mathbf{v}' = \mathbf{v} + \mathbf{v}_e, \quad v'^2 = v^2 + v_e^2 + 2vv_e \cos \chi \quad (1.36)$$

where χ is the angle between the WIMP velocity in the Earth frame and of the direction of the Earth's motion. As function of time, v_e changes as the Earth's motion comes into and out of alignment with the Sun's motion around the Galaxy. This causes a yearly modulation in the event rate which reaches its maximum around June 2nd each year and its minimum half a year later [Gri88, Dru86]. This is taken into account using

$$v_e = v_0 \left[1.05 + 0.07 \cos \left(\frac{2\pi(t - t_p)}{1 \text{ yr}} \right) \right] \quad (1.37)$$

where $t_p = \text{June 2nd} \pm 1.3 \text{ days}$ [Fre88]. Changing variables, using $d^3v'/d^3v = (v'^2/v^2) \cos \theta / \cos \chi$, and integrating over all directions one gets [Fre88]

$$f(v)dv = \frac{vdv}{v_e v_0 \sqrt{\pi}} \left\{ \exp \left[-\frac{(v - v_e)^2}{v_0^2} \right] - \exp \left[-\frac{(v + v_e)^2}{v_0^2} \right] \right\} \quad (1.38)$$

Then from Eq. (1.28)

$$T(Q) = \frac{\sqrt{\pi}}{4v_e} v_0 \left[\operatorname{erf} \left(\frac{v_{min} + v_e}{v_0} \right) - \operatorname{erf} \left(\frac{v_{min} - v_e}{v_0} \right) \right] \quad (1.39)$$

so that

$$\frac{dR}{dQ} = \frac{\sigma_0 \rho_0}{4v_e m_\chi m_r^2} F^2(Q) \left[\operatorname{erf} \left(\frac{v_{min} + v_e}{v_0} \right) - \operatorname{erf} \left(\frac{v_{min} - v_e}{v_0} \right) \right] \quad (1.40)$$

Unfortunately, the modulation effect is usually small, $\Delta R \lesssim 5\%$ [Jun96, Bae98].

1.4.2.3 Current Experiments

Detecting WIMPs directly means looking for rare events. The already tested rates are of the order of 0.01 count/(kg keV day). Therefore, background should be suppressed as strong as possible. Techniques for background-rejection and subtraction have been developed. Other requirements are high target mass and low energy threshold of the detectors.

Various techniques and detector systems are applied presently for WIMPs searches. They can be classified according to their ability to discriminate nuclear recoil from electron recoil. Most detectors are calibrated and provide a linear response to electron recoils, whereas WIMPs induce nuclear recoils, which tend to produce less ionization or scintillation than electron recoils. Therefore, nuclear recoil discrimination offers a capability for background rejection.

The strategy for all is to use materials and shielding for the setup as radio-pure as possible. Some no-discrimination experiments like Heidelberg-Moscow [Bau99] and HDMS [Bau99] use semiconductor detectors. A proposal for a new experiment, GENIUS [Bau99b], operates 'naked' germanium crystals in liquid nitrogen which has been measured to be a very pure environment. A Test Facility for GENIUS is running at the Gran Sasso laboratory. CUORE [Pre02], CRESST I [Bra99], and Rosebud [Ceb99] are no-discrimination detectors using cryogenic bolometer detectors, while ELEGANT V [Fus02] is a NaI scintillation detector.

The first applied discrimination technique has been pulse-shape discrimination technique for NaI scintillator detectors used by DAMA [Ber98] and UKDM [Kud99]. Beside the ability to discriminate nuclear from electron recoils, it is also possible with NaI detectors to setup large target masses like DAMA (87.3 kg active volume). This enables DAMA to use the annual modulation as a WIMP-signature. The collaboration has in fact, reported a possible evidence for the modulation, as shown in Figure 1.2, and claimed that their data are consistent with the expectation for a WIMP at [Ber00]

$$m_\chi = 59_{-14}^{+17} \text{ GeV}; \quad \xi\sigma_{scalar} = 7.0_{-1.2}^{+0.4} \times 10^{-6} \text{ pb}$$

where $\xi\sigma_{scalar}$ is the WIMP-nucleon scalar cross section normalized to the local halo density (in units of 0.3 GeV/cm^3). However, this evidence is inconsistent with the results reported by three other current experiments (CDMS [Bri02], EDELWEISS [Dra02], and ZEPLIN [Smi02]).

CDMS at Stanford Underground Facility (SUF) and EDELWEISS in the *Laboratoire Souterrain de Modane* (LSM) in France use a combined signal readout of phonon signals and ionization signals from germanium (and silicon in the case of CDMS) crystals. In germanium crystals the ionization efficiency for nuclear recoils is only about 25% (energy dependent, see [Bau98] and references therein) compared to electron recoils.

Twenty-three WIMP candidate events are observed in the CDMS I data

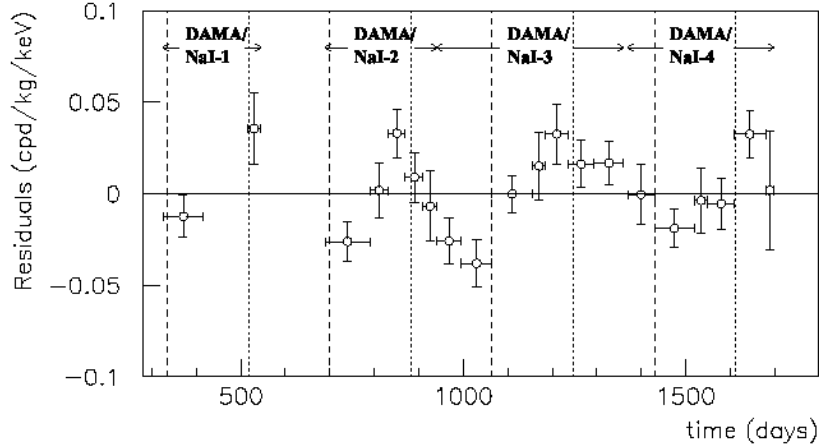


Fig. 1.2 Model independent residual rate for single hit events, in the 2-6 keV cumulative energy interval, as a function of time elapse since January 1st of the year of data taking. The expected behavior of a WIMP signal is a cosine function with minimum roughly at the dashed vertical lines and with maximum roughly at the dotted ones.

from 1998 and 1999 (15.8 kg days exposure for Ge), but these events are consistent with a background from neutrons in all ways tested. Resulting limits on the spin-independent WIMP-nucleon elastic scattering cross section exclude unexplored parameter space for WIMPs with masses between 10-70 GeV/c⁻². Results are compatible with some regions reported as allowed at 3 σ by the annual-modulation measurement of DAMA. However, under the assumptions of standard WIMP interactions and a standard halo, the results are incompatible with the DAMA most likely value at > 99% CL, and are incompatible with the model-independent annual-modulation signal of DAMA at 99% CL [Cdm02].

In the energy range relevant for WIMP masses below 10 TeV/c², EDELWEISS observed no nuclear recoils in the fiducial volume of its cryogenic 320 g germanium detector during an exposure of 7.4 kg days [Dra02]. Combined with the previous EDELWEISS data, the exclusion limit derived for spin-independent (scalar) interaction exclude a WIMP with mass of 44 GeV/c² and cross section of 5.4×10^{-6} pb as reported by DAMA by more than 99.8% CL.

The discrimination concept employed in ZEPLIN I is ionization and scintillation signal readout from liquid Xenon. The ZEPLIN setup is located in the Boulby mine in England. A similar sensitivity as that of EDELWEISS is obtained by ZEPLIN I with 230 kg days of exposure time.

IGEX is actually a ⁷⁶Ge double-beta decay experiment. One IGEX detector (active mass ~ 2.0 kg) is currently operating in the Canfranc un-

derground laboratory in a search for dark matter WIMPs, through the Ge recoil produced by the WIMP elastic scattering. A new exclusion plot has been derived for WIMP-nucleon spin independent interactions using data taken during 2001. Cross sections down to $\sim 7 \times 10^{-5}$ pb are excluded for WIMP masses of ~ 50 GeV.

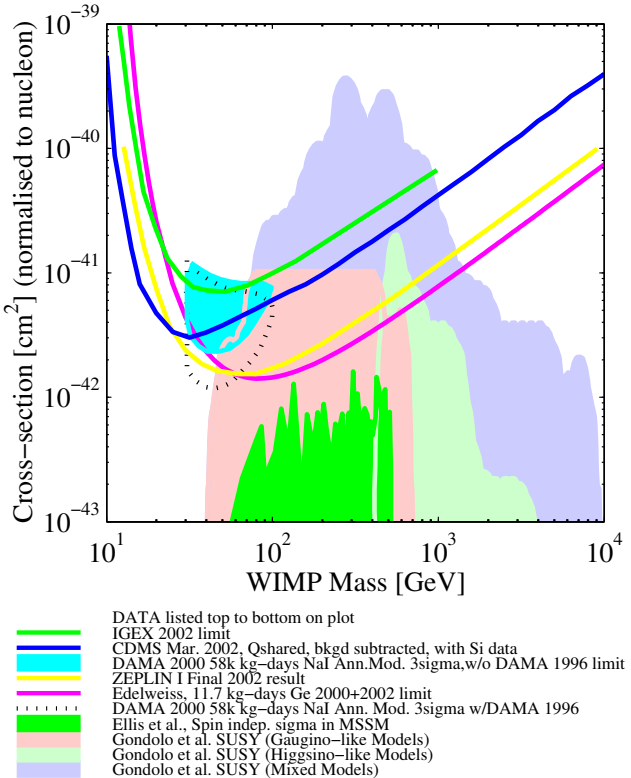


Fig. 1.3 Limits on the WIMP-nucleon cross section for scalar (coherent) interactions as a function of the WIMP mass reached by some current experiments and theoretical expectations.

Figure 1.3 shows the exclusion plot of IGEX [Mor01], CDMS [Abr02], ZEPLIN [Smi02], and EDELWEISS [Ben02], together with the DAMA [Ber00b] allowed regions and some theoretical predictions. Regions above the curves are excluded. This figure was produced by using an interactive plotter for experimental and theoretical data of WIMP dark matter available on a web site maintained by Rick Gaitskill and Vuk Mandic [Gai03].

CRESST II combines phonon and scintillation readout to discriminate nuclear recoils from electron recoils. This experiment will be described in the next chapter.

1.4.2.4 Neutron Background

The neutron flux is considered as an important parameter characterizing underground environments. In direct searches for WIMPs neutrons are a particularly important background source because they produce the same signature as the WIMPs. Therefore they can not be eliminated by active background rejection techniques as described in the previous subsection. This background neutrons will in turn limit the sensitivity of the experiment. The current results of CDMS, for instance, were obtained from the measurements performed at shallow depth at SUF. Muon-induced neutrons represent a major source of background. The experiment is now moved to a deeper site in the Soudan underground laboratory, where the flux of muons is reduced significantly. Even at large depth CDMS and other dark matter searches still have to cope with the problems of neutrons, especially if higher and higher sensitivity is to aim for. Besides, the understanding of the neutron background may be relevant in resolving the controversy between DAMA and other current experiments.

The recoil energy of a target nucleus hit by a neutron is described by the following equation:

$$E_R(\text{neutron}) = \frac{2E_n M_N m_n}{(M_N + m_n)^2} (1 - \cos \theta) \quad (1.41)$$

where E_n , M_N , m_n and θ are the neutron energy, the nucleus mass, the neutron mass and the scattering angle in the center of mass respectively. The maximum recoil energy is given by head on collision, $E_R(\text{neutron, max}) = \frac{4E_n M_N m_n}{(M_N + m_n)^2}$. A WIMP that hits a target nucleus would give a recoil energy as the following:

$$E_R(\chi) = \beta^2 \frac{M_\chi^2 M_N}{(M_\chi + M_N)^2} (1 - \cos \theta) \quad (1.42)$$

where $\beta = v/c$ is the WIMPs velocity in the units of c and M_χ is the WIMP mass.

For a typical neutron energy of 1 MeV, a WIMP mass of 60 GeV and assuming $v = 250 \text{ km/s} \approx 10^{-3}c$ and head on collision on several target nuclei we get maximum recoil energies for neutron-induced and WIMP-induced events as shown in Table 1.1. It is clear, that the heavier the target nucleus, the more difficult it is to distinguish WIMP-induced recoils from neutron-induced recoils.

The neutron flux present at an experimental setup comes from different origins:

- (1) Low energy neutrons induced by fission and (α, n) reactions due to uranium and thorium activities in the surrounding rock and concrete. They give the bulk to the total flux in an underground laboratory.

Table 1.1 Maximum recoil energies for neutron-induced and WIMP-induced events.

Target Nucleus	m_N (GeV)	Neutron-induced (keV)	WIMP-induced (keV)
O	16	221	20
Si	28	133	26
Ca	40	95	29
Ge	73	53	30
Xe	131	30	26
W	184	22	22

- (2) Low energy neutrons induced by fission in the shield material and the setup.
- (3) High energy neutrons induced by muons in the rock. These neutrons could do spallation reactions in the experimental shield and produce additional neutrons.
- (4) High energy neutrons induced by muons in the shielding material (especially lead).

Neutron background is intensively studied by many collaborations. A working group of CRESST, EDELWEISS and UKDM called ETNo μ Siq (European Team for Neutron and μ Simulation and Qualification), for example, works together and meets regularly to discuss and exchange information on this topic.

In this work neutron-induced background in the CRESST experiment has been investigated. Contributions of all aforementioned sources of neutrons to the rate expected in CRESST and the way to get rid of them will be discussed.

Chapter 2

The CRESST Experiment

The CRESST (Cryogenic Rare Event Search using Superconducting Thermometers) setup is located at the Gran Sasso laboratory in Italy. The goal of the CRESST project is the direct detection of elementary particle dark matter and elucidation of its nature[Cre01].

This chapter discusses the detection concept of CRESST, the experimental setup at Gran Sasso and the current status of the experiment.

2.1 Detection Concept

The basic detection technique of CRESST is the measurement of non-thermal phonons produced by WIMP-induced nuclear recoils in a crystal. The energy deposited by elastic scattering of WIMPs on nuclei is small, *i.e.* typically in the order of some tens of keV for WIMPs with mass of some tens of GeV. To be able to detect this small amount of energy, cryogenic calorimeters with superconducting thermometers are used.

The detector employed in CRESST consists of a dielectric crystal (target/absorber), in which the particle interaction takes place, and a small superconducting film evaporated onto the crystal surface, functioning as a highly sensitive thermometer. Energy deposited in the absorber causes small change in temperature of the film. The detector is operated within the super conducting-to-normal transition of the thermometer, where a small temperature rise ΔT leads to a relatively large rise ΔR of its resistance. This change in resistance is measured with a SQUID. The ΔT induced by a particle is usually much smaller than the width of the transition, which leads to an approximately linear relation between ΔT and ΔR (see Figure 2.1).

To good approximation, the high frequency phonons created by an event do not thermalize in the crystal before being directly absorbed by the super conducting film [Prö95]. Therefore the energy resolution is only moderately dependent on the size of the crystal, and scaling up to large detector is feasible. The high sensitivity of this system also allows the use of a small separate detector of the same type to see the light emitted when the absorber is a scintillating crystal. In CRESST phase I 262 g sapphire (Al_2O_3)

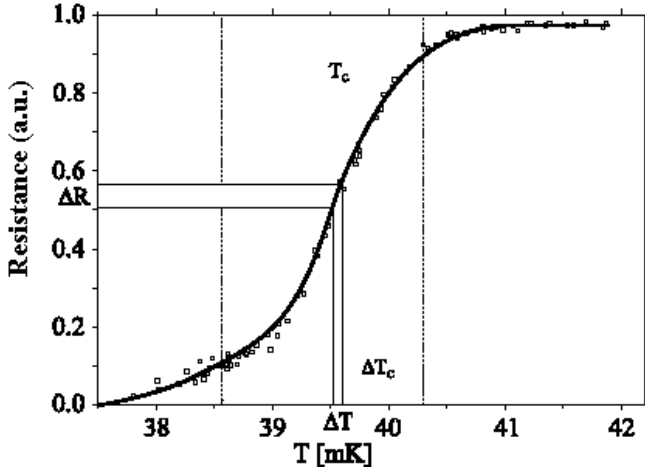


Fig. 2.1 Transition curve of a super conducting thermometer. A small temperature rise ΔT leads to a relatively large rise ΔR of its resistance.

was used as absorber and tungsten film was employed as thermometer. In principal a variety of other materials can be used. For CRESST II calcium tungstate (CaWO_4), a scintillating crystal, is used as absorber.

With a 262 g sapphire absorber and a tungsten thermometer CRESST phase I reached an energy resolution of 133 eV at 1.5 keV in the spectrum of an X-ray fluorescence source [Bra99]. This is the best energy resolution per unit mass of a cryogenic device achieved so far. Beside the excellent energy resolution CRESST phase I could also achieve an energy threshold of around 500 eV.

In such a rare event search, where one expects an event rate of the order of 1 count/keV/kg/day or below, the background must be suppressed as much as possible. But in spite of the employment of passive background reduction techniques, *i.e.* going to a deep underground site, efficient shielding against radioactivity of the surrounding rock, and the use of radiopure materials inside the shielding, there is remaining background dominated by β and γ emission from nearby radioactive contaminants that leads to electron recoils in the detector. On the other hand WIMPs, and also neutrons, produce nuclear recoils. Therefore, the sensitivity of detection can be improved dramatically if, in addition to the passive shielding, the detector itself is able to discriminate electron recoils from nuclear recoils and “actively” reject them.

A particle interaction in a scintillating crystal produces mainly phonons and scintillation light. Low energy nuclear recoils create much less scintillation light than electron recoils of the same energy. Therefore, a measurement of the energy branching between scintillation light and phonons can

clearly distinguish nuclear recoils from electron recoils. This is exactly the new detection concept being applied for CRESST phase II. With CaWO₄ as absorber, the measurement of scintillation light is carried out in parallel to the phonon detection [Bra99].

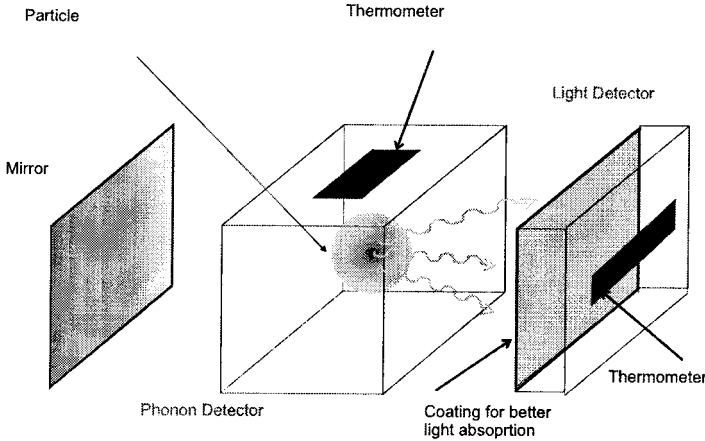


Fig. 2.2 Schematic view of the arrangement used for the simultaneous light and phonon detection.

The setup for simultaneous light/phonon detection is shown schematically in Figure 2.2. It consists of two independent detectors. The main (larger) absorber is CaWO₄ with a phase transition thermometer on its surface that measures phonons produced by interactions in the absorber. This absorber also scintillates at low temperature. Next to the first crystal, a similar but smaller detector is placed to detect the scintillation light.

Several tests were done, first by irradiating the CaWO₄ crystal with photons from a ⁵⁷Co-source and simultaneously with electrons from a ⁹⁰Sr-source, and then neutrons from an Am-Be source were added. Figure 2.3 shows a scatter plot of the pulse height measured in the phonon detector versus the pulse height observed in the light detector.

Two bands are clearly distinguishable in Figure 2.3. The upper band shows electron recoils induced by β 's and γ 's, while the lower band is produced by neutron-induced nuclear recoils. This allows a rejection of the electron recoils with an efficiency of at least 99.7% for nuclear recoil energies above 15 keV.

The simultaneous measurements of light and phonons has several advantages over the parallel measurement of charge and phonon as employed by CDMS and EDELWEISS. First, it does not suffer from the “dead layer” problem. With charge measurement an incomplete collection of the charges from events near the surface of the crystal may lead to a misidentification of an electron recoil as a nuclear recoil. Besides, tungstate in CaWO₄ crystal is a very efficient target for scalar (coherent) WIMP-nucleus scattering.

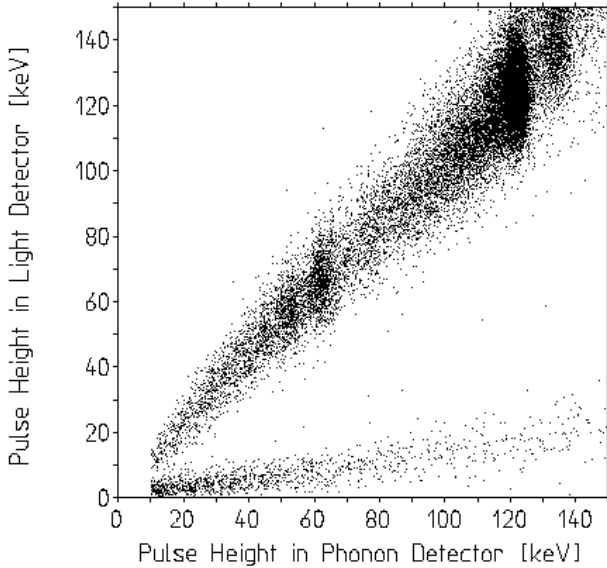


Fig. 2.3 Pulse height in the light detector versus pulse height in the phonon detector. The upper band shows electron recoils induced by β 's and γ 's, while the lower band is produced by neutron-induced nuclear recoils [Meu99].

2.2 CRESST Setup at LNGS

The central part of the CRESST low background facility in the Gran Sasso underground laboratory is the cryostat, whose design had to combine the requirements of low temperature with those of low background. A well separated “cold box” houses the experimental volume at some distance from the cryostat (see Figure 2.4).

The cold box is made of low background copper, with high purity lead used for the vacuum seals. It is surrounded by shielding, consisting of 14 cm of low background copper and 20 cm of lead. Any direct line of sight from the outside world and the cryostat into the cold box is eliminated by the combination of external shielding together with the internal shields. The low temperature of the dilution refrigerator is transferred to the cold box by a 1.5 meter long cold finger protected by thermal radiation shields, all are made of low background copper to minimize radioactivity. A 20 cm thick lead shield inside a copper can is placed between the mixing chamber and the cold finger, with the low temperature being transmitted here by the copper can. This internal shield, combined with another one surrounding the cold finger, serves to block any line of sight for radiation coming from the dilution refrigerator into the experimental volume.

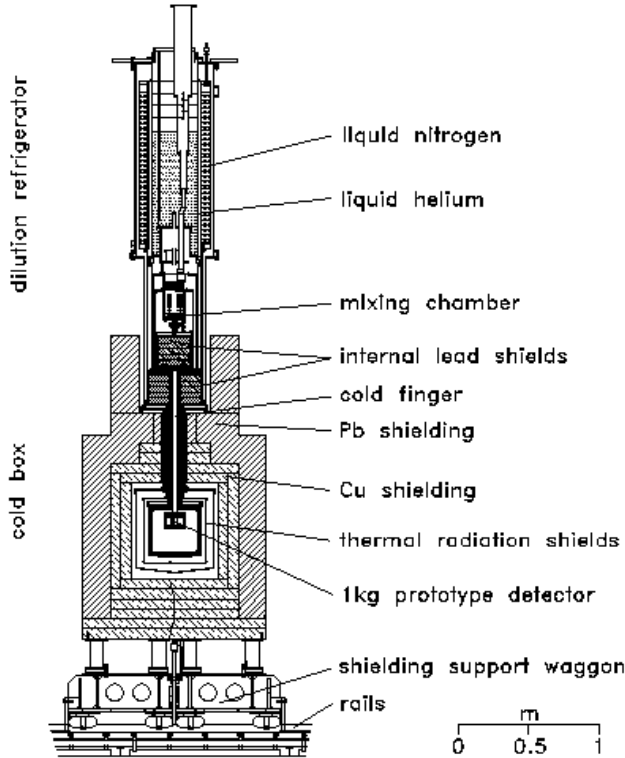


Fig. 2.4 Layout of the dilution refrigerator and cold box.

To avoid activation by cosmic rays, the amount of the time that the copper of the shielding and the cold box spent above ground was minimized. To prevent contamination of their surfaces, the cryostat and the shield are placed in a clean room. All work on the low-background components of the experiment can be performed inside this room. The entire shielding is enclosed in a gas-tight radon box flushed with N_2 to avoid radon contamination from the air. The access to the top of the cryostat for servicing and to the electronics is allowed from outside the clean room. A Faraday cage surrounds the clean room and the entrance to the cryostat.

The CRESST setup was located in hall B of the Gran Sasso laboratory. Because of the plan to build detectors for long-baseline neutrino experiments CERN-Gran Sasso in hall B, CRESST had to move to hall A. Just after CRESST phase I achieved its goal in April 2001, the measurements had to be stopped. After around one year of interruption measurements could be resumed in fall 2002.

2.3 Results of CRESST Phase I

The goal of CRESST phase I was to show the possibility to operate 1 kg of sapphire in the milli-Kelvin range, with a threshold of 500 eV under low background conditions [Coo93]. This detector with an extremely low energy threshold and a low mass target nucleus with high spin (*Al*) is sensitive to the low WIMP-mass range of 1 - 10 GeV. As mentioned in the previous section, the measurements were done with phonon readout only.

After the desired background level had been achieved, *i.e.* just before CRESST had to move from hall B to hall A, measurements with 262 g sapphire could be done in the Gran Sasso laboratory. The results published in [Ang02] are based on ten hours of calibration measurement with an external ^{57}Co -source, a measurement of 138.8 hours (an exposure of 1.51 kg day) without source, and a further calibration measurement at the end. Two detectors were employed. The one with lower threshold energy (detector No.8 in the production series) dominates the results and therefore only this detector was used for the determination of new WIMP limits. The second detector served to exclude coincident signals.

The trigger efficiency of the detectors was 100% down only to 580 eV in energy. Therefore, an energy threshold of 600 eV was put by software to avoid the issue of trigger efficiency in the analysis. In the energy range from this threshold to 120 keV, 446 events were collected by the detector. 76 events (17% of all events), that also coincidentally were measured in the second detector and therefore can not be due to WIMPs, were excluded.

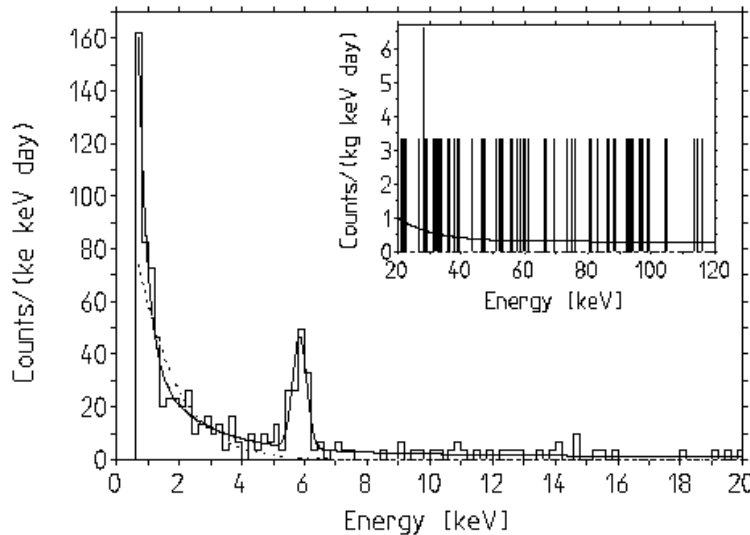


Fig. 2.5 Energy spectrum of the CRESST I measurement at Gran Sasso (1.51 kg day) in 200 eV bins. The figure in the inset shows the spectrum at higher energy. Solid line: empirical fit for experimental spectrum, that has been used for data analysis and for calculating a WIMP-limit. Dashed line: spectrum as expected for WIMP of mass 5 GeV with a cross section that is excluded by data with 90% C.L. [Ang02].

As the two cube-shaped detectors faced each other with only one of their six surfaces, it is expected, that in future measurements with an array of detectors, where all surfaces are covered with the neighboring detectors, a large part of the events can be excluded by coincidence. Hence the background could be further reduced. Some of the remaining 370 events, that are caused by vibrations or electronic noise, showed an unusual signal shape. After this events were excluded, 320 events survived and the spectrum is shown in Figure 2.5. A background rate of 0.7 events/kg/day above 15 keV and of 0.3 events/kg/day at 100 keV remained. At 5.9 keV there is a line with about 7 events/day. The energy of the line suggested, that it was caused by a contamination from ^{55}Fe -source used to test the detector in the laboratories in Munich.

To derive the upper limit on the scattering rate of WIMPs, the experimental spectrum has to be compared with the spectrum expected from elastic scattering of WIMPs. To calculate the recoil spectrum expected from WIMPs, the velocity distribution of [Don98] was used (isothermal WIMP-halo model, Maxwellian velocity distribution around 220 km/s, escape velocity of 650 km/s, relative velocity of the Earth of 230 km/s, and a local WIMP density of 0.3 GeV/cm³). In sapphire only ^{27}Al with spin 5/2 and 100% isotopical abundance contributes to the spin-dependent scattering.

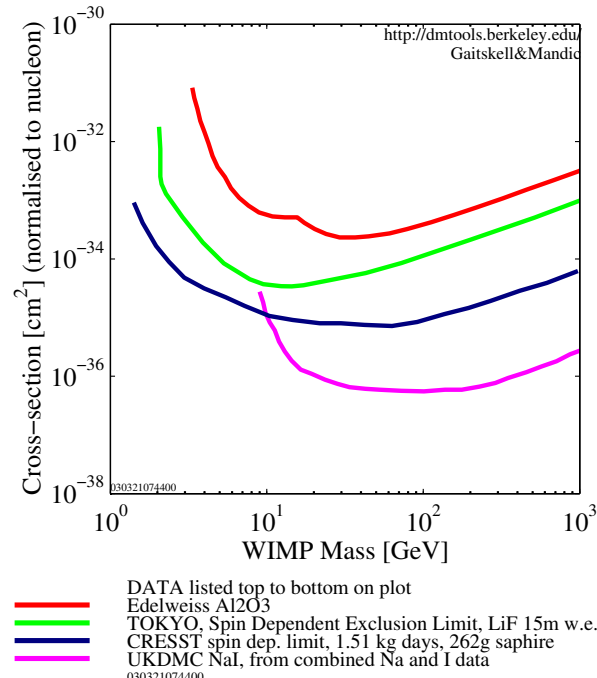


Fig. 2.6 Equivalent WIMP-proton cross section limit (90% C.L.) for spin dependent interaction as a function of WIMP mass from an exposure of 1.51 kg days in CRESST I with a 262 g sapphire crystal [Ang02]. As comparison the limits from EDELWEISS [Bel96] (sapphire-calorimeter), Tokyo [Oot99] (LiF detectors) and UKDMC [Spo00] (NaI detectors) are shown.

The form factor used for aluminum comes from [Eng95] and the form factors for the spin-independent interaction from [Hel56]. For the determination of exclusion plot a Monte Carlo method was used [Ang02]. Figure 2.6 shows the 90% CL upper limit for the cross section by spin-dependent interaction.

As the comparison with measurements with n-type nuclei, like ^{73}Ge is questionable, only experiments with p-type nuclei are shown together [Sei98, Eng89, Ell91]. As one can see, CRESST improves the existing limit for the low WIMP-masses and hence, the goal of the CRESST phase I was achieved.

For the spin-independent (scalar) interaction the light nuclei like Al and O are not advantageous compared to nuclei like Ge or I, due to coherence of the interaction. Nevertheless, the limit for the low mass WIMPs below 5 GeV could be given for the first time (see Figure 2.7).

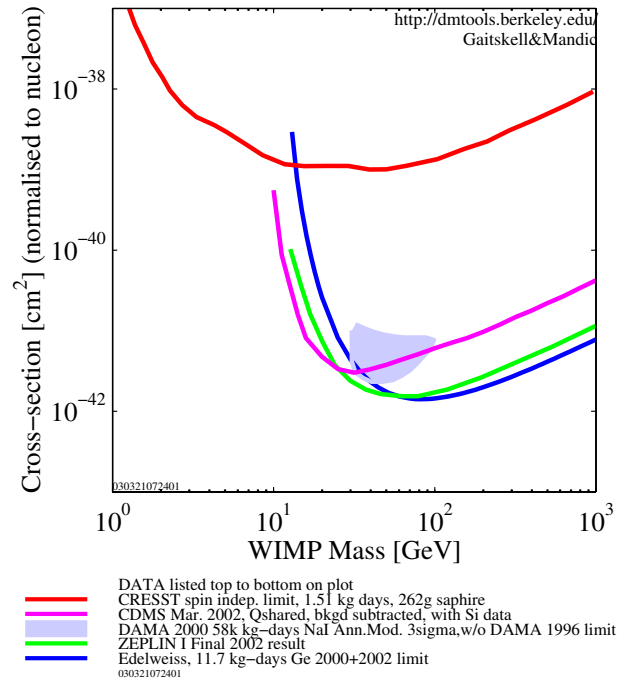


Fig. 2.7 Equivalent WIMP-proton cross section limit (90% C.L.) for spin independent interaction as a function of WIMP mass from an exposure of 1.51 kg days in CRESST I with 262 g sapphire target [Ang02]. As comparison the limits from EDELWEISS [Ben02], CDMS [Abr02], ZEPLIN I [Smi02] and the DAMA annual modulation region [Ber00b] are shown.

2.4 CRESST Phase II

For the second phase of CRESST a detector with a total mass of about 10 kg using the simultaneous measurement of scintillation light and phonons is planned. The detector will consist of 33 modules based on CaWO₄ crystals with a mass of 300 g each. It will allow an efficient discrimination of radioactive backgrounds and will be especially sensitive to medium and high mass WIMPs. To reach 10 kg of detector mass the CRESST setup will be upgraded to 66 readout channels.

The use of tungsten, that has a large atomic number, as target makes the second phase detector particularly sensitive to WIMPs with coherent interaction. Here the WIMP cross section profits from a large coherence factor of the order of A^2 , where A is the number of nucleons. Combined with the strong background rejection this means the detector can be sensitive to low WIMP cross section.

Figure 2.8 shows the expected sensitivity of the second phase. The expected sensitivity curve is based on a background rate of 1 count/kg/keV/day, an intrinsic background rejection of 99.7% above a recoil threshold of 15 keV and an exposure of 3 kg years. Preliminary result of CRESST II from Run 23 (4.112 kg day) is also shown. For comparison present experimental limit from several experiments are shown together with the contour for positive evidence from DAMA [Ber00b].

In a 10 kg CaWO₄ detector, 60 GeV WIMPs with the cross section as claimed in [Ber00] would give about 46 counts between 15 and 25 keV within one month. A background of 1 count/kg/keV/day suppressed with 99.7% would leave 9 background counts in the same energy range. A 10 kg CaWO₄ detector is expected to be able to test the reported positive signal with one month of measuring time. But already at this point neutron background would cause a problem (see discussion in Chapter 3).

Nuclear recoils in scintillators produce much less scintillation light than electron recoils do. This is called the “quenching” of the light signal and is the basis of background suppression. The light quenching factor for recoils on tungsten in a CaWO₄ crystal is probably higher than for recoils on oxygen or calcium. As the tungsten recoil is relevant for the WIMP search, the light quenching factor for W recoils must be determined.

The quenching factor for the phonon signal can also be different from one. The light produced by an interaction is lost for the phonon measurement, therefore one expects that the phonon signal for an electromagnetic interaction is smaller than for a nuclear recoil, that does not produce so much light. Hence, in the measured spectra the energy scale for electromagnetic radiation is different from that for nuclear recoils.

To determine the two quenching factors for different detectors used in the search for WIMPs a neutron scattering experiment is built at the accelerator

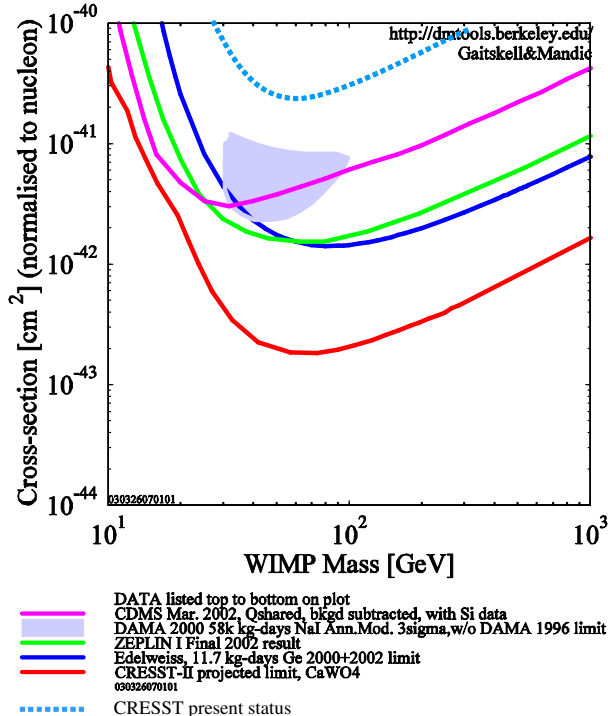


Fig. 2.8 WIMP-nucleon cross section limits (90% C.L.) for scalar (coherent) interactions as a function of WIMP mass, expected for the second phase of CRESST. The curve is based on a background rate of 1 count/kg/keV/day, an intrinsic background rejection of 99.7% above a recoil threshold of 15 keV and an exposure of 3 kg years. The preliminary result of CRESST II from Run 23 (4.112 kg day) is shown by dotted line. As comparison the limits from EDELWEISS [Ben02], CDMS [Abr02], ZEPLIN I [Smi02] and DAMA annual modulation region [Ber00b].

at the Maier-Leibnitz-Laboratory in Munich. The basic idea is to generate a mono energetic recoil of known energy in a calibrated cryogenic detector. At the detector neutrons of known energy and given angle are scattered elastically, by which the recoil energies are kinematically determined.

The neutron beam is pulsed, so that the neutron energy can be determined by its time of flight. The scattering angle is determined by neutron detectors, that are set up in different directions with respect to the scattering center. As neutron detectors 50 cells with liquid scintillator are used. The scintillator can distinguish gammas from neutrons by pulse form analysis.

In this experiment neutrons are produced by the reaction $p(^{11}B,n)^{11}C$. The ^{11}B beam is directed to a hydrogen gas cell. With this reaction neutrons with energies up to 11 MeV can be produced, that is enough to deposit a measurable recoil energy on the heavy tungsten nuclei.

Another important issue that should be handled in the second phase of the CRESST experiment is the protection against neutron background. It will be discussed in Chapter 3 that already in the range of the present sensitivity of some 10^{-6} pb in the WIMP-proton scattering cross section, where the DAMA evidence is reported, one has to take neutron-induced background into consideration. Therefore a shielding against neutron-induced background is planned to be installed in Gran Sasso. The next chapters will discuss different neutron sources in Gran Sasso, their contribution to the background rate in CRESST, and the ways to reduce them.

Chapter 3

Background Induced by Low Energy Neutrons

Low energy neutron flux underground comes mainly from the rock and concrete surrounding an experimental setup. It gives the bulk of the total flux of neutrons at the experimental site. These neutrons are produced through (α,n) and fission reactions due to activities in the rock and concrete. This chapter discusses the calculation of neutron production rates in the surrounding rock and concrete at Gran Sasso. The expected flux at the experimental site and the simulations of background induced by low energy neutrons in the CRESST setup are presented. In addition, neutrons from fission reaction in the shielding material of CRESST will also be covered.

3.1 Neutron Flux Measurements at LNGS

Measuring the neutron flux underground is not an easy task because of its very low intensity. At present there exists a number of measurements at LNGS employing different methods of detection as summarized in Table 3.1. The results of those measurements are shown in Table 3.2. It is clearly seen that there are discrepancies in the results. Most of the measurement results are given in large energy bins. Only two works [Bel89, Arn99] give some information about the spectral shape. Almost all of the measurements were performed in hall A, only the measurement by the ICARUS group [Arn99] was done in hall C.

The total flux of [Arn99] is basically consistent with the result of [Bel89] for $E > 1$ MeV, while the energy spectrum as a whole is significantly harder. The results from [Arn99] show important distortions with respect to the spectrum in the hypothesis that was previously assumed in the literature, *i.e.* that neutrons are mainly produced by spontaneous fission. The difference is seen at high energies. To search for a possible explanation the authors considered the production of neutrons *via* (α,n) reactions inside the rock and computed the 'thin target' spectrum of neutrons produced by the reaction $^{17}\text{O}(\alpha,n)^{20}\text{Ne}$ only. The (α,n) and spontaneous fission spectra were

Table 3.1 Detection methods for the neutron flux measurements at Gran Sasso.

Detector	Detection Reaction	Neutron Signature	Ref.
Prop. Counter ^3He	$\text{n} + ^3\text{He} \rightarrow \text{p} + ^3\text{H}$	p	[Rin88]
Liquid Scintillator NE320(^6Li doped)	$\text{n} + ^6\text{Li} \rightarrow \alpha + ^3\text{H} + \gamma$	Elastic scattering (n,p), γ (4.8 MeV)	[Ale88]
Prop. Counter BF_3	$\text{n} + ^{10}\text{B} \rightarrow ^7\text{Li}^* + \alpha + \gamma$ $\rightarrow ^7\text{Li} + "E^*$ "	γ (2.3 MeV) $E^* = 2.8$ MeV	[Bel89]
$(\text{CaNO}_3)_2$ aqueous sol. Organic scint. with high H content + Cd	$\text{n} + ^{40}\text{Ca} \rightarrow ^{37}\text{Ar} + \alpha$ $\text{n} + \text{p} \rightarrow \text{n} + \text{p}$ n captured by Cd $\rightarrow \gamma$ cascade $\rightarrow \text{e}$ in detector	^{37}Ar decay ; E = 2.82 keV p recoil + e signal (10 ms)	[Cri95] [Arn99]

Table 3.2 Neutron flux measurements at LNGS reported by different authors.

E interval (MeV)	Neutron Flux ($10^{-6}\text{cm}^{-2}\text{s}^{-1}$)					
	[Bel89]	[Arn99]	[Ale88]	[Bel85]	[Rin88]	[Cri95]
$10^{-3} - 1$	0.54 \pm 0.01					
1 – 2.5		0.14 \pm 0.12				
2.5 – 5	0.27 \pm 0.14	0.13 \pm 0.04		2.56 \pm 0.27		
5 – 10	0.05 \pm 0.01	0.15 \pm 0.04	0.78 \pm 0.3		3.0 \pm 0.8	0.09 \pm 0.06
10 – 15	$(0.6 \pm 0.2).10^{-3}$	$(0.4 \pm 0.4).10^{-3}$				
15 – 25	$(0.5 \pm 0.3).10^{-6}$					

then used as input for the MCNP (Monte Carlo N-Particles) code to obtain the effective neutron flux in hall C. They found that their measurements and simulations are in very good agreement and that (α, n) reactions are the main source of the high energy neutron flux in the laboratory.

However, there are doubts addressed to the results from [Arn99]. Gerbier [Ger02] argues that the uncertainties have been underestimated. His arguments are discussed below.

Proton recoil technique in an organic liquid scintillator with a high hydrogen content was used in this experiment. The signature of a neutron interaction is one or more proton recoil signals (selected from the pulse shape) followed, within $10 \mu\text{s}$, by electron signals. The background run time ($\approx 3 \times 10^6 \text{ s}$) is about three times shorter than the data run time ($1.088 \times 10^7 \text{ s}$). The spectrum of proton recoils (see Figure 3.1) has 5 bins with 81 events obtained after subtraction of 1604 background events.

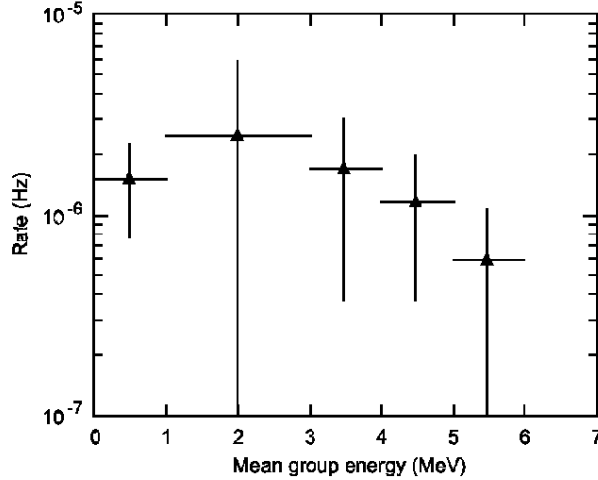


Fig. 3.1 Mean neutron energy *vs.* rate from the ICARUS neutron flux measurement [Arn99].

In Table 3.3 “Signal” is the rate (Hz) times data run time, that is the total number of events. “Background” is obtained by subtracting “Signal” from “(p+e) events” and “ σ on plot” is the square root of “Background”. Basically, what is plotted in Figure 3.1 is “Signal” with uncertainty of “ σ on plot”. Here we can see that two data points, *i.e.* the second and the fifth, have a very large error and are therefore insignificant. Moreover, we have to recall that the background run is about three times shorter than the data run. Therefore, the proper uncertainty should be “ σ on plot” times $\sqrt{3}$ as shown in “ σ on data run”. What should be plotted in Figure 3.1 are then “Signal” with uncertainty of “ σ on data run”. It turns out that all data points are insignificant. The agreement between the thin target calculation and the measurement found here is accidental. Nevertheless, neutron production from (α, n) reactions has to be taken into account due to its contribution to the flux of high energy neutrons.

Table 3.3 Correction for σ in the ICARUS neutron flux measurement.

E bin (MeV)	p+e events	Rate (Hz* 10^{-6})	Signal	Background	σ on plot	σ on data run
0-1	65	1.51	16	49	7	13
1-3	1312	2.49	27	1285	36	65
3-4	205	1.69	18	187	14	25
4-5	74	1.16	13	61	8	14
5-6	28	0.588	6	22	5	8
Total		7.438	81	1604		

The discrepancies of the measurements, their questionable reliability and the lack of detailed information on the shape of the spectrum in the energy range interesting for CRESST raised motivation to reinvestigate neutrons from (α, n) and fission reactions in the rock and concrete. An additional reason is to study the dependence of neutron flux and recoil count rates on the humidity of the surrounding rock and concrete. As mentioned in Chapter 1, the DAMA experiment has reported an annual modulation of the signal they measured. They have done several study to check if this modulation is caused by other effects [Bel02]. It is worthwhile therefore to see whether variation of water content in the rock and concrete could modulate the signal rates.

3.2 Calculation and Simulation of the Low Energy Neutron Flux from Fission and (α, n) Reactions in the Surrounding Rock/Concrete

3.2.1 *Neutron Production by Spontaneous Fission*

There are mainly three nuclides in nature that undergo spontaneous fission: ^{238}U , ^{235}U and ^{232}Th . In this work only neutrons produced by spontaneous fission of ^{238}U are considered, because of the long fission half life of the other two nuclides compared to that of ^{238}U . The shape of the neutron spectrum follows Watt spectrum:

$$N(E) = C \exp(-E/a) \sinh(bE)^{1/2} \quad (3.1)$$

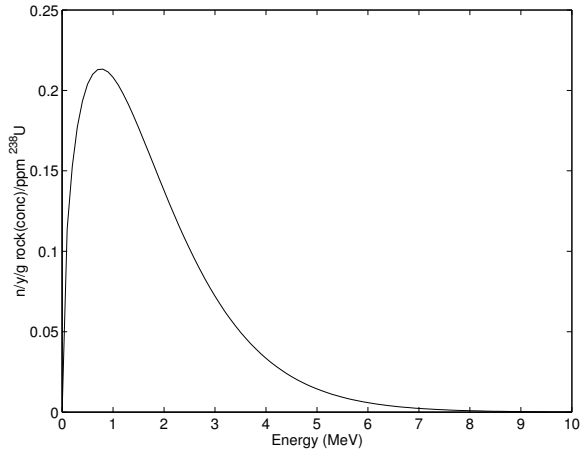


Fig. 3.2 Energy spectrum of neutrons from spontaneous fission of ^{238}U .

Figure 3.2 shows the neutron energy distribution due to spontaneous fission of ^{238}U . In this work the Watt spectrum parameters of the Los Alamos model results were used [Mad01], where $a = 0.7124 \text{ MeV}$ and $b = 5.6405 \text{ MeV}^{-1}$.

The rate of spontaneous fission of ^{238}U is $0.218/\text{year/g}$ of rock (concrete) for 1 ppm of ^{238}U and the average number of neutrons emitted per fission event is 2.4 ± 0.2 [Lit52]. This gives $0.52 \text{ neutrons/year/g}$ of rock (concrete)/ppm ^{238}U .

3.2.2 Neutron Production by (α, n) Reactions

Uranium, thorium, and their daughter products decay by emitting α and β particles. In the rock (concrete) α -particles can interact especially with light elements and produce neutrons through (α, n) reactions.

The yield of neutrons per α -particle for individual element depends on the (α, n) interaction cross section (which is energy dependent) and on the energy loss of α -particles in a medium made of that element. In this work the thick target yield of (α, n) reactions was used instead of the thin target yield used in [Arn99]. The thick target yield of the (α, n) reaction for an individual element j in which the α -particle has a range R may be written as [Fei68]:

$$Y_j = \int_0^R n_j \sigma_j(E) dx \quad (3.2)$$

where n_j is the number of atoms per unit volume of element j , and σ_j is the microscopic (α, n) reaction cross section for an α -particle energy E . Transforming the integral to energy gives:

$$\begin{aligned} Y_j &= \int_0^{E_i} \frac{n_j \sigma_j(E)}{-(dE/dx)} dE \\ &= \int_0^{E_i} \frac{n_j \sigma_j(E)}{\rho_j S_j^m(E)} dE \\ &= \int_0^{E_i} \frac{n_j \sigma_j(E) N_A}{n_j A_j S_j^m(E)} dE \\ &= \frac{N_A}{A_j} \int_0^{E_i} \frac{\sigma_j(E)}{S_j^m(E)} dE \end{aligned} \quad (3.3)$$

where E_i is the initial α -energy, N_A is the Avogadro number, A_j is the atomic mass and σ_j and S_j^m are the (α, n) cross section and the mass stopping power respectively, which are energy dependent.

Neutron yields from individual elements can be used to calculate the total yield in a chemical compound or mixture. The calculation was developed

by several authors [Fei68, Wes79, Bul82]. The following assumptions are usually made in such a calculation:

- (i) the compound is a homogeneous mixture of its constituent elements
- (ii) Bragg's law of additivity for stopping power holds for the compound
- (iii) the ratio of an element's stopping power to the total stopping power of the compound is independent of the α -particle energy.

The validity of (iii) has been discussed by several authors. Although for each element the mass stopping power S_j^m decreases with energy, Feige [Fei68] found that the mass stopping power ratio for any pair of elements does not change by more than $\pm 4\%$ between 5.3 MeV and 8.8 MeV. Heaton *et al.* [Hea90] showed that above 3 MeV this approximation introduces an uncertainty of less than 5% in the neutron yield.

Under those assumptions the neutron yield of element j in the compound or mixture with initial α -particle energy E_i can be written as:

$$\begin{aligned}
 Y_{i,j,mix} &= \int_0^{E_i} \frac{n_j \sigma_j}{\sum_j \rho_j S_j^m} dE \\
 &= \int_0^{E_i} \frac{\rho_j S_j^m}{\sum_j \rho_j S_j^m} \frac{n_j \sigma_j(E)}{\rho_j S_j^m} dE \\
 &= \frac{\rho_j S_j^m(E_0)}{\sum_j \rho_j S_j^m(E_0)} \int_0^{E_i} \frac{n_j \sigma_j(E)}{\rho_j S_j^m} dE \\
 &= \frac{M_j S_j(E_0)}{\sum_j M_j S_j(E_0)} Y_j(E_i)
 \end{aligned} \tag{3.4}$$

where M_j is the mass fraction of element j in the mixture, E_0 is a chosen reference energy (8 MeV in this work), S_j^m is mass stopping power and $Y_j(E_i)$ is the neutron yield of element j in isolation (see Eq. (3.3)). Thus the (α,n) yield of a compound (mixture) is the sum of the yields of its elements weighted by relative contributions of the elements to the total stopping power of the compound.

The use of 8 MeV mass stopping power was selected because the overwhelming contribution to the neutron yield comes from high energy α -particles and the relative stopping power of elements are nearly independent of the α -energy in this energy region [Hea89]. In Table 3.4 the 8 MeV mass stopping powers of elements used in this work are shown. Although hydrogen has a negligible neutron yield, it is included in the table because its stopping power value is important for many materials. In this work the data on neutron yield of elements in isolation, in units of neutron/ α , is taken from a compilation by Heaton *et al.* [Hea89, Hea02].

Table 3.4 Mass Stopping power of elements at 8 MeV.

Element	Mass Stopping Power $(\frac{\text{MeV.cm}^2}{\text{mg}})$	Element	Mass Stopping Power $(\frac{\text{MeV.cm}^2}{\text{mg}})$
Ca	0.438	Na	0.511
C	0.583	Fe	0.351
O	0.541	Ti	0.383
Mg	0.486	P	0.443
Si	0.462	S	0.442
Al	0.449	H	1.587
K	0.428		

Gran Sasso rock consists mainly of CaCO_3 and MgCO_3 , with a density of $2.71 \pm 0.05 \text{ g/cm}^3$ [Cat86]. The weight percentage of the elements is given in Table 3.5.

Table 3.5 Chemical composition of LNGS rock.

Element	Ca	C	O	Mg	Si	Al	K
% Weight	30.29	11.88	47.91	5.58	1.27	1.03	1.03

Due to the presence of a certain type of rock, called “roccia marnosa nera”, the contaminations of ^{238}U and ^{232}Th in hall A rock are about ten and thirty times higher respectively than those of hall C [Bel85] as shown in Table 3.6.

Table 3.6 ^{238}U and ^{232}Th activities in LNGS rock.

Hall	Activities (ppm)	
	^{238}U	^{232}Th
A	6.80	2.167
B	0.42	0.062
C	0.66	0.066

Since there is no data on the chemical composition of Gran Sasso concrete available in the literature, several samples were taken from different places in the laboratory, including from hall A, where the CRESST setup is now located. The concrete samples were then analyzed at the laboratory of the *Lehrstuhl für Baustoffkunde und Werkstoffprüfung* at the department of civil engineering of the Technische Universität München. No significant variations were found in the chemical composition of the samples, which

leads to the conclusion that all halls in Gran Sasso are layered with the same type of concrete. The typical water content in the concrete is 12%, with a possible variation of 4% at most (in most cases the variation is smaller). The weight percentage of elements in concrete with 8% water content (hereafter “dry concrete”) is shown in Table 3.7. The ^{238}U and ^{232}Th contaminations are 1.05 ± 0.12 ppm and 0.656 ± 0.028 ppm [Bel91] respectively. The density is between 2.3-2.5 g/cm³, depending on the water content.

Table 3.7 Chemical composition of LNGS dry concrete.

Element	Ca	C	O	Mg	Si	Al	K	Na	Fe	Ti	P	S	H
% Weight	34.06	7.99	48.43	0.85	3.86	0.9	0.54	0.6	0.43	0.04	0.04	0.16	0.89

To get the neutron production rate we have to multiply the yield with the number of α emitters per decay chain, the number of α 's emitted by each emitter per unit time, and the concentration of ^{238}U and ^{232}Th in the rock (concrete). It is assumed in this work, that ^{238}U and ^{232}Th are in secular equilibrium with their daughter products. Table 3.8 shows all α emitters in the ^{238}U and ^{232}Th chains, the emitted α energies and the branching ratios. Neutrons produced per unit mass per year by (α, n) reactions with the elements of the rock in hall A, hall C and also in dry and wet concrete are presented in Table 3.9, Table 3.10, Table 3.11 and Table 3.12. In these tables separate contributions of neutron production from ^{238}U and ^{232}Th are shown together with the total contribution.

Table 3.8 α -Emitters in the ^{238}U and ^{232}Th chains.

^{238}U -chain			^{232}Th -Chain		
α -Emitter	Branching ratio	α -Energy	α -Emitter	Branching ratio	α -Energy
U-238	1	4.20	Th-232	1	4.01
U-234	1	4.78	Th-228	1	5.42
Th-230	1	4.69	Ra-224	1	5.69
Ra-226	1	4.78	Rn-220	1	6.29
Rn-222	1	5.49	Po-216	1	6.78
Po-218	1	6.00	Bi-212	0.3594	6.09
Po-214	1	7.69	Po-212	0.64	8.79
Po-210	1	5.30			

The energy of the emitted neutron is dependent on the α energy, the reaction energy Q , and the neutron emission angle. It was calculated under the following assumptions:

Table 3.9 Neutron yields from (α, n) interactions in hall A rock.

Element	U-238 yield (n/y/g rock)	Th-232 yield (n/y/g rock)	Total elemental yield (n/y/g rock)	% yield
O	7.80E-1	9.00E-2	8.8E-1	20.03
Si	5.00E-2	1.00E-2	6.00E-2	1.36
Al	3.00E-1	5.00E-2	3.50E-1	7.98
Mg	2.01E+0	3.00E-1	2.31E+0	52.66
K	7.00E-2	2.00E-2	9.00E-2	2.02
Ca	2.00E-1	5.00E-2	2.40E-1	5.54
C	4.00E-1	5.00E-2	4.60E-1	10.41
Total U-238	3.82E+0			
Total Th-232		5.60E-1		
Total yield in Rock			4.38E+0	

Table 3.10 Neutron yields from (α, n) interactions in hall C rock.

Element	U-238 yield (n/y/g rock)	Th-232 yield (n/y/g rock)	Total elemental yield (n/y/g rock)	% yield
O	7.62E-2	2.82E-3	7.90E-2	20.38
Si	4.95E-3	2.57E-4	5.21E-3	1.34
Al	2.90E-2	1.54E-3	3.05E-2	7.88
Mg	1.95E-1	9.03E-3	2.04E-1	52.64
K	7.14E-3	4.57E-4	7.60E-3	1.96
Ca	1.91E-2	1.38E-3	2.05E-2	5.29
C	3.91E-2	1.61E-3	4.07E-2	10.51
Total U-238	3.70E-1			
Total Th-232		1.71E-2		
Total yield in Rock			3.88E-1	

- (i) the interaction take place at the initial α energy
- (ii) the neutron is emitted at 90°
- (iii) the residual nucleus is produced in its ground state.

Under these assumptions, neutrons are produced at maximum energies which can be determined by using simple Eq. (3.5):

$$E_n = \frac{MQ + E_\alpha(M - M_\alpha)}{(M_n + M)} \quad (3.5)$$

where M is the mass of the final nucleus, M_n and M_α are the masses of neutron and the α particle respectively, and E_α is the initial α energy.

Table 3.11 Neutron yields from (α, n) interactions in dry concrete (8% water content).

Element	U-238 yield (n/y/g conc.)	Th-232 yield (n/y/g conc.)	Total elemental yield (n/y/g conc.)	% yield
O	1.22E-1	2.84E-2	1.50E-1	29.75
Si	2.38E-2	7.77E-3	3.16E-2	6.26
Al	4.01E-2	1.34E-2	5.35E-2	10.60
Mg	4.70E-2	1.37E-2	6.07E-2	12.02
K	5.93E-3	2.39E-3	8.31E-3	1.65
Ca	3.40E-2	1.55E-2	4.95E-2	9.81
C	4.16E-2	1.08E-2	5.24E-2	10.38
Na	7.31E-2	2.35E-2	9.65E-2	19.12
Fe	5.54E-4	3.99E-4	9.53E-4	0.19
P	3.08E-4	1.27E-4	4.35E-4	0.09
S	2.41E-4	9.49E-5	3.36E-4	0.07
Ti	2.23E-4	1.12E-4	3.35E-4	0.07
Total U-238	3.89E-1			
Total Th-232		1.16E-1		
Total yield in concrete			5.05E-1	

Since high energy neutrons would be more dangerous for the experiment, the aforementioned assumptions give a conservative estimate, because it produces the hardest possible spectrum. In reality the spectrum will be softer.

The threshold energy E_{th} for an (α, n) reaction is the minimum kinetic energy the impinging α particle must have (in the laboratory system) in order to make the reaction energetically possible. For endothermic reactions, the threshold energy is:

$$E_{th} = -[(M_n + M_\alpha/M_1)Q] \quad (3.6)$$

where M_1 and M_α are the masses of the target nucleus and of α particle respectively. The threshold energy is zero for exothermic reactions, *i.e.* reactions with positive Q .

The highest energy among naturally emitted α particles is 8.79 MeV, which comes from the decay of ^{212}Po . Hence, for some elements in the rock or concrete there are isotopes that can not participate in the (α, n) reactions, because of their high E_{th} (*e.g.* ^{16}O , ^{28}Si , ^{24}Mg , and ^{40}Ca). For each element calculations of neutron energies were therefore done for all isotopes that are not closed for (α, n) interactions. Finally, neutron mean energies of elements were calculated according to the relative abundances of the “open” isotopes as shown in Table 3.13 for different α energies .

Table 3.12 Neutron yields from (α, n) interactions in wet concrete (16% water content).

Element	U-238 yield (n/y/g conc.)	Th-232 yield (n/y/g conc.)	Total elemental yield (n/y/g conc.)	% yield
O	1.27E-1	2.96E-2	1.57E-1	33.02
Si	2.13E-2	6.93E-3	2.82E-2	5.94
Al	3.61E-2	1.21E-2	4.82E-2	10.15
Mg	4.21E-2	1.23E-2	5.44E-2	11.46
K	5.29E-3	2.13E-3	7.42E-3	1.56
Ca	3.04E-2	1.38E-2	4.42E-2	9.31
C	3.72E-2	9.62E-3	4.68E-2	9.86
Na	6.58E-2	2.11E-2	8.69E-2	18.30
Fe	4.97E-4	3.58E-4	8.55E-4	0.18
P	2.97E-4	1.23E-4	4.19E-4	0.09
S	2.18E-4	8.58E-5	3.04E-4	0.06
Ti	2.15E-4	1.08E-4	3.23E-4	0.07
Total U-238	3.66E-1			
Total Th-232		1.08E-1		
Total yield in concrete			4.75E-1	

Table 3.13 Neutron energy of elements for different α -energies, averaged over “open” isotopes.

α -Energy (MeV)	Neutron Energy (MeV)												
	O	Si	Al	Na	Fe	Mg	K	Ca	C	P	S	Ti	
²³⁸ U-chain	4.20	1.79	1.09		1.52	3.74		0.76	4.08		0.69	0.62	
	4.78	2.24	1.58	0.46	0.05	2.05	4.22		1.28	4.49		1.16	1.14
	4.69	2.17	1.51	0.39	0.00	1.97	4.15		1.20	4.43		1.08	1.06
	4.78	2.24	1.59	0.47	0.06	2.05	4.23		1.29	4.50		1.17	1.15
	5.49	2.79	1.43	1.06	0.63	2.45	4.82	0.57	1.92	4.99		1.78	1.79
	6.00	3.18	1.87	1.49	1.05	2.92	5.24	1.02	2.38	5.36		2.22	2.07
	7.69	4.48	3.30	2.90	2.42	1.07	6.64	2.52	3.18	6.54	0.11	1.56	3.59
	5.30	2.64	1.27	0.90	0.48	2.28	4.66	0.40	1.75	4.86		1.62	1.62
²³² Th-chain	4.01	1.65	0.93		1.35	3.59		0.59	3.95		0.53	2.35	
	5.42	2.73	1.38	1.00	0.58	2.38	4.76	0.51	1.86	4.95		1.72	1.73
	5.69	2.94	1.60	1.22	0.79	2.63	4.98	0.74	2.09	5.13		1.95	1.96
	6.29	3.40	2.11	1.73	1.28	3.18	5.48	1.28	2.63	5.56		2.47	2.33
	6.78	3.78	2.53	2.14	1.68	2.12	5.89	1.71	3.07	5.90		0.77	2.77
	6.09	3.25	1.94	1.56	1.12	3.00	5.31	1.10	2.45	5.42		2.30	2.15
	8.79	5.33	4.23	3.82	3.32	2.08	7.55	3.49	4.17	7.32	1.05	2.51	4.58

Finally, the yields of all elements were summed up in 0.5 MeV energy bins to get the energy spectra of neutrons from (α, n) reactions as shown in Figure 3.3 for hall A rock, hall C rock, and dry concrete. High energy neutrons are contributions of magnesium and carbon.

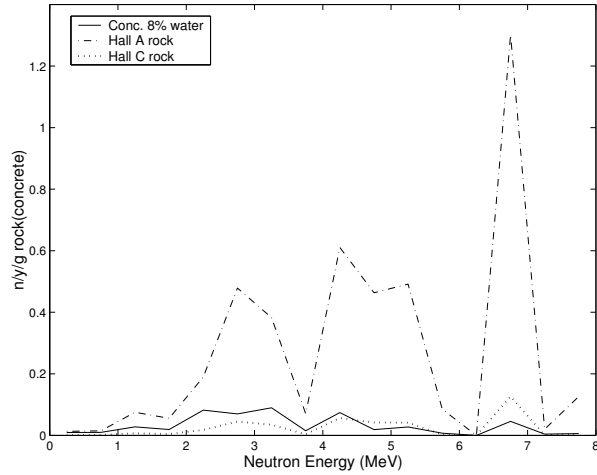


Fig. 3.3 Energy spectra of neutrons from (α, n) reactions.

3.2.3 Flux of Low Energy Neutrons at LNGS

To get the flux of low energy neutrons inside the halls, Monte Carlo simulations have to be done to transport neutrons produced by fission and (α, n) reactions through the rock and concrete and diffuse them inside the halls. All of the simulations for low energy neutrons in this work were done using the MCNP4B (Monte Carlo N-Particles version 4B) code from Los Alamos [Bri97].

First, the typical depth of the rock and concrete should be determined in order to see their characteristics and to get an idea of a reasonable thickness of rock and concrete to be used in the simulations. Simulations with different thicknesses of rock and concrete were done to get fluxes of neutrons coming into hall A and hall C. In these simulations back scattering was not taken into account (neutrons were terminated when entering the halls). The fluxes of neutrons produced by fission and (α, n) reactions in hall A rock and dry concrete are shown by points in Figure 3.4 for all energies and for $E > 1$ MeV separately. The lines are fits of the points with the following function:

$$y = Y_{max}(1 - \exp(-x/C)) \quad (3.7)$$

where x is thickness and C is the typical depth.

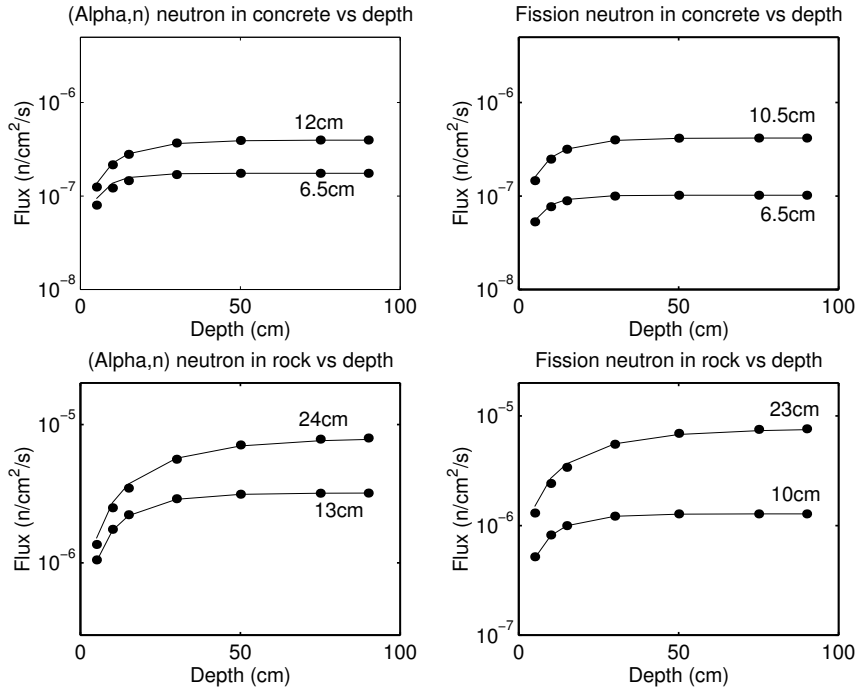


Fig. 3.4 Typical depths of neutrons from (α, n) and fission reactions in hall A rock (lower pictures) and in dry concrete (upper pictures). The upper curve in each picture is the contribution from neutrons with all energies, the lower curve is from neutrons with energies above 1 MeV.

It is clear that neutrons with $E > 1$ MeV come from more or less 7 cm and 13 cm of concrete and rock respectively. As the thickness of concrete layer in Gran Sasso is not less than 30 cm (in some places even around 1m), it can be expected that the bulk of the total flux in the laboratory is given by neutrons produced in the concrete.

The typical size of the halls in Gran Sasso is 100 m x 20 m x 20 m. For the simulations of the low energy neutron flux, rock 2 m thick was used. The thickness of the concrete layer in the laboratory is 45 cm below the floor and 35 cm elsewhere. Both in the rock and concrete roughly half of the neutrons come from (α, n) reactions and the other half from fission reaction. The calculated fluxes of low energy neutrons (after scattering inside the halls) are shown in Table 3.14 for hall A with 8% (dry) and 16% (wet) water content in the concrete, for hall C with dry concrete, and the measurement by Belli et al. [Bel89] in Hall A as comparison.

It is clearly seen that the spectrum and total flux of this present work are in good agreement with those of measurement. No significant difference between hall A and hall C is seen, although the neutron production rate in hall A rock is more than ten times higher than that of hall C. The concrete indeed reduces the neutron flux from the rock significantly and neutrons

Table 3.14 Neutron flux in hall A and hall C.

Energy (MeV)	Neutron Flux ($10^{-6} \text{n/cm}^2 \text{s}$)			
	Hall A		Hall C	Measurement
	(8% water in conc.)	(16% water in conc.)	(8% water in conc.)	[Bel89]
1 - 2.5	0.35	0.18	0.27	0.38 ± 0.01
2.5 - 5	0.18	0.12	0.15	0.27 ± 0.14
5 - 10	0.05	0.03	0.03	0.05 ± 0.01

coming into the halls are mainly those produced in the concrete layer. The flux in Hall A with wet concrete is lower than with dry concrete. This is understandable, because more water means more hydrogen that does not give additional neutron yield but contributes to the total stopping power. Besides, wet concrete would moderate neutrons more effectively than dry concrete.

3.3 Neutron Background in the Current Setup of CRESST: The Need for Neutron Shielding

3.3.1 MCNP4B and Recoil Spectrum

To get a spectrum of neutron-induced recoils in the target, a Monte Carlo code is needed to simulate the random processes. As mentioned in the previous subsection, MCNP4B was used to transport and to get the neutron flux in the laboratory. This code, that transports also photons and electrons, was originally developed for criticality calculation. It is a reliable code, widely used for radiation protection and dosimetry. In such calculations one usually does not need any information on event-by-event basis. Therefore, simulation results presented as fluxes or currents are enough, and MCNP wonderfully accommodates this purposes.

But getting a recoil spectrum with MCNP is another story, because it is not given as a “ready to use” facility in the code. An additional output file, which gives information on event-by-event basis, is given in a file of raw data called PTRAC file. In order to be able to extract the needed information one has to work with this raw data, which is quite laborious. Besides, the manual does not give quite clear information on this and some bugs were found in the way MCNP4B writes the interaction types on PTRAC. Given some guidance by the MCNP developer team [McK01], the bugs were fixed. The PTRAC files were read with MATLAB routines written for this purpose.

To check the reliability of MCNP4B in simulating nuclear recoils induced by elastically scattered neutrons, a test simulation was done, in which W

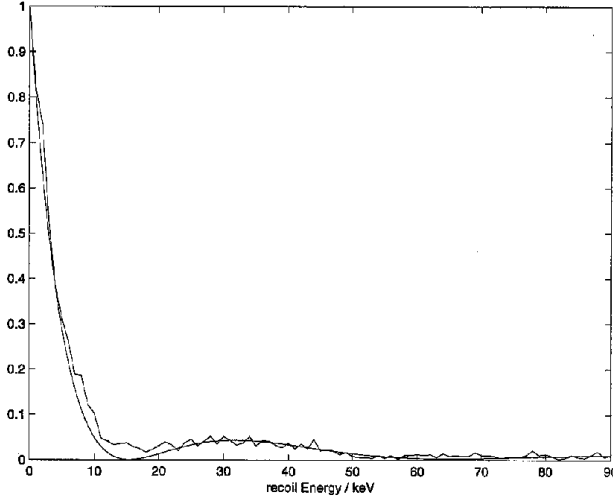


Fig. 3.5 Comparison of recoil spectrum of W hit by 10 MeV neutrons: simulation with MCNP4B (broken line) and theoretical calculation (smooth line).

nuclei were hit by 10 MeV neutrons. The recoil spectrum obtained from the simulation was then compared with the one obtained from theoretical calculation. The two spectra are in good agreement, as shown in Figure 3.5.

3.3.2 Neutron Background Expectation in CRESST I and in CRESST II without Neutron Moderator

To estimate the neutron background in the present setup of CRESST (Pb/Cu shields without neutron moderator) a simple geometry (see Figure 3.6), which consist of Pb/Cu shield and a single cube detector crystal ($4\text{ cm} \times 4\text{ cm} \times 4\text{ cm}$), was used. The dimension of the lead shield (outer surface) is $130\text{ cm} \times 130\text{ cm} \times 136\text{ cm}$ and the thickness is 20 cm. Inside the lead is 15 cm thick copper and inside the copper is the experimental cavity, in which the detector crystal is placed. Neutrons with the measured energy spectrum [Bel89] were generated uniformly at the outer surfaces of the lead shield, with a uniform angular distribution in 2π .

The recoil spectrum obtained from simulation for CRESST phase I, in which sapphire was used, is shown in Figure 3.7. The CRESST collaboration reported a background rate of 0.3 cts/kg/day at 100 keV [Ang02] (see discussion in Chapter 2). Although there is only poor statistics at energy around 100 keV in the simulated spectrum in Figure 3.7, it is seen that the neutron background rate at this energy is about ten times lower than the background rate reported by CRESST. Hence, with the sensitivity reached by CRESST I neutrons were not a dominant background.

In CRESST phase II CaWO₄ is being used instead of sapphire. To study whether neutron background would cause a problem for the second phase of

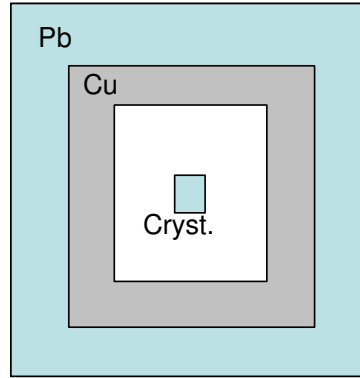


Fig. 3.6 Simple geometry with Pb/Cu shields used in the simulations.

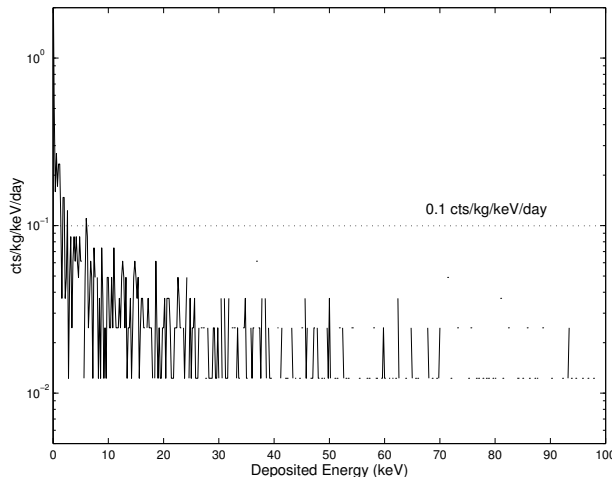


Fig. 3.7 Recoil spectrum of sapphire in CRESST phase I, obtained from simulation with simple Pb/Cu shields setup (see text).

the experiment, similar simulations had been performed with CaWO_4 as a target crystal. Both the measured spectrum [Bel89] and the spectrum obtained in this work were used in the simulations.

As shown in Figure 3.8 the simulation with the spectrum in hall A for dry concrete gives 69 cts/kg/y in the energy range of 15-25 keV for the current setup, while the simulation with the measured spectrum [Bel89] gives 47 cts/kg/y. Here 15 keV is the energy threshold of the detector system (see Chapter 2). In CRESST phase II, 60 GeV WIMPs with a cross section as claimed in [Ber00] would give 55 cts/kg/y in the same energy range. This means, it is impossible for CRESST II to check the DAMA evidence without a neutron moderator.

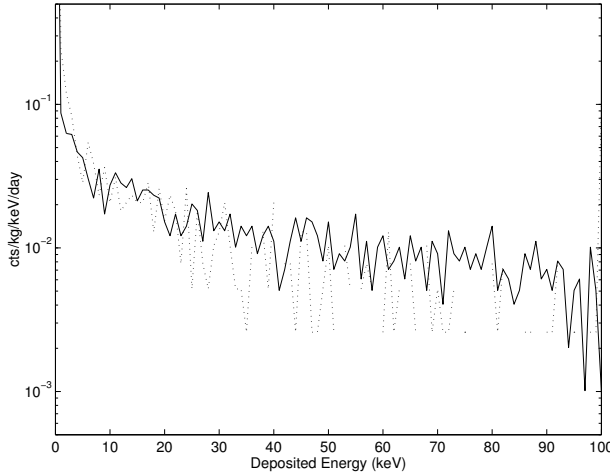


Fig. 3.8 Recoil spectrum of CaWO_4 in CRESST phase II with the simple Pb/Cu shield setup (see text). Solid line: simulation with the calculated spectrum in hall A (dry concrete), dotted line: simulation with measured spectrum [Bel89].

3.4 Neutron Moderator

3.4.1 Efficiency of Shielding and Alternatives

Material with a high hydrogen content is ideal to slow down and then capture neutrons. Two kinds of materials commonly used as neutron moderator, namely polyethylene and borated polyethylene (10% B), had been studied in this work. Neutron moderators of different thicknesses were placed outside the lead shield to determine the efficiency of the shielding. Similar to previous simulations, neutrons with the measured energy spectrum [Bel89] were generated uniformly at the outer surfaces of the neutron moderator, with a uniform angular distribution in 2π . Fluxes of neutrons entering the CaWO_4 crystal with an energy above 70 keV are shown in Table 3.15. Here 70 keV is the minimum neutron energy needed to deposit 15 keV in the crystal (in a head on collision with oxygen nucleus), which is the threshold of the detector system.

In the simulations the “albedo” has been taken into account, which means neutrons were allowed to scatter inside the experimental cavity and be counted again. The number of neutrons coming more than once into the experimental cavity are about 40% of the total flux. Almost no difference are found between the fluxes obtained from simulations with polyethylene and with borated polyethylene. Boron captures neutrons and produces 0.42 MeV gammas. Therefore, borated polyethylene is usually used to capture neutrons at defined (desired) places, and gammas are the signature for the neutrons capture. However, the advantage of using borated polyethylene is not relevant for CRESST, and therefore only polyethylene was used

Table 3.15 Flux of neutrons entering the CaWO₄ crystal with energies above 70 keV.

Thickness of shielding (cm)	Neutron Flux (n/cm ² s)	
	Polyethylene	Borated PE (10% B)
10	4.40 x 10 ⁻³	4.61 x 10 ⁻³
15	8.36 x 10 ⁻⁴	8.73 x 10 ⁻⁴
20	2.01 x 10 ⁻⁴	2.01 x 10 ⁻⁴
30	1.55 x 10 ⁻⁵	1.55 x 10 ⁻⁵

in the further simulations.

The neutron background count rates in the crystal for a deposited energy range of 15–25 keV are summarized in Table 3.16 for setups with different thicknesses of polyethylene. As the input spectra the measured spectrum from [Bel89] and the calculated spectrum obtained from simulations with dry concrete were used. Figure 3.9 shows the recoil spectrum in the setup with 50 cm polyethylene, obtained from a simulation with the measured spectrum [Bel89] and with the calculated spectrum from this work. From now on the setup with 50 cm polyethylene will be used as a “standard” in comparing count rates from different cases.

Table 3.16 Neutron background count rates in the 15–25 keV energy range in CaWO₄ for different thicknesses of polyethylene.

Thickness of shielding (cm)	Count Rate (cts/kg/day))	
	Sim. with measured spectrum [Bel89]	Sim. with dry concrete
No PE	1.30 x 10 ⁻¹	1.89 x 10 ⁻¹
10	6.60 x 10 ⁻²	
20	8.17 x 10 ⁻³	
30	1.60 x 10 ⁻³	
40	4.37 x 10 ⁻⁴	
50	9.96 x 10 ⁻⁵	1.64 x 10 ⁻⁵
60	2.36 x 10 ⁻⁵	

In spite of the agreement of the calculated and the measured total flux (see Table 3.14), the count rates obtained with these two spectra are different, especially for the setup with 50 cm polyethylene, where the count rate obtained with the calculated spectrum is seven times lower than that obtained with the measured spectrum. This is due to the fact that the detailed shapes of these two spectra (see Figure 3.10) are different. The measured flux [Bel89] is given as integral fluxes over quite large energy

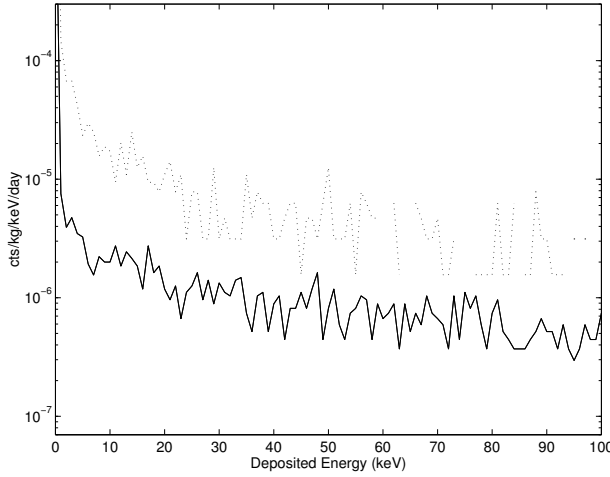


Fig. 3.9 Recoil spectrum in CaWO_4 in a setup with Pb/Cu and 50 cm of polyethylene. Solid line: obtained with the dry concrete spectrum, dotted line: obtained with the measured spectrum [Bel89].

bins. In the simulations the energy was sampled with the same probability in these large bins. This makes the spectrum look harder than it really is. On the other hand, the calculated spectrum was given as integral fluxes of smaller bins, and therefore more detailed. The higher number of neutrons with an energy above 7 MeV in the measured spectrum could survive the moderator and therefore would give more counts in the crystal. This fact shows the importance of the detailed knowledge of the neutron spectrum at the experimental site.

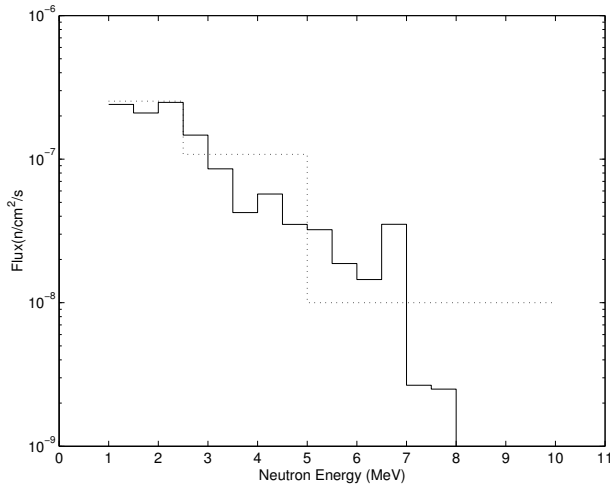


Fig. 3.10 Spectra of low energy neutrons from the rock/concrete used in simulations. Solid line: calculated spectrum, dotted line: measured spectrum [Bel89].

3.4.2 *Simulation with a Realistic Setup*

Simulations with a more realistic setup as shown in Figure 3.11 has been done with the measured spectrum [Bel89]. In the first simulation the polyethylene thickness was taken to be 30 cm, while in the second simulation it was 30 cm at the bottom of the setup and 60 cm elsewhere.

The recoil spectra obtained from simulations with the two setups are shown in Figure 3.12. The count rate at 15-25 keV for the setup with 30 cm polyethylene is 1.27×10^{-3} cts/kg/day (0.46 cts/kg/y), which is a factor of around 100 times lower than the count rate for the simple setup without neutron moderator in the same energy range. This means, that with 30 cm polyethylene as neutron moderator neutrons will definitely not prohibit CRESST from checking the DAMA result. If higher sensitivity is aimed for, of course the idea is to use a thicker polyethylene shield. The setup with 30 cm polyethylene at the bottom and 60 cm elsewhere would give 8.35×10^{-5} cts/kg/day(0.03 cts/kg/y). But it will be shown at the end of this chapter and in the next chapter, that with thicker polyethylene, contributions of neutrons from other origins will become more important.

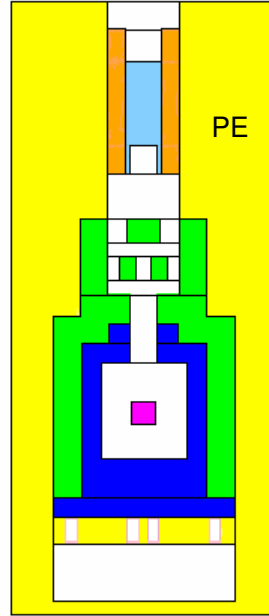


Fig. 3.11 More realistic setup with polyethylene used in the simulations.

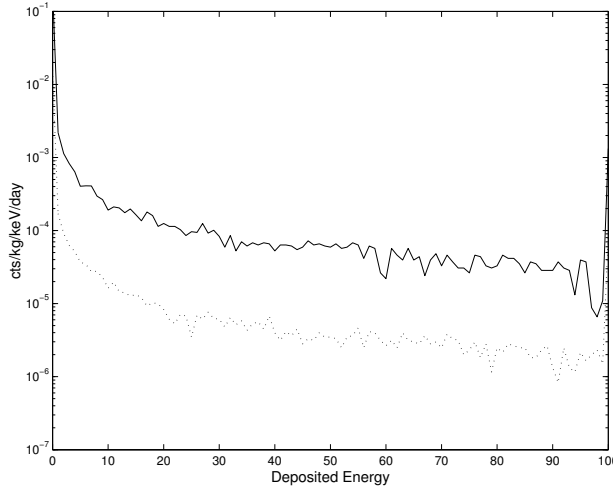


Fig. 3.12 Recoil spectra obtained with a measured spectrum [Bel89] for a realistic setup. Solid line: 30 cm polyethylene, dotted line: 30 cm polyethylene at the bottom of the setup and 60 cm elsewhere.

3.5 Water Content Variation

It can be expected, that the water content in the surrounding rock and concrete of the Gran Sasso halls changes throughout the year. As mentioned at the beginning of this chapter, another motivation to study low energy neutron was to investigate the possibility that the count rate would vary if the humidity in the vicinity of experimental setup changes. The influence of changing water content in the concrete on the count rates expected in the CaWO₄ crystal has been studied. Two extreme cases were considered: dry concrete with 8% water content and wet concrete with 16% water content.

In Figure 3.13 the recoil spectra for the simple setup without neutron moderator are shown. The count rate at 15-25 keV for the simulation with dry concrete is 69 cts/kg/y, while using wet concrete gives 37 cts/kg/y, which is almost two times lower. To make the difference between the two spectra clearer, the y-axis is linear and not logarithmic as in the other plots.

Simulations using 50 cm of polyethylene as neutron moderator have also been performed. The recoil spectra for the two extreme cases are shown in Figure 3.14. The use of dry concrete would give a count rate of 6×10^{-3} cts/kg/y, which is 50% higher than the rate for wet concrete, (4×10^{-3} cts/kg/y). Again, here the y-axis is linear.

As previously mentioned, the typical water content of concrete is 12%. A variation of up to maximum 4% is possible, but the most probable case is a variation of about 1%. With such a small variation in the humidity, one can expect a change of less than 10% in the count rate.

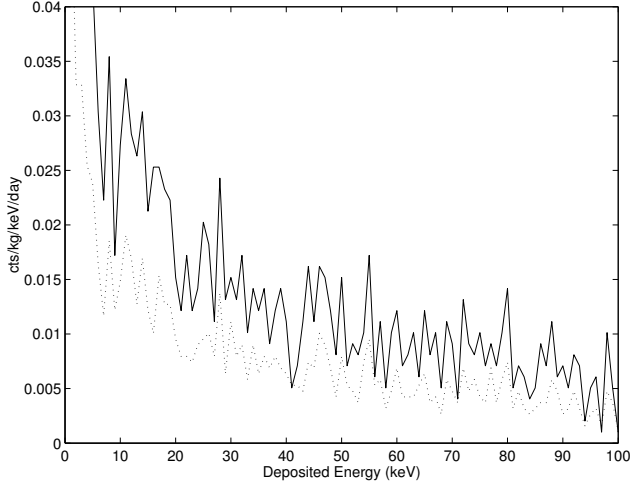


Fig. 3.13 Variation in the count rate due the change of humidity in the the concrete. Setup: Simple geometry (Pb/Cu shields without neutron moderator). Solid line: dry concrete, dotted line: wet concrete.

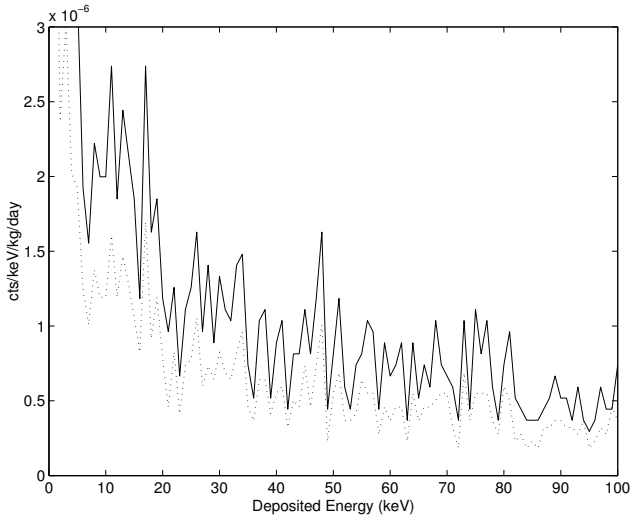


Fig. 3.14 Variation in the count rate due to the change of humidity in the concrete. Setup: Simple geometry with neutron moderator (Pb/Cu shields with 50 cm polyethylene). Solid line: dry concrete, dotted line: wet concrete.

There is still a long way to go, if one wants to relate this humidity variation with the annual modulation as reported by DAMA. To mimic a WIMP signal modulation a seasonal effect has to fulfill several requirements like one year period, a phase that peaks around $\simeq 2^{nd}$ June, modulation amplitude of $\lesssim 7\%$, and some other conditions. One may expect that the laboratory is more humid during summer, while the snow from winter is

melting and giving rise to the water content underground. More water content means less neutron count rate in the detector, which is the opposite of the effect expected for a WIMP signal. But the concrete layer has a different characteristic than the rock. The concrete layer in Gran Sasso is made of hi-tech concrete, used to prevent water from the rock to come into the laboratory. So, there is a time delay (can be months) for the water to come into the halls. It may happen therefore, that during winter the concrete layer is more humid than during summer. But once again, there is no way to prove this argument but by monitoring the water content in the concrete throughout the year. For the moment, it is safe simply to say, that neutron background count rate does change with the variation of water content in the experimental vicinity.

3.6 Neutrons Produced by Fission in the Lead Shield

The use of radio pure material for the experimental setup and shield in the rare event searches is mandatory. However, it is still necessary to check, whether the low remaining activity is really harmless for CRESST II.

Allesandrello *et al.* [All91] reported a ^{238}U contamination of $< 2 \text{ ppb}$ in roman lead and $< 12 \text{ ppb}$ in low activity lead. In this work a contamination of 0.1 ppb was assumed. Only fission-induced neutrons were considered, because contribution of (α, n) reactions in lead is not significant. Neutrons with energies following the Watt spectrum (see Eq. (3.1)) were generated uniformly inside the whole volume of the lead shield. An isotropic (4π direction) angular distribution was taken.

It was found that neutrons from this origin would give 0.2 cts/kg/y in the energy range of $15\text{-}25 \text{ keV}$, which is a factor of around 300 lower than the rate expected from low energy neutrons from the rock without neutron moderator. This means, neutrons from ^{238}U contamination in the Lead shield do not cause any problem from CRESST II with the current setup. Nevertheless, the rate from this type of neutrons is around 5 times higher than the rate expected from low energy neutrons from the rock/concrete after moderated by 50 cm of polyethylene (see Figure 3.15).

It is clear, that even a very low contamination in the lead shield can still be dangerous for the experiment, especially because it is very close to the detector of course. Higher count rate is expected if the contamination of the lead is higher than the assumed number. Additional neutron flux can be expected from the copper and polyethylene shields. The contribution of the latter might be negligible, because neutrons will be moderated by polyethylene. To know the real contribution of neutrons from this origin, it would be best to measure the contamination in the shielding materials used in CRESST, as has been done for example by the EDELWEISS collaboration with its lead shield. Assuming an equilibrium of ^{238}U with its daughter

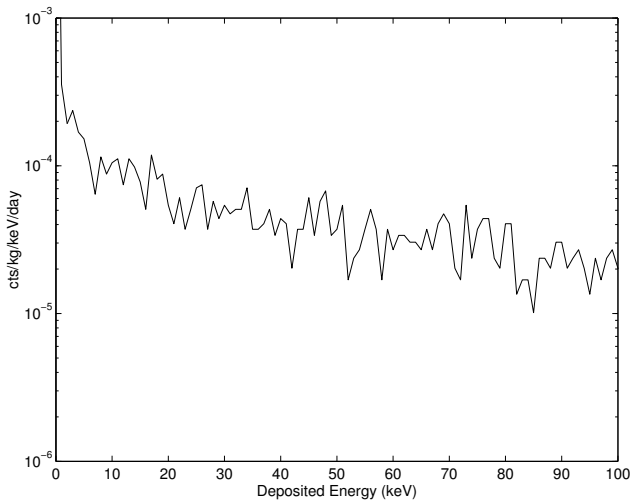


Fig. 3.15 Recoil spectrum due to neutrons produced by spontaneous fission in the lead shield.

products the collaboration found an upper limit of 0.7 ppb in the most recent measurements. Previous measurements made on another lead gave 0.1 ppb [Ger03].

Chapter 4

Muon-induced Neutron Background

In general, the production rate of muon-induced neutrons at the depth of $3000 - 4000$ m w.e., where many rare event experiments are located, is about three orders of magnitudes lower than that of low energy neutrons from activity of the experimental environment. However, muon-induced neutron flux can be important for experiments attempting to reach high sensitivity like WIMP searches. The energy spectrum of muon-induced neutrons is hard, extending to the GeV range. Fast neutrons can propagate and reach a detector at large distances, far from the associated muon track. They also can transfer a large amount of energy in nuclear recoils, making them visible in dark matter detector. On the contrary, many recoil energies from radioactivity-induced neutrons are too low and fall below the detector threshold. Besides, muon-induced neutrons are more difficult to get rid of. Hydrogen-rich material that works for radioactivity-induced neutrons, will not protect against fast neutrons induced by muons and even by itself be a target for cosmic ray muons.

In this work background induced by neutrons of this type and its importance for CRESST has been studied. This chapter will be started with a general description of muons, the origins, interactions with matter, muons underground, mechanism to produce neutrons, and results of measurements. Then a study on muon-induced neutrons and simulations relevant for CRESST will be discussed.

4.1 Muons and Cosmic Rays

Cosmic ray particles, that hit the Earth’s atmosphere at a rate of about $1000/(m^2 s)$, are ionized nuclei: about 90% protons, 9% alpha particles and the rest heavier nuclei [Gai90]. “Primary” cosmic rays consist of particles accelerated at astrophysical sources, *e.g.* electrons, protons, helium and other nuclei synthesized in stars, while “secondary” cosmic rays are particles produced in interactions of the primaries with interstellar gas (and the

Earth's atmosphere) [Hag02]. According to their origin and energy spectra, cosmic rays can generally be divided into a solar component and a galactic component.

The solar component dominates the low energy range of cosmic rays up to 200 MeV and due to absorption in the Earth's atmosphere can not contribute to the muon flux underground. On the contrary, the galactic component may have energies up to about 10^{20} eV ("Greisen-Zatsepin-Kuzmin Cut-Off" [Gre66, Zat66b]) or even above. The differential energy spectrum of the major component of cosmic rays from ~ 10 GeV up can be described by the inverse power law in energy [Gai90]:

$$\frac{dN}{dE} \propto E^{-(\gamma+1)} \quad (4.1)$$

The spectrum continues up to $E \sim 10^6$ GeV with $\gamma \approx 1.7$. Above this energy the spectrum steepens to $\gamma \approx 2.0$.

The primary nuclei of cosmic rays lose their energy by inelastic interaction with particles in the atmosphere and produce secondary particles like protons, neutrons and pions. In smaller numbers other particles like kaons and charm particles are also produced.

Muons are products of the decay of charged pions and kaons high in the atmosphere (typically 15 km), where the density is low. In lower height and therefore higher density of the atmosphere pions disappear mainly through nuclear interactions. A much less frequent source of muons is the decay of short lived particles like charm particles, and muons produced by this channel are usually called "prompt" muons. Because of the short live times of these charm particles there is for them no competition between interaction and decay, and the prompt muon energy spectrum has almost the same slope as the primary spectrum. On the contrary, the flux of ordinary muons (those from pions and kaons) decreases with increasing muon energy. Because of their flatter energy spectrum prompt muons will eventually dominate the muon flux at very high muon energy ($E > 1000$ TeV) despite the much lower production of their parents compared to pions and kaons. Unlike the flux of muons from pions and kaons, which strongly depends on zenith angle, prompt muon flux is isotropic [Gai90]. In addition to the two production mechanisms, muon can also be produced by the charged current interactions of muon neutrinos in the rock surrounding an experiment underground.

The fact that there are more protons than neutrons in the primary spectrum is reflected in the muon charge ratio $K_\mu = N(\mu^+)/N(\mu^-)$. The charge ratio is between 1.2 and 1.3 from 250 MeV up to 100 GeV [DeP93].

After being produced in the atmosphere muons lose about 2 GeV to ionization before reaching the ground. Muons are the most numerous charged particles at sea level. Their energy and angular distribution reflect a convolution of the production spectrum, the energy loss in the atmosphere, and

the decay. The mean energy of muons at the ground is $\approx 4 \text{ GeV}$. The energy spectrum is almost flat below 1 GeV, steepens gradually in the $10 - 100 \text{ GeV}$ range reflecting the primary spectrum, and steepens further at higher energies because pions with $E_\pi \gtrsim 115 \text{ GeV}$ tend to interact in the atmosphere before they decay. Asymptotically ($E \gg 1 \text{ TeV}$), the energy spectrum of atmospheric muons is one power steeper than the primary spectrum [Hag02]. The integral intensity of vertical muons above 1 GeV/c at sea level is $\approx 70 \text{ m}^{-2}\text{s}^{-1}\text{sr}^{-1}$ [DeP93]. The overall angular distribution at the ground is $\propto \cos^2\theta$ (where θ is zenith angle), which is characteristic for muons with $E_\mu \sim 3 \text{ GeV}$. Muons are nearly stable. An approximate formula for the muon energy spectrum at sea level at zenith angle θ , which is valid when the muon decay is negligible ($E_\mu > 100 \text{ GeV}/\cos\theta$) and the curvature of the Earth can be neglected ($\theta < 70^\circ$), is [Gai90]:

$$\frac{dN_\mu}{dE_\mu} \approx \frac{0.14E_\mu^{-2.7}}{\text{cm}^2\text{s sr GeV}} \times \left\{ \frac{1}{1 + \frac{1.1E_\mu \cos\theta}{115 \text{ GeV}}} + \frac{0.054}{1 + \frac{1.1E_\mu \cos\theta}{850 \text{ GeV}}} \right\} \quad (4.2)$$

where the two terms give the contribution of pions and charged kaons. The small contribution from charm and heavier flavors is neglected in Eq. (4.2).

Muons have a small cross section for interaction, and are therefore very penetrating. Nevertheless, they are relatively easy to detect, because they are charged. Interactions of muons with matter will be discussed in the next section.

4.2 Interactions of Muons with Matter

Muons lose energy by ionization and by radiative processes: bremsstrahlung, direct production of e^+e^- pairs, and photonuclear interactions (deep inelastic scattering with nuclei). Those processes are described in the following subsections.

4.2.1 Ionization

The continuous energy loss of muons by inelastic scattering on atomic electrons can be described by the Bethe-Bloch-Formula:

$$\left[\frac{dE_\mu}{dx} \right]_{Ion} = 2\pi N_A r_e^2 c^2 \frac{Z m_e}{A \beta_\mu^2} \left\{ \ln \left[\frac{2m_e P_\mu^2 E'_{max}}{m_\mu^2 I^2(Z)} \right] + \frac{1}{4} \left[\frac{E'_{max}}{E_\mu} \right]^2 - 2\beta_\mu^2 - \delta \right\} \quad (4.3)$$

where r_e is the classical electron radius, N_A the Avogadro Number, Z the atomic number A is the mass number, $I(Z)$ the ionization potential of the medium, m_e and m_μ are the rest masses of electron and the muon, P_μ and E_μ momentum and energy of the muon, $\beta_\mu = P_\mu/E_\mu$, and δ describes a density correction [Ste84]. The maximum energy E'_{max} transferred to an

electron can be described as

$$E'_{max} = 2m_e \frac{P_\mu^2}{m_e^2 + m_\mu^2 + 2m_e E_\mu} \quad (4.4)$$

The energy loss by ionization for relativistic particles can be considered as almost constant. An approximate description of muon energy loss by ionization in standard rock is described with an accuracy of around 5% (for $E_\mu > 10$ GeV) by the following formula [Ros68]:

$$\left(\frac{dE_\mu}{dx} \right)_{Ion} \approx (1.9 + 0.08 \ln E_\mu/\text{GeV}) \text{ MeV}/(\text{g cm}^{-2}) \quad (4.5)$$

In a wide energy range (up to around 200 GeV) average energy loss of muons through ionization can also be described by the famous approximation for minimal-ionizing particles:

$$\left(\frac{dE_\mu}{dx} \right) \approx 2 \text{ MeV}/(\text{g cm}^{-2}) \quad (4.6)$$

While the energy losses through muon-electron scattering with energy transfers below 30 MeV is regarded as a continuous loss by ionization, muon-electron interactions with a higher energy transfer to the electron is handled as a single event with the following interaction cross section [Ros56]:

$$\left[\frac{d\sigma}{d\nu} \right]_{Ion} = 2\pi r_e^2 c^2 \frac{Zm_e}{\beta_\mu^2 E_\mu \nu^2} \left[1 - \beta^2 \frac{\nu}{\nu_{max}} + \frac{\nu^2}{2} \right] \text{ with } \nu_{max} = E'_{max}/E_\mu \quad (4.7)$$

The energy transferred to the electron, ν , is too high in this case, so that electron is knocked out of the atomic shell. Electrons of this type are called *knock-on-electrons* or δ -electrons.

4.2.2 Bremsstrahlung

Muons that are slowed down or deflected in the coulomb field of atomic electrons or atomic nuclei emit bremsstrahlung photons. The following differential cross section describes the process of energy loss due to bremsstrahlung (see [Loh85] and references therein):

$$\left[\frac{d\sigma}{d\nu} \right]_{Brems} = 4\alpha r_e^2 Z(Z+1) \left(\frac{m_e}{m_\mu} \right)^2 \frac{1}{\nu} \left[\frac{4}{3}(1-\nu) + \nu^2 \right] \phi(\delta) \quad (4.8)$$

where $\alpha = 1/137$ is the fine structure constant and ν is the fraction of energy transferred to the photon. The parameter $\delta = m_\mu^2 \nu / (2E_\mu(1-\nu))$ is the minimum momentum transferred to the nucleus. For the function $\phi(\delta)$

the following approximation is used:

$$\phi(\delta) = \ln \left[\frac{m_\mu}{m_e} \frac{(1-a)RZ^{-a-1/3}}{1 + \frac{\sqrt{e}}{m_\mu} \delta RZ^{-1/3}} \right] \quad (4.9)$$

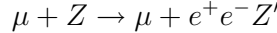
with $a=0$ for $Z \leq 10$ and $a=1/3$ for $Z > 10$, $R=189$ and $e=2.718$. The muon energy loss by bremsstrahlung is obtained by solving the integral in the following equation

$$\left[\frac{dE_\mu}{dx} \right]_{\text{Brems}} = E_\mu \frac{N_A}{A} \int_{\nu_{min}}^{\nu_{max}} \nu \left(\frac{d\sigma}{d\nu} \right)_{\text{Brems}} d\nu = E_\mu b_b(E_\mu) \quad (4.10)$$

with $\nu_{min}=0$ and $\nu_{max}=1 - \frac{3}{4}\sqrt{e} \frac{m_\mu}{E_\mu} Z^{1/3}$. As seen in Figure 4.1 the energy loss due to bremsstrahlung is in a first approximation proportional to the muon energy, *i.e.* the coefficient $b_b(E_\mu)$ is only weakly dependent on the energy.

4.2.3 Direct e^+e^- Pair Production

Direct e^+e^- pair production by muons takes place if a muon-induced virtual photon is absorbed in the coulomb field of an atomic nucleus.



The cross section for this interaction is [Kok71]:

$$\left[\frac{d^2\sigma}{d\nu d\rho} \right]_{\text{Pair}} = \frac{2}{3\pi} (r_e \alpha)^2 Z(Z+1) \frac{1-\nu}{\nu} \left[\Phi_e(E_\mu, \rho, \nu) + \left(\frac{m_e}{m_\mu} \right)^2 \Phi_\mu(E_\mu, \rho, \nu) \right] \quad (4.11)$$

In Eq. (4.11) $\nu = (\epsilon^+ + \epsilon^-)/E$ describes the fraction of energy transferred to the electron-positron pair, $\rho = (\epsilon^+ - \epsilon^-)/(\epsilon^+ + \epsilon^-)$ is the asymmetry parameter of the electron-positron pair, where ϵ^+ and ϵ^- are the energy of e^+ and e^- respectively. The corrections for atom- and nuclear form factors are contained in the functions Φ_e and Φ_μ [Loh85].

By using Eq. (4.11) the energy loss of muons due to direct pair production can be obtained by solving the following integral:

$$\left[\frac{dE_\mu}{dx} \right]_{\text{Pair}} = 2E_\mu \frac{N_A}{A} \int_{\nu_{min}}^{\nu_{max}} \nu \int_0^{\rho_{max}} \left[\frac{d^2\sigma}{d\nu d\rho} \right]_{\text{Pair}} d\rho d\nu = E_\mu b_p(E_\mu) \quad (4.12)$$

with $\nu_{min} = \frac{4m_e}{E_\mu}$, $\nu_{max} = 1 - \frac{3}{4}\sqrt{e} \frac{m_\mu}{E_\mu} Z^{1/3}$ and $\rho_{max} = (1 - \frac{6m_\mu^2}{E_\mu^2(1-\nu)}) \sqrt{1 - \frac{4m_e}{E_\mu \nu}}$.

As one can see in Figure 4.1 the energy loss due to pair production is also in a first approximation proportional to the muon energy, *i.e.* $b_p(E_\mu)$ is only weakly dependent on the energy.

4.2.4 Photonuclear Interactions (Deep Inelastic Scattering with Nuclei)

At high muon energy the process of deep inelastic scattering in the lowest order of Quantum Electrodynamical calculation can be described as an exchange of virtual photons. In this case the muon couples directly to the nucleons in the nucleus *via* virtual photons.



At high energy transfer hadronic showers can be produced, where the rest nucleus deexcites by emitting nucleons. In the Born approximation the differential cross section as a function of the four momentum transfer Q^2 and the structure functions W_1 and W_2 is determined by [Rho93]:

$$\left[\frac{d^2\sigma}{dQ^2 d\nu} \right]_{dis} = \frac{\alpha^2}{Q^4} \frac{1}{E^2 - m_\mu^2} \left[4W_1 \left(\frac{Q^2}{2} - m_\mu^2 \right) + 2W_2 \left(2EE' - \frac{Q^2}{2} \right) \right] \quad (4.13)$$

A detailed description of muon deep inelastic scattering can be found in [Bil89]. Also here the energy loss due to deep inelastic scattering is roughly proportional to the muon energy, *i.e.* $dE_\mu/dx = E_\mu b_{dis}(E_\mu)$ with $b_{dis}(E_\mu) \approx \text{constant}$, as one can see in Figure 4.1.

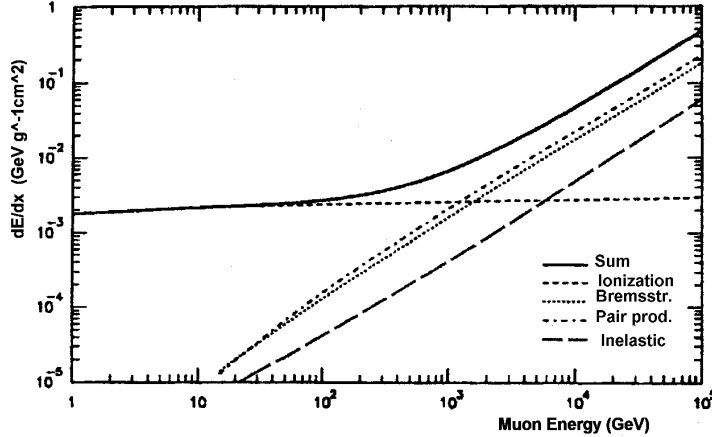


Fig. 4.1 Energy loss dE/dx of high energy muons in standard rock. Contributions of ionization, bremsstrahlung, pair production, inelastic scattering and sum of all interactions are shown [Rho93].

4.3 Muons Underground

Among cosmic rays produced in the atmosphere only muons and neutrinos penetrate to significant depths underground. Muons that pass through the rock overburdens the experimental setup can produce photons, electrons, neutrons, proton, and pions mainly by electromagnetic- and hadronic shower. These shower products together with β 's and γ 's emitted by muon-induced radio nuclides are called cosmogenic background. Only muon-induced neutrons will be discussed further in this work.

The muon total energy loss discussed in the previous subsections can be summarized as the following:

$$\begin{aligned} \left[\frac{dE_\mu}{dx} \right] &= \left[\frac{dE_\mu}{dx} \right]_{Ion} + \left[\frac{dE_\mu}{dx} \right]_{Brems} + \left[\frac{dE_\mu}{dx} \right]_{Pair} + \left[\frac{dE_\mu}{dx} \right]_{dis} \\ &= a_{ion}(E_\mu) + \{b_p(E_\mu) + b_b(E_\mu) + b_{dis}(E_\mu)\} E_\mu \end{aligned} \quad (4.14)$$

Due to their weak dependence on the muon energy the factors b_p , b_b and b_{dis} can be merged into a single factor b . Thus the total muon energy loss consists of an almost energy independent part from ionization, $a = a_{ion}$, and of a part, that is proportional to the muon energy, from the three radiative processes as shown in Eq. (4.15)

$$\left[\frac{dE_\mu}{dx} \right] \approx a + b E_\mu \quad (4.15)$$

These parameters a and b are quite sensitive to the chemical composition of the rock, which must be evaluated for each experimental location. The value of a/b (≈ 500 GeV in standard rock) defines a critical energy below which continuous energy loss due to ionization is more important than radiative energy losses.

The total energy loss of muons in the rock composed of n chemical elements is the sum of the elemental energy losses weighted by their relative abundances p_n :

$$\left[\frac{dE_\mu}{dx} \right]_{total} = \sum_n p_n \left[\frac{dE_\mu}{dx} \right]_n \quad (4.16)$$

In order to compare measurements, that were done to determine the muon energy loss in several experiments with different covering rock, Menon and Ramana Murthy introduced in 1967 the so called *standard rock* with a well defined chemical composition and density. Table 4.1 shows values of parameters a and b for standard rock as a function of muon energy. The second column shows the muon range R for standard rock [Gro01]. The Range is given in km-water-equivalent.

Table 4.1 Average muon range R and energy loss parameters calculated for standard rock.

E_μ GeV	R km w.e.	a MeV g $^{-1}$ cm 2	b_b 10 $^{-6}$ g $^{-1}$ cm 2	b_p 10 $^{-6}$ g $^{-1}$ cm 2	b_{dis} 10 $^{-6}$ g $^{-1}$ cm 2	$\sum b_i$
10	0.05	2.17	0.70	0.70	0.50	1.90
100	0.41	2.44	1.10	1.53	0.41	3.04
1000	2.45	2.68	1.44	2.07	0.41	3.92
10000	6.09	2.93	1.62	2.27	0.46	4.35

Conversion from Gran Sasso rock to Standard rock can be done by using the transformation proposed by [Kot69]. Table 4.2 shows that the parameters of Gran Sasso rock [Cat86] and standard rock are quite close.

Table 4.2 Comparison of parameters of standard rock with Gran Sasso rock.

Rock art	Mass number A	Atomic number Z	Density in g cm $^{-3}$
Standard rock	22	11	2.65
Gran Sasso rock	22.87	11.41	2.71±0.05

4.3.1 Vertical Muon Intensity

In analytical calculations of the muon energy spectrum underground one usually assumes that coefficients a and b are constant and neglects the fluctuation in the energy loss [Lip91]. Because muons are produced as secondary particles from a primary spectrum of high energy cosmic rays, the vertical energy spectrum of muons on the Earth surface follows also the simple potential law from Eq. (4.1) [Lip91]:

$$\frac{dN_\mu}{dE_\mu}(E_\mu, h = 0) = B E_\mu^{-(\gamma+1)} \quad (4.17)$$

From the surface spectrum one can calculate the vertical muon spectrum at a certain depth by using Eq. (4.15):

$$\frac{dN_\mu}{dE_\mu}(E_\mu, h) = B \exp(-\gamma b h) \left\{ E_\mu + \frac{a}{b} [1 - \exp(-bh)] \right\}^{-(\gamma+1)} \quad (4.18)$$

The first exponent describes the fall of the high energy muon flux with depth h , while the expression in the braces determines the shape of the local energy spectrum.

The fluctuation in the energy loss becomes very important for the muon flux deep underground [Lip91], where bremsstrahlung and deep inelastic scattering processes with relative high energy transfer can happen. To in-

clude the influence of fluctuations in Eq. (4.18) Zatsepin *et al.* introduced effective energy loss coefficients ($b_{eff}, b'_{eff} < b$) [Gur76]. In a first approximation one gets the spectrum of the vertical muon flux at depth h underground:

$$\frac{dN_\mu}{dE_\mu}(E_\mu, h) = B \exp(-\gamma b_{eff} h) \left\{ E_\mu + \frac{a}{b'_{eff}} [1 - \exp(-b'_{eff} h)] \right\}^{-(\gamma+1)} \quad (4.19)$$

The mean vertical muon energy can be written as a function of depth h :

$$\bar{E}_\mu^{vert}(h) = \frac{a}{b'_{eff}(\gamma - 1)} [1 - \exp(-b'_{eff} h)] \quad (4.20)$$

It is shown in Figure 4.2.

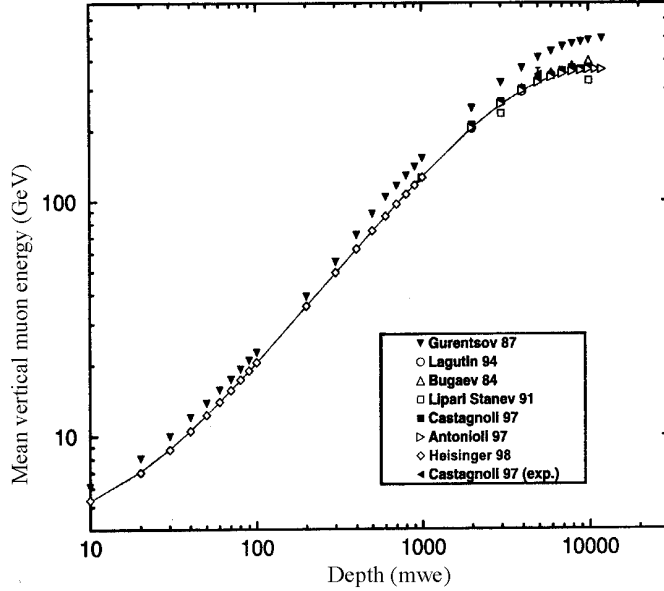


Fig. 4.2 Mean energy of the vertical muon flux $\bar{E}_\mu^{vert}(h)$ according to numerical calculations of [Hei98], Monte Carlo Simulations [Cas95, Cas97, Lag91, Cas97, Ant97] and semi-analytical calculations of [Gur76]. The line is a fit to data of [Hei98](\diamond) and [Ant97](\triangleright).

From a surface spectrum with $\gamma = 2.70$, Castagnoli *et al.* [Cas95] gave the parameters $b_{eff} = 0.381 \text{ (km w.e.)}^{-1}$, $b'_{eff} = 0.374 \text{ (km w.e.)}^{-1}$, and $a/b'_{eff} = 647 \text{ GeV}$ for standard rock in the depth range of 4–10 km w.e.

4.3.2 Local Muon Energy and Intensity at LNGS

Information on muons at Gran Sasso come from two experiments: MACRO (Monopole, Astrophysics, and Cosmic Ray Observatory), that was located in hall B, and LVD (Large Volume Detector), that is located in hall A. MACRO measured muons at slant depths of $3000 - 7000 \text{ hg/cm}^2$. The measured muon flux in the slant depth region considered corresponds to the muon spectrum at the surface in the energy range of 1-20 TeV or 2-200 TeV in the all-nucleon primary flux. The experimental data were fitted with Eq. (4.19), with the parameters $h = 4 \text{ km}$ w.e., $b_{\text{eff}} = b'_{\text{eff}} = 0.383 \text{ (km w.e.)}^{-1}$, $a/b'_{\text{eff}} = 618 \text{ GeV}$ and $\gamma = 2.70$. The average muon energy in the energy range $0.1 < E < 1 \text{ TeV}$ is $225 \pm 3 \text{ (stat.)} \pm 4 \text{ (syst.) GeV}$. The fraction of energy above 1 TeV is about 6% and average of all muon energy is found to be $320 \pm 4 \text{ (stat.)} \pm 11 \text{ (syst.) GeV}$.

In order to compare the MACRO results with those of other experiments, a conversion of the data to standard rock slant depth was done and the vertical muon intensity was calculated. In the range of $3200-7000 \text{ hg cm}^{-2}$ the data are well fitted by the three-parameter empirical formula:

$$I_\mu(h) = A \left(\frac{h_0}{h} \right)^\alpha e^{-\frac{h}{h_0}} \quad (4.21)$$

with $A = (1.96 \pm 0.03) \times 10^{-6} \text{ cm}^{-2} \text{ s}^{-1} \text{ sr}^{-1}$, $\alpha = 1.1 \pm 0.01$, and $h_0 = (972 \pm 3) \text{ hg cm}^{-2}$. Using the Frejus function [Ber89]:

$$I_\mu(h) = B \left(\frac{h_1}{h} \right)^2 e^{-\frac{h}{h_1}} \quad (4.22)$$

the data are fitted with $B = (1.81 \pm 0.06) \times 10^{-6} \text{ cm}^{-2} \text{ s}^{-1} \text{ sr}^{-1}$ and $h_1 = (1231 \pm 1) \text{ hg cm}^{-2}$.

LVD has measured the muon intensity at slant depths of standard rock from about 3000 hg cm^{-2} to about 20000 hg cm^{-2} , hence covers also the region where the dominant source of muons is the interaction of atmospheric neutrinos with the rock surrounding the experiment. The depths correspond to muon energies at the sea level from 1.5 TeV to 40 TeV or from 10 – 400 TeV of the energies of primaries. Due to the unique topology of the Gran Sasso laboratory the muons beyond about 14000 hg cm^{-2} of standard rock are at zenith angles near 90° . Therefore, LVD is the first experiment reported measurement at zenith angles near 90° and for slant depths between 14000 and 20000 hg cm^{-2} . The plot of the data (see Figure 4.3) shows an exponential shape up to a slant depth of about 14000 hg cm^{-2} and is roughly constant beyond that point. The Frejus function plus a constant term was used to fit the data [Agl95]:

$$I_\mu(h) = B \left(\frac{h_1}{h} \right)^2 e^{-\frac{h}{h_1}} + K_0 \quad (4.23)$$

The best fit for these three parameters are: $B = (1.77 \pm 0.02) \times 10^{-6} \text{ cm}^{-2} \text{ s}^{-1} \text{ sr}^{-1}$, $h_1 = (1211 \pm 3) \text{ hg cm}^{-2}$ and $K_0 = (2.98 \pm 1.15) \times 10^{-13} \text{ cms}^{-1} \text{ sr}^{-1}$, in good agreement with MACRO.

Figure 4.3 shows the vertical muon intensity as a function of depth h in standard rock. Data from several experiments are plotted together.

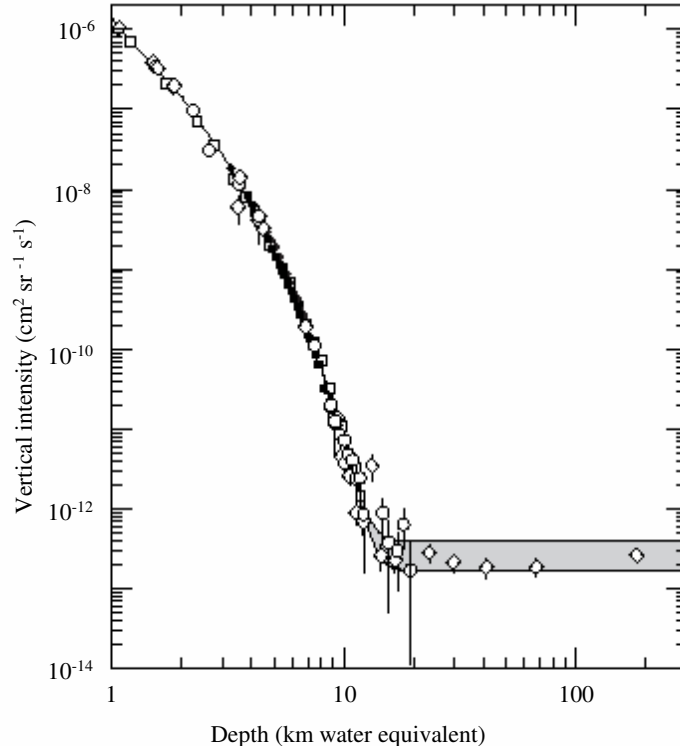


Fig. 4.3 Vertical muon intensity *vs.* depth in standard rock. The experimental data are from: \diamond : the compilation of Crouch [Cro87], \square : Baksan [And87], \circ : LVD [Agl99], \bullet : MACRO [Amb95], \blacksquare : Frejus [Ber89]. The shaded area at large depths represents neutrino-induced muons with energies above 2 GeV. The upper line is for horizontal neutrino-induced muons, the lower one for vertically upward going muons.

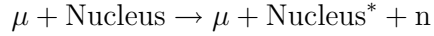
4.4 Muon-induced Neutrons Underground

High energy muons, that typically have a mean energy of 300-400 GeV at a depth of 3000-5000 m w.e., may produce neutrons with energies up to 100 MeV. There are four main processes of neutron production by muons underground:

- (i) μ^- capture by a nucleus followed by neutron emission. The μ^- capture cross section depends very sensitively on the μ^- kinetic energy

and falls off sharply for kinetic energies greater than the e^- binding energy. This process is important at depths less than 300 m w.e. and is therefore negligible for the determination of the neutron background for experiments at large depths.

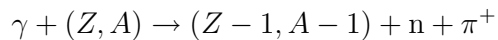
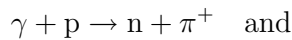
- (ii) neutron photo-production in μ inelastic scattering on nuclei. In deep inelastic scattering μ interacts with a nucleus *via* a virtual photon producing a nuclear disintegration. This process is usually called “direct muon spallation”:



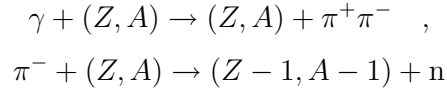
- (iii) neutron production by hadrons in the muon-generated nuclear showers. In this case neutrons are generated in pion-nucleus and nucleon-nucleus interactions.
- (iv) neutron production by γ 's in the muon-generated electromagnetic showers. Here neutrons are produced mainly in photonuclear interactions.

In an inelastic scattering of a muon with a high energy transfer, multiple production of hadrons ($\pi^\pm, \pi^0, K^\pm, K^0, n$ and p) occurs, and a nuclear shower develops. According to their energy, hadrons in a nuclear shower can be divided into three groups: shower hadrons ($\beta > 0.7$), cascade hadrons ($\beta = 0.2 - 0.7$) and evaporative nucleons ($\beta < 0.2$), where $\beta = v/c$. Shower pions π^\pm produce new generations of particles until no particles with $\beta > 0.7$ are left. The cascade hadrons in collisions with nuclei produce cascade particles with lower energies and evaporative nucleons. Cascade neutrons can multiply further in nuclear reactions, while cascade protons lose their energy rapidly by ionization. An additional mechanism of neutron production is the capture of a slow π^- by a nucleus. Slow π^+ 's decay through $\pi^+ \rightarrow \mu^+ \rightarrow e^+$ [Kha95].

In electromagnetic showers, the main process that produces neutrons and pions is photo-production on nuclei. This process is also known as real photonuclear disintegration, in contrast to virtual photo-production in the direct muon spallation process. In this process, the major contribution comes from (γ, n) reactions. In addition, it is also necessary to take multiple photo-production reactions (γ, xn) into account. Due to the fact that the spectrum of shower photons falls with energy as dE_γ/dE_γ^2 [Bel48], neutrons in electromagnetic showers are generated mainly by low energy photons. At higher γ energies, there are two channels for neutron production [Kha95]: first, due to inelastic charge exchange reactions



and second, in two step reactions such as



It has been shown [Rya66] that the intensity of μ -induced neutron production falls with depth slower than the muon intensity. Due to the cascade process the number of neutrons produced per muon increases with the average energy of the muon $\langle E_\mu \rangle$ at corresponding depth h [Zat66a, Kha95]:

$$N_n(h) \propto \langle E_\mu(h) \rangle^{0.75} \quad (4.24)$$

Several measurements have been done to determine the rate of neutron produced by muons underground. Many experiments reported their results as a function of the detector's depth underground, but the proper physical parameter is actually the mean muon energy at the detector site. The conversion between depth and mean muon energy is not entirely trivial, because the mean energy depends on the geometry of the rock overburden, especially in the case of deep sites. For consistency, experimental results on neutron production in liquid scintillator from the depth of 20 m w.e. up to 5200 m w.e. underground are shown in Figure 4.4 as a function of the mean muon energy [Wan01].

Formula (4.24) is in agreement with most measurements except the recent one by the LVD collaboration [Agl99]. The result of LVD, $(1.5 \pm 0.4) \cdot 10^{-4} \mu\text{g cm}^{-2}$, is 3.5 times lower than that obtained by the LSD detector at larger depth. The difference can not be easily explained by large systematic uncertainty and the difference of the depths of the detector sites. Simulations with Fluka Monte Carlo code [Wan01] are indicated with stars in Figure 4.4 and fitted with the following power law:

$$N_n(h) = 4.14 \langle E_\mu(h) \rangle^{0.74} \cdot 10^{-6} \quad \text{neutrons}/(\mu\text{g.cm}^{-2}) \quad (4.25)$$

where energy is in GeV. This relation is consistent with $E_\mu^{0.75}$ law.

4.5 High Energy Neutrons Induced by Muons in the LNGS Rock (Demetyev's Spectrum)

4.5.1 *Spectrum of Neutrons Entering the Experimental Hall*

Muons interacting with nuclei of the rock initiate hadron cascades, consisting of pions, protons, and neutrons. Demetyev *et al.* [Dem99] performed simulations of production and transport of hadrons generated in nuclear cascades initiated by muons in the Gran Sasso rock. The code they used was the universal hadron transport code SHIELD [Sob70,

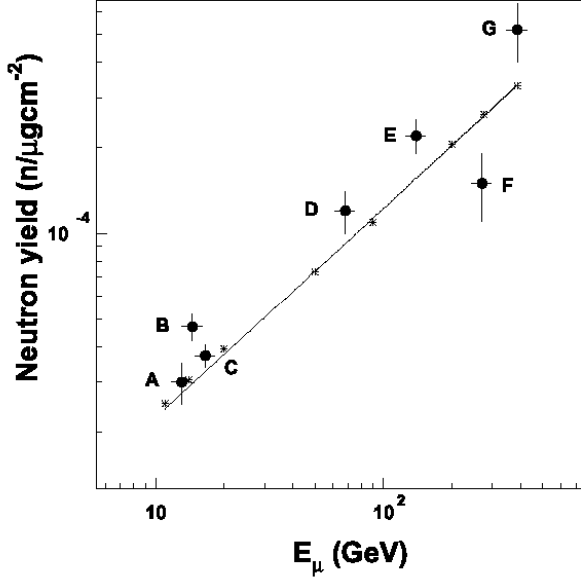


Fig. 4.4 Neutron production rate as a function of the mean muon energy. The abscissa corresponds to the mean muon energy at the experiment's depths: (A) 20 m w.e. [Boe00, Her95], (B) 25 m w.e. [Bez73], (C) 32 m w.e. [Her95] by the Palo Verde experiment, (D) 316 m w.e. [Bez73], (E) 750 m w.e. [Eni87], (F) 3650 m w.e. by the LVD experiment at Gran Sasso [Agl99], and (G) 5200 m w.e. by the LSD experiment at Mount Blanc [Agl89].

Dem94]. Coordinates of the point of inelastic muon-nucleus interactions were supposed to be uniformly distributed inside the rock volume. The direction of the primary muon was sampled according to the measured angular distribution at the depth of LVD [Lvd94]. The muon spectrum at Gran Sasso was taken as

$$\frac{dN}{dE} = \text{Const} \times [E + (\gamma - 1) \times \bar{E}]^{-(\gamma+1)} \quad (4.26)$$

where $\gamma = 2.70$ is the exponent of the atmospheric muon spectrum, and $\bar{E} = 280$ GeV is the average muon energy at the given depth. The fraction of energy transferred by a muon to hadron cascade was calculated according to Bezrukov and Bugaev [Bez81]. The absolute density of inelastic muon-nucleus interaction, 9.45×10^{-6} (1/g year), was used further for normalization of the hadron spectra.

The spectra of hadrons entering the Gran Sasso hall are shown in Figure 4.5. The integral flux of neutrons is only about $200 \text{ n/m}^2/\text{y}$ where the bulk comes from the contribution of neutrons with energies below 1 GeV. Angular distributions of the particles were calculated for the roof, walls, and floor of the hall separately and are shown in Figure 4.6.

Compared to the measured neutron flux in the laboratory [Bel89] above 5 MeV ($0.051 \text{ n/cm}^2/\text{s} = 16094 \text{ n/m}^2/\text{y}$), the flux of muon-induced neutrons in the rock between 6-25 MeV ($71 \text{ n/m}^2/\text{y}$) is negligible ($\sim 0.4\%$). The bulk of the neutron flux in the laboratory is indeed neutrons from fission and (α, n) reactions. However, the energy spectrum of these muon-induced neutrons is hard, extending to the GeV range. The fast neutrons can propagate far, reach the detector and produce additional neutrons in the shielding materials.

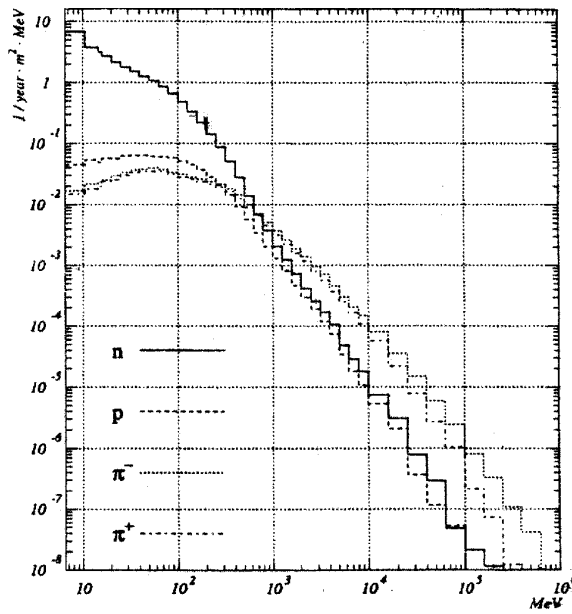


Fig. 4.5 Energy spectrum of muon-induced hadrons in the rock entering the Gran Sasso hall [Dem99].

4.5.2 Count Rates Obtained with the Dementyev's Spectrum

In spite of the small flux, high energy neutrons from muon cascades in the rock can enter the shield of the experimental setup (especially lead) and undergo spallation reactions (like (n, xn)) and produce more neutrons that are less energetic, but more probable to induce recoils in the energy range interesting for the experiment. Just to give some examples, neutrons production rates by spallation of high energy neutrons in lead have been simulated in this work with the FLUKA simulation code [Fas00] and are shown in Table 4.3. It is seen that the production rate increase with energy.

A study has been done in this work to determine the contribution of

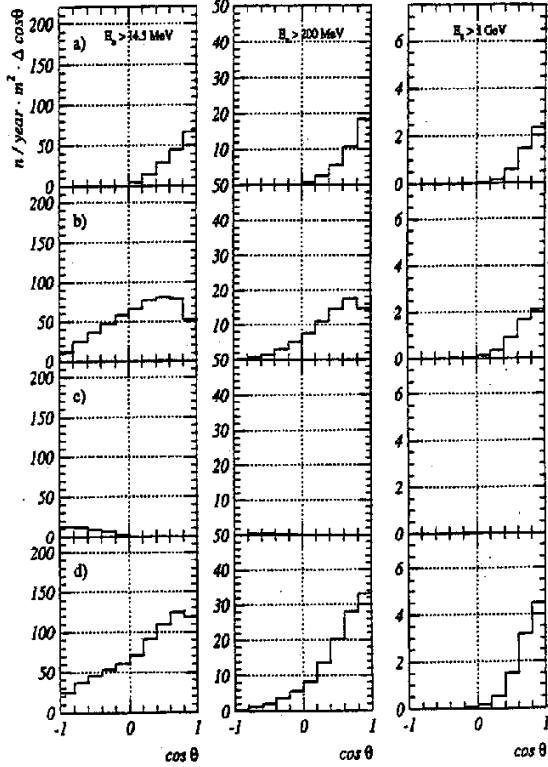


Fig. 4.6 Angular distribution of neutrons entering the experimental hall from: a) roof, b) walls, c) floor and d) sum, for three energy threshold: 14.5, 200 and 1000 MeV [Dem99].

Table 4.3 Neutron production rates by spallation of high energy neutrons in lead.

Neutron Energy (MeV)	Neutron production rate (1/n/(g/cm ²))
50	4.78×10^{-3}
100	8.89×10^{-3}
500	3.30×10^{-2}
1000	5.75×10^{-2}

neutrons induced by muons in the rock, as shown by Dementyev *et al.* [Dem99], to the rate of neutron background in CRESST. It is not clearly stated in the work of Dementyev *et al.* [Dem99] whether the neutron energy spectrum coming into the laboratory hall (see Figure 4.5) is the spectrum after scattering inside the laboratory (neutrons are let to scatter inside the

laboratory and counted more than once) or without scattering inside the laboratory (neutrons are stopped while entering the hall for the first time). Therefore, to get the recoil spectrum and count rate in the detector (CaWO_4 crystal) with Dementyev's spectrum, two different simulation series were performed. MCNPX and MCNP4B were used for these simulations.

In the first case, neutrons following Dementyev's energy spectrum (Figure 4.5) were generated at the outer surface of the experimental set up with an angular distribution sampled isotropically in 2π . The flux of neutrons at the six sides of the setup were taken according to the flux entering the hall from the roof, the floor and the walls (see Figure 4.6, left). The simulations were done for the simple geometry (Pb/Cu shields without neutron moderator), the simple setup with 50 cm Polyethylene, and the more realistic setup with 30 cm Polyethylene at the bottom and 60 cm elsewhere. Table 4.4 shows the count rate at 15-25 keV for those different geometries.

Table 4.4 Count rates at 15-25 keV in CaWO_4 induced by high energy neutrons (Dementyev's spectrum) sampled at the outer surface of the Pb shield.

Thickness of polyethylene (cm)	Count Rate (15-25 keV) (cts/kg/day)
No PE	1.89×10^{-3}
50	8.94×10^{-4}
Realistic setup (PE:30 cm bottom, 60 cm elsewhere)	6.82×10^{-4}

If one compares the results with those from the simulations of low energy neutron with the measured spectrum [Bel89] (see Table 3.16 in chapter 3), it is clearly seen that for the setup with 50 cm polyethylene, the count rates of high energy neutrons from the rock are higher than those of low energy neutrons, which is 9.96×10^{-5} cts/kg/day. This is because high energy neutrons penetrate the moderator without loosing much energy. Moreover they can even undergo spallation in the Pb/Cu shields and produce additional neutrons with lower energies, that eventually give rise to the count rate in the detector. The count rate for the realistic setup is also higher than that of low energy neutrons from the rock, which is 8.35×10^{-5} cts/kg/day (see discussion in subsection 3.4.2). Figure 4.7 shows the recoil spectra for the setup with 50 cm polyethylene.

In the second series of simulations, neutrons following Dementyev's energy spectrum (Figure 4.5) and the angular distribution for neutron energy above 14.5 MeV (see Figure 4.6) were sampled at the surface of the laboratory hall. The experimental setup was placed on the floor at the center of the experimental hall (which was taken as 20 m wide, 100 m long, and

20 m high). Behind the surfaces of the experimental hall was a layer of 2 m rock. Neutrons were allowed to scatter inside the laboratory. Because of the position of the setup inside the hall and the angular distribution of the neutrons coming from the rock, many neutrons did not go directly to the setup or even reach it at all. The consequence is that the neutron spectrum was softened when reaching the outer surface of the experimental setup. Due to scattering a large number of neutrons was slowed down to below 6 MeV (see Figure 4.8)

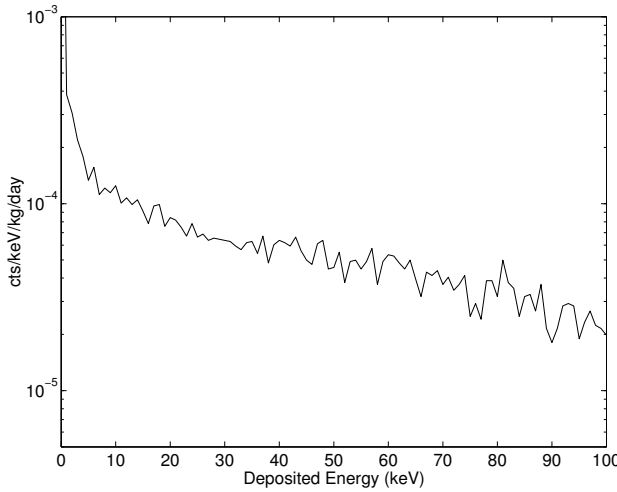


Fig. 4.7 Recoil spectrum induced by high energy neutrons [Dem99] started at the surface of the Pb shield. Geometry: simple setup with 50 cm polyethylene.

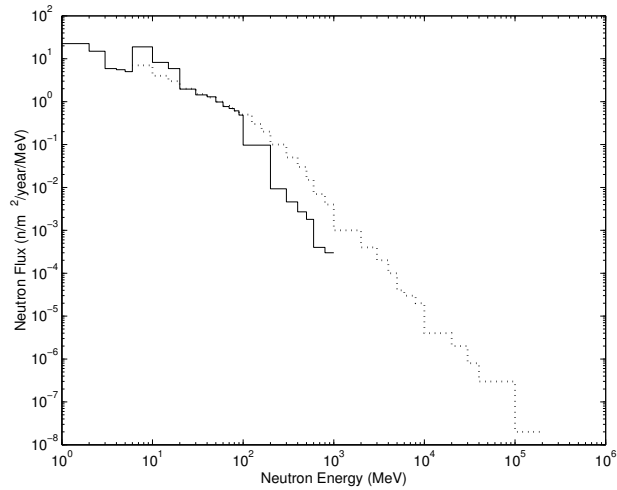


Fig. 4.8 Spectrum of neutrons when entering the hall (dotted line) [Dem99] and at the outer surface of the experimental setup (after scattered inside the hall (solid line)).

The count rates at 15-25keV for the Pb/Cu setup without neutron moderator and for the setup with 50 cm polyethylene are shown in Table 4.5. These count rates are lower than the corresponding rates obtained in the first case (see Table 4.4). This is because neutrons in this case are less energetic than those in the first case, and therefore induce less spallation in the lead shield. Besides, neutrons with energy less than 6 MeV (which are absent in the first case but numerous in the second case) would not survive the moderator. The count rate for the setup with 50 cm polyethylene is slightly lower than the count rate of low energy neutron obtained from the measured spectrum [Bel89] but almost five times higher than that of low energy neutron obtained from the calculated spectrum with dry concrete, both with 50 cm polyethylene shield. The recoil spectra for the two cases are shown in Figure 4.9. However, it will be shown in the next section, that the first case of simulations using Dementyev's spectrum is more realistic than the second one.

Table 4.5 Count rates at 15-25 keV in CaWO₄ induced by high energy neutrons (Dementyev's spectrum) sampled at the hall surface.

Thickness of polyethylene (cm)	Count Rate (15-25 keV) (cts/kg/day)
No PE	8.1×10^{-4}
50	7.4×10^{-5}

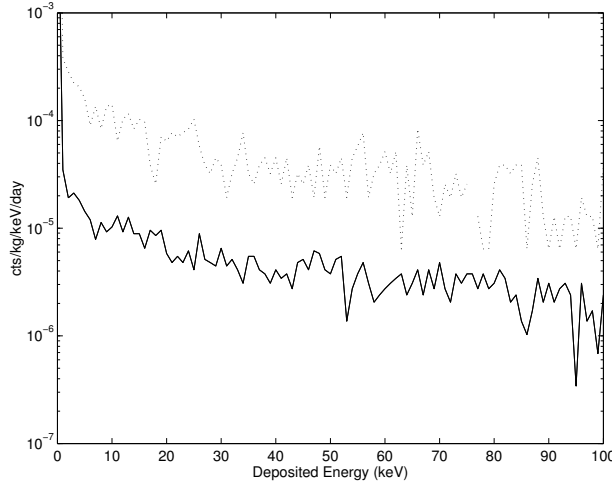


Fig. 4.9 Recoil spectra induced by high energy neutrons [Dem99] started at the surfaces of the laboratory hall. Dotted line: Pb/Cu shields without neutron moderator, solid line: Pb/Cu shield with 50 cm of polyethylene.

Comparing count rates from simulations of high energy neutrons (Dementyev's spectrum) with those from simulations of low energy neutron from the rock (concrete) activity, one can conclude that the use of thick polyethylene is good to suppress the contribution of low energy neutrons, but then the neutron background will be dominated by high energy neutrons from the rock. Since this issue is crucial if higher and higher sensitivity is aimed for with CRESST, high energy neutrons should be studied carefully. It is worth therefore, to check Dementyev's spectrum and also the assumptions used in the two cases of simulations that have been performed for high energy neutrons from the rock.

Another source of background neutrons is the interaction of muons with the experimental setup. Neutrons produced in the cascades generated by muons in the setup would increase the count rate of neutron background. It would be ideal, therefore, to perform full simulations that follow muons and their cascade products down to the detector level and eventually get neutron count rates at the detector.

4.6 Full Simulations of Muon-induced Neutrons for CRESST

The CRESST setup is located in hall A of the Gran Sasso underground laboratory, excavated under about 1300 m of rock (3600 m w.e.), which reduces the muon flux by a factor of $\sim 10^6$ compared to the surface flux. Nevertheless, about $1 \mu/\text{hm}^2$ [Cri97, DeM92] reaches the setup. As mentioned before, muons can produce neutrons in the rock (and concrete) and in the materials used in the setup and shielding. To determine the background induced by neutrons from muons in CRESST, a study based on Monte Carlo simulation has been performed in this work. This section will cover the description of the codes used to simulate muon-induced neutrons, how muon flux and energy spectrum were obtained, neutron production rates by muons in materials relevant for CRESST, the neutron energy spectrum entering the hall and finally the neutron count rate at CRESST detector.

4.6.1 Monte Carlo Codes Used for the Simulations

After an intensive comparative study and correspondences with authors and users of several Monte Carlo codes, it is concluded that no single Monte Carlo code is capable to do the whole task, from transporting muons, simulating neutron production from muons, and tracking neutrons down to nuclear recoils in the detector. Muon nuclear interaction, for example, is not yet implemented in MCNPX. The code, therefore, can not be used to simulate neutron production. GEANT 3.21 underestimates photo nuclear production. The KARMEN Group introduced a correction in the cross section, and was able to get an agreement of experimental data with simu-

lations of muons with energies up to 100 GeV. The same correction is being used and tested in simulations for higher muon energy for EDELWEISS.

Recently, a new MC code GEANT 4 has been released, but is not yet fully tested for neutron production and for low energy neutrons. Some errors in the high energy electro-nuclear interactions have been reported [Wel02] and are being fixed. In the simulations of the neutron scattering experiment in Munich an error in the inelastic scattering of neutrons below 20 MeV was reported [Wal02]. It is not yet clear if this error happens also with higher energy neutrons.

Currently the most complete code to describe both hadronic and electromagnetic interactions up to 20 TeV is FLUKA [Fas00]. Nevertheless, the use of FLUKA for the purpose of this work is not free of problems. FLUKA, in fact, does not treat individual nuclear recoils, but it treats low energy ($< 20\text{MeV}$) neutron interactions in an average way. Energy deposition is calculated using kerma factors, *i.e.* by summing over all possible reactions. The energy is conserved on average, but not necessarily in a single reaction. Therefore, in this work FLUKA was used for simulations of neutron production from muons and for transport up to the experimental cavity in the CREST setup. The recoil spectrum in the detector is obtained by employing MCNP, which has also been used to get the recoil spectrum of low energy neutrons.

4.6.2 Muon Flux and Energy Spectrum

There are two important quantities for calculating the production rate of neutrons from muons, namely the muon flux and the muon energy spectrum. The muon flux is needed for absolute normalization, while the muon energy spectrum is important due to the increase of neutron production with muon energy. Unlike the muon flux underground that can be measured, the muon energy spectrum is hard to determine experimentally. It is usually obtained from simulations.

To calculate differential and integral muon intensities at the depth of the Gran Sasso laboratory a special code called SIAM [Kud03a] was used. In this code the differential muon intensity underground was determined by using the following equation:

$$I_\mu(E_\mu, X, \cos \theta) = \int_0^\infty P(E_\mu, X, E_{\mu 0}) \frac{dI_{\mu 0}(E_\mu, \cos \theta^*)}{dE_{\mu 0}} dE_{\mu 0} \quad (4.27)$$

where $\frac{dI_{\mu 0}(E_\mu, \cos \theta^*)}{dE_{\mu 0}}$ is the muon intensity at sea level at the zenith angle θ^* :

$$\frac{dI_{\mu 0}(E_\mu, \cos \theta^*)}{dE_{\mu 0}} = A \frac{0.14 E_\mu^{-\gamma}}{\text{cm}^2 \text{s sr GeV}^X} \left\{ \frac{1}{1 + \frac{1.1 E_{\mu 0} \cos \theta^*}{115 \text{GeV}}} + \frac{0.054}{1 + \frac{1.1 E_{\mu 0} \cos \theta^*}{850 \text{GeV}}} + R_c \right\} \quad (4.28)$$

The zenith angle at the Earth's surface, θ^* , was calculated from the zenith angle underground, θ , taking into account the curvature of the Earth. R_c denotes the ratio of prompt muons to pions. The parameters in Eq. (4.28) were taken either according to Gaisser's parameterization [Gai90] ($A=1, \gamma=2.70$) which is modified for large zenith angles and prompt muon flux [Agl98], or following the best fit to the depth-vertical μ intensity relation measured by the LVD experiment [Agl98]. LVD reported the normalization constant $A = 1.84 \pm 0.31$, $\gamma = 2.77 \pm 0.02$ and the upper limit $R_c \leq 2 \times 10^{-3}$ (95% C.L.) [Agl99b]. $P(E_\mu, X, E_{\mu 0})$ is the probability for a muon with energy $E_{\mu 0}$ at the surface to have the energy E_μ at depth X [Kud03b]. $P(E_\mu, X, E_{\mu 0})$ was obtained by propagating muons with various energies at the Earth's surface using MUSIC (**Muon Simulation Code**) [Ant99].

In this work the ratio of prompt muons to pions was chosen to be 10^{-4} , well below the upper limit given by LVD [Agl99b]. To calculate the integral muon intensity, an integration of Eq. (4.27) over dE_μ was carried out. An additional integration over $\cos \theta$ gives the global intensity for a spherical detector.

The absolute muon intensity underground depends in fact on the surface relief. Gran Sasso has a very complex mountain profile, that make it difficult to predict the muon flux without precise information on the slant depth distribution. In this work a flat surface was assumed as approximation. In the near future, a further study is planned, taking the detail mountain profile of Gran Sasso into account. There might not be a big difference in the neutron production. The simulation results will after all be normalized to the muon flux measured in Gran Sasso ($1\mu/\text{h}/\text{m}^2$). The difference may be important for simulations of the muon veto.

4.6.3 *Simulations of Muon-induced Neutrons*

As mentioned before, neutron production by muons in this work has been simulated with FLUKA [Fas00]. The models of photo-production and hadronic interaction used in FLUKA are described in [Fas00, Wan01].

A commonly used approximation (see for example [Kha95, Agl89, Wan01] and references therein) to determine neutron production by muons at a certain depth is the assumption that neutrons are produced by muons with fixed energy which corresponds to the mean energy at this depth. Therefore, besides using the two muon energy spectra underground (the ones obtained using Gaisser's formula and the LVD best fit), simulations of neutron production were also performed for mono energetic muons of 270 GeV (the mean energy at the depth of the Gran Sasso laboratory).

In this work, the neutron production was simulated for materials relevant for CRESST, *i.e.* Gran Sasso rock, Gran Sasso concrete, lead, copper, and polyethylene. The simulations of neutron production were done by

shooting mono directional muons at a wide slab of medium (perpendicular to the muon direction). Since cascades need some depth to develop and to produce neutrons, the thickness of medium was chosen large enough (of the order of 4000-5000 g/cm²). However, the use of a large thickness can reduce the muon energy compared to the initial value due to the interaction with matter. Therefore, careful checks were done to ensure that the neutron flux in the simulations did not decrease with the thickness of the medium crossed by the muons. Technically, the medium thickness was divided into several bins. So it can be expected that neutron fluxes in the first bins (where cascades have not yet developed) and the last bins (where the muon energy is decreased) are smaller than in the middle bins.

An appropriate correction of the order of a few percent was then applied to get reasonable neutron production rates. In each bin neutrons can be scattered back to the previous bin. In FLUKA a scattered neutron is also counted as a secondary neutrons (with different energy). These neutrons are called “stars” in FLUKA. To avoid double counting, the number of stars produced by neutrons was subtracted from the total number of neutrons.

To study the contribution of different mechanisms of neutron production, three different simulations were performed for each material, *i.e.*: neutron production from muon spallation only, from muon spallation and hadronic cascades, and from all processes including electromagnetic cascades. To simulate neutron production from muon spallation only, the electromagnetic interaction was switched off and secondaries produced in hadronic cascades (n , π , p , *etc.*) were discarded (produced but not transported). To determine neutron production from muon spallation and hadronic cascades, the electromagnetic interaction was again switched off but particles produced in the hadronic interaction were not discarded, whereas to get neutron production by all interactions, the electromagnetic interaction was switched on in addition.

To get a better statistic each simulation was repeated several times. The results for the simulations with a muon energy of 270 GeV are shown in Table 4.6. Neutron productions from hadronic cascades were obtained by subtracting the rates of muon spallation only from the rates of hadronic production and muon spallation. The rate of neutron productions from electromagnetic cascades were calculated by subtracting the rates from μ spallation and hadronic cascades from the neutron production from all interactions.

It is clearly seen that neutron production at this energy is dominated by secondary processes (hadronic and electromagnetic showers). It can also be seen that neutron production increases with the atomic weight A of the target. In Figure 4.10 neutron production rates, N_n , from 270 GeV muons as a function of the atomic weight A of materials relevant for CRESST are

Table 4.6 Neutron production rates from 270 GeV muons in several materials.

Material	Neutron production rate (10^{-5} n/ μ /(g/cm 2))			
	μ -spallation	Hadronic shower	E.M. shower	Total
Lead	11.05	212.21	200.91	424.16
Copper	4.75	80.13	47.06	131.94
LNGS rock	2.02	27.89	7.34	37.45
LNGS concrete	2.07	27.05	7.71	36.82
Polyethylene	1.51	17.75	6.86	26.11

shown. A simple parameterization by a linear function is given by

$$N_n = 2.06 \times 10^{-5} A \text{ n/muon/g cm}^{-2} \quad (4.29)$$

The production rates in rock and concrete are about the same due to their almost similar atomic weights.

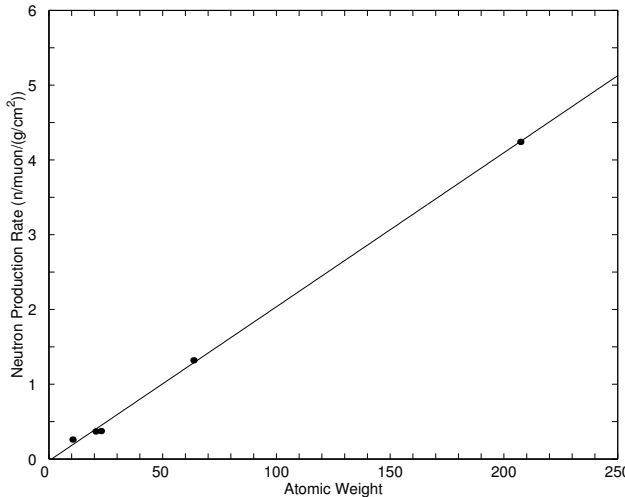


Fig. 4.10 Neutron production from 270 GeV muons as a function of the atomic weight A of materials relevant for CRESST: lead ($A = 207.20$), copper ($A = 63.55$), Gran Sasso rock ($A = 22.87$), Gran Sasso concrete ($A = 20.50$) and polyethylene ($A = 10.40$). A simple parameterization by a linear function is given by the solid line.

In Table 4.7 neutron production rates for different interactions are given for the muon spectrum underground obtained with the LVD formula, while neutron production rates for the muon spectrum underground obtained with Gaisser's parameterization are shown in Table 4.8. The rates obtained with these two μ spectra underground are in agreement with each other and also with the results from 270 GeV muons.

There are some old measurements on the neutron production rate by

Table 4.7 Neutron production rate from muons with the LVD best fit spectrum in several materials.

Material	Neutron production rate (10^{-5} n/ μ /(g/cm 2))			
	μ -spallation	Hadronic shower	E.m. shower	Total
Lead	10.13	239.45	178.68	428.26
Copper	4.22	74.95	41.04	120.20
LNGS rock	1.79	26.42	7.37	35.59
LNGS concrete	1.86	25.40	5.70	32.96
Polyethylene	1.23	16.32	6.27	23.82

Table 4.8 Neutron production rate from muons with Gaisser's parametrization in several materials.

Material	Neutron production rate (10^{-5} n/ μ /(g/cm 2))			
	μ -spallation	Hadronic shower	E.m. shower	Total
Lead	10.46	231.76	183.65	425.87
Copper	4.29	80.30	35.71	120.30
LNGS rock	1.83	27.19	6.65	35.67
LNGS concrete	1.84	25.78	5.86	33.48
Polyethylene	1.24	18.46	6.21	25.91

muons that can be used as a comparison for the result in this work. Gorshkov [Gor73] measured neutron production by muons for several elements including lead at 1000 m w.e. In the lead he found a neutron production rate of 6.0×10^{-9} neutrons/g/s. Given the muon flux at 1000 m w.e. ($8 \times 10^5 \mu/m^2/y$), the result can be rewritten as 2.37×10^{-3} neutrons/ μ /(g/cm 2). The mean energy at this depth is 150 GeV. Using the law that holds for scintillator, *i.e.* that neutron production rate goes like $E_\mu^{0.75}$, would give a neutron production rate at 270 GeV (Gran Sasso mean muon energy) 3.68×10^{-3} neutrons/ μ /(g/cm 2), which is in quite good agreement with the simulation in this work.

Bergamosco [Ber73] performed his experiment in Mont Blanc (4300 m w.e. or 5200 m w.e according to the LSD experiment [Agl89]) and reported a neutron production of 6.0×10^{-4} neutrons/g/y. Given the muon flux at Mont Blanc ($500 \mu/m^2/y$), this means the neutron production in lead at this depth is 1.2×10^{-2} neutrons/ μ /(g/cm 2). If the mean muon energy at Mont Blanc is assumed to be 385 GeV as reported by LSD [Agl89] the $E_\mu^{0.75}$ law would give neutron production rate in lead at Mont Blanc as 4.80×10^{-3} neutrons/(g/cm 2), which is almost three times lower than Bergamosco's result. In fact, Bergamosco has reported a product of multiplication and cross section, $\bar{m}\sigma$, which is about three times higher than the theoretical

prediction and extrapolation from several experiments [Ber73].

Recently, measurements to determine the neutron production rate in lead, copper and carbon were performed in the NA55 experiment at CERN with a 190 GeV muon beam [Cha02]. The use of thin target allowed the measurements of neutron production in the first muon interaction only (without taking neutrons produced in cascades into account) [Cha02]. Results of the measurements for lead and copper are shown in Table 4.9 for three different solid angles. The relevant quantity in this work to compare with these measurements is neutron production rate from muon spallation only. However, because neutron production was reported at several scattering angles in the NA55 experiment, a direct comparison with results in this work is difficult.

Table 4.9 Measured neutron production in the CERN NA55 experiment.

Solid angle	Target	$\text{neut}/\mu.\text{sr}.\text{g}.\text{cm}^{-2}$
$45^0 \pm 1$	Cu	$(1.90 \pm 0.38) \times 10^{-5}$
$90^0 \pm 1$		$(0.76 \pm 0.14) \times 10^{-5}$
$135^0 \pm 1$		$(0.79 \pm 0.14) \times 10^{-5}$
$45^0 \pm 1$	Pb	$(3.93 \pm 0.87) \times 10^{-5}$
$90^0 \pm 1$		$(3.39 \pm 0.69) \times 10^{-5}$
$135^0 \pm 1$		$(1.09 \pm 0.21) \times 10^{-5}$

4.6.4 *Energy Spectrum of Neutrons Entering the LNGS Hall*

To determine the energy spectrum of neutrons coming from the rock into the laboratory hall, the muon spectrum from the LVD best fit was used (see previous discussion on the muon spectrum at Gran Sasso). It is clear that the number of neutrons entering the hall should depend on the thickness of the rock used in the simulations. A very large thickness needs too large computing time, whereas a too small thickness will underestimate the particle yield. It was found in the simulation of neutron production in Gran Sasso rock using the muon spectrum from the LVD best fit, that cascades were well developed and that the equilibrium between neutron and muon flux was reached after muons had crossed about 6-7 meter of Gran Sasso rock.

An additional information came from the results from Monte Carlo simulations performed by Dementyev [Dem99]. He found that the typical depth of Gran Sasso rock for hadrons with energies above 200 MeV is 90 cm, which means that 96% of neutron flux coming into the hall are produced at the depth of about 3 meter behind the rock surface.

In this work muons were generated at the surfaces of a cube of rock with a size of $20\text{ m} \times 20\text{ m} \times 20\text{ m}$. Inside the rock cube, the experimental hall was taken to be the size of $6 \times 6 \times 5\text{ m}^3$. The top of the hall was placed 10 m below the top of the rock cube (see Figure 4.11). This should be an optimal depth to allow the cascades to develop and to let neutrons be produced in the last 3-4 meter of rock overburden the hall enter the hall. The size of the experimental hall used in these simulations, which is smaller than the real hall at the Gran Sasso laboratory, was chosen to save computing time. But some test simulations have been done to ensure that the results do not change significantly if a larger size is used. To sample muon energy and angular distribution the code MUSUN (Muon Simulation Underground) [Kud03c] was used. This code and the code SIAM mentioned before had previously been used to simulate the angle of atmospheric muons under water [Kud00].

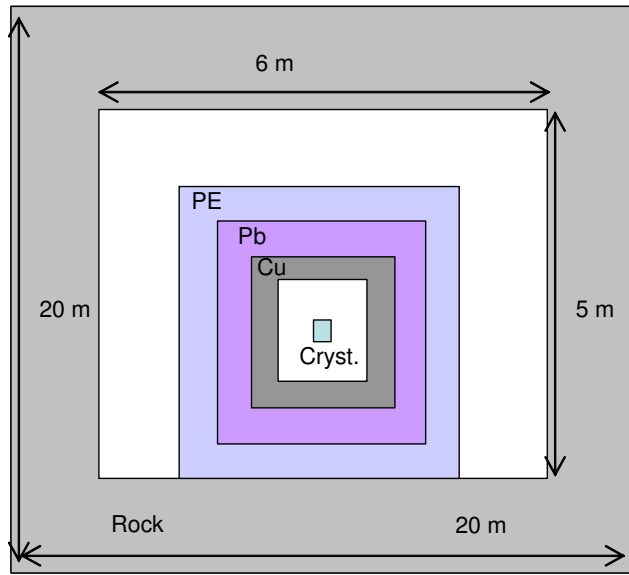


Fig. 4.11 Geometry used in the full simulations of muon-induced neutrons.

In the first simulation muons and neutrons were stopped when entering the hall for the first time. In the second simulation they were allowed to cross the hall so that neutrons could be scattered back into the hall and counted more than once. Additional neutrons could also be produced by muons propagated to the opposite wall and also through spallation of high energy neutrons. Figure 4.12 shows the neutron energy spectra at the boundary of rock and hall for the two cases mentioned above. The total flux of neutrons entering the hall for the first case is $4.27 \times 10^{-10}\text{ n/cm}^2/\text{s}$ ($135\text{ n/m}^2/\text{year}$) above 1 MeV and $8.53 \times 10^{-10}\text{ n/cm}^2/\text{s}$ ($269\text{ n/m}^2/\text{year}$)

for the second case. This shows the effect of back scattering from the walls. A similar result is seen if the experimental setup is placed inside hall.

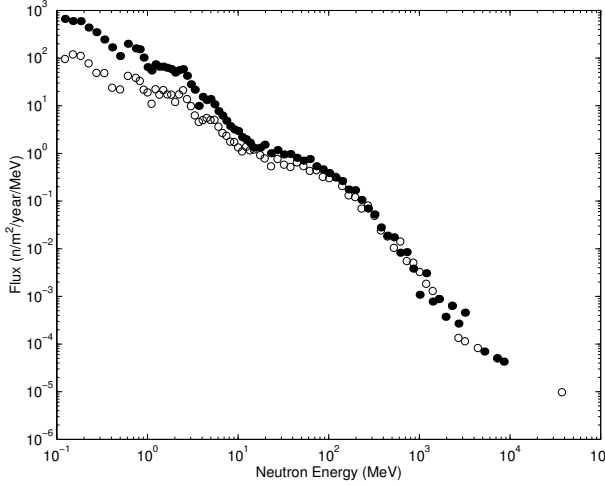


Fig. 4.12 Flux of muon-induced neutrons entering the Gran Sasso hall obtained from simulations in this work. Two cases are shown: without back scattering (open circles) and with back scattering (filled circles).

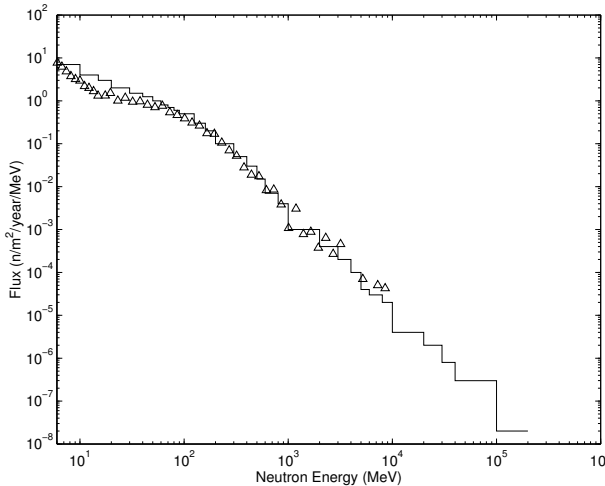


Fig. 4.13 Comparison of Flux of muon-induced neutrons entering the Gran Sasso hall: Dementyev [Dem99](solid line) and this work with back scattering(triangles).

In Figure 4.13 the spectrum reported by Dementyev [Dem99] and the spectrum with back scattering obtained in this work are shown together. It is more likely from this comparison, that Dementyev's energy spectrum is the spectrum with back scattering. It is seen however, that for the energy

range between 6 - 60 MeV Dementyev's flux is higher. Above 6 MeV Dementyev's spectrum gives a total flux of about $200 \text{ n/m}^2/\text{year}$ ($170 \text{ n/m}^2/\text{year}$ between 6 and 100 MeV).

The angular distributions of neutrons entering the hall with energies above 1 MeV are shown separately for the roof, the floor, the walls and total for the cases with and without back scattering in Figure 4.14. Both without and with back scattering, the spectra of neutrons from the roof of the hall are peaked at vertical direction. The angular distribution of neutrons from the walls has a wider spread. Almost all neutrons entering the hall from the floor are back scattered neutrons.

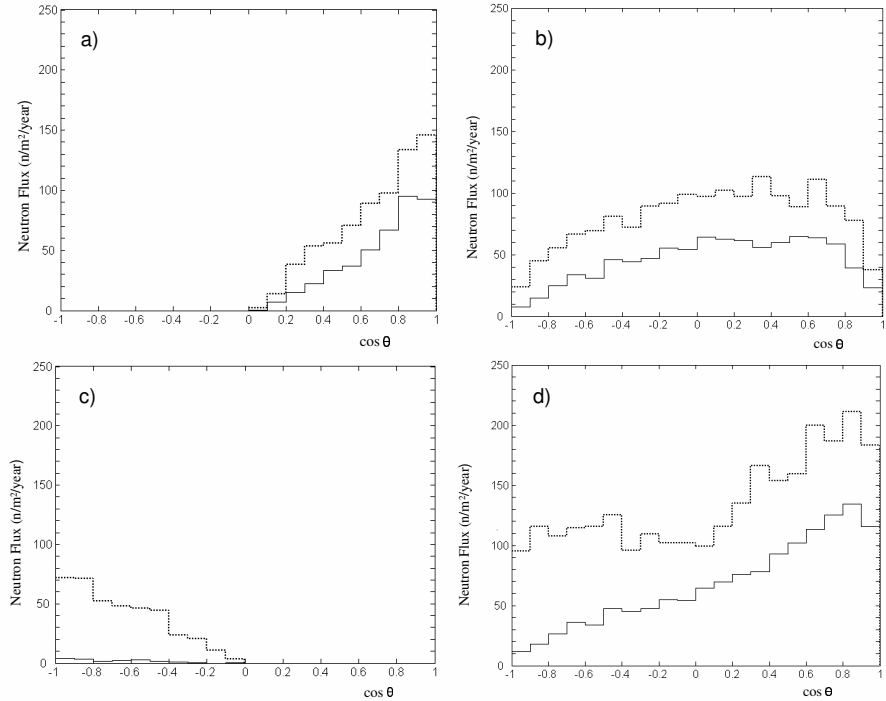


Fig. 4.14 Angular distribution of neutrons entering the hall from a) the roof, b) the walls, c) the floor and d) anywhere with energies above 1 MeV for the case without back scattering (solid lines) and with back scattering (dotted lines).

Energy spectra of neutrons with energies above 1 MeV entering the hall from the roof, the wall and the floor are shown in Figure 4.15 for the cases without and with back scattering. High energy neutrons come mainly from the roof. The number of lower energy neutrons is increased due to scattering.

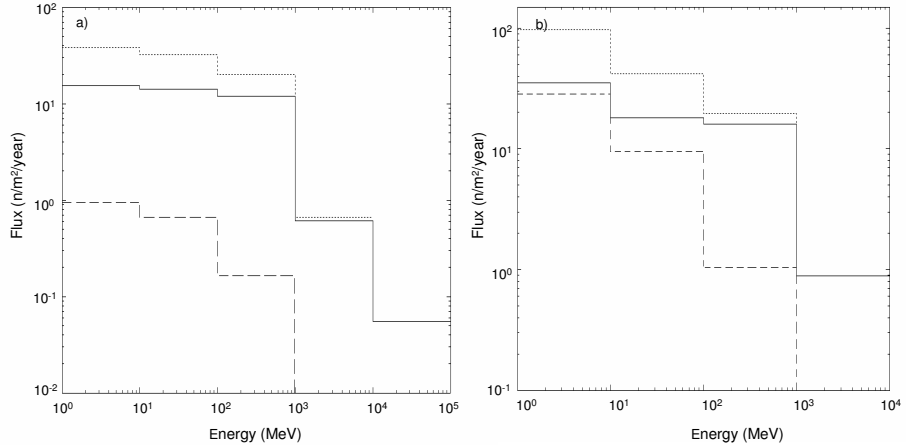


Fig. 4.15 Energy distribution of neutrons entering the hall from the roof (solid lines), the walls (dotted lines) and the floor (dashed lines) for the cases a) without back scattering and b) with back scattering.

4.6.5 Effect of Shielding Materials

It has been previously shown by simulations using Dementyev's spectrum, that high energy neutrons produced by muons in the rock can reach the experimental setup and undergo spallation reactions to produce more neutrons. It has been mentioned also, that this neutron flux will increase the neutron background, and even exceed the contribution of low energy neutrons from activity in the rock if a thick polyethylene shield is used in CRESST. In addition, muons propagating through the experimental setup can also produce additional neutrons. It is interesting, therefore, to see the effect of the use of each shielding material in CRESST to the flux of neutrons at detector level.

To do this, simulations similar to the one performed to get the neutron flux entering the hall with back scattering were done, but this time with the experimental setup placed inside the hall. To see the effect of polyethylene, the lead and copper shields were replaced by vacuum. The neutron flux at the boundary between the detector area and the polyethylene inside the shield is shown in Figure 4.16(a) together with neutron flux entering the hall including back scattering. The effect of lead was studied by replacing the polyethylene and copper shields by vacuum. Figure 4.16(b) shows the flux at the boundary between the detector area and the lead inside the shield. The same was done to see the effect of copper, and the result is shown in Figure 4.16(c). Finally, all shielding materials were put together and the neutron flux at the boundary between the copper shield and the detector area is shown in Figure 4.16(d). One should keep in mind that in all of

these cases neutrons could be produced both in the rock and in the shields. As expected, the lead shield gives more important effect than the other two shields. Below 3 MeV the flux of neutrons at the boundary between the lead shield and the detector area is higher than the flux of neutrons at the boundary between the rock and the hall. Figure 4.16(d) shows the whole effect of neutron production and transport in the shields, which is dominated by the lead shield.

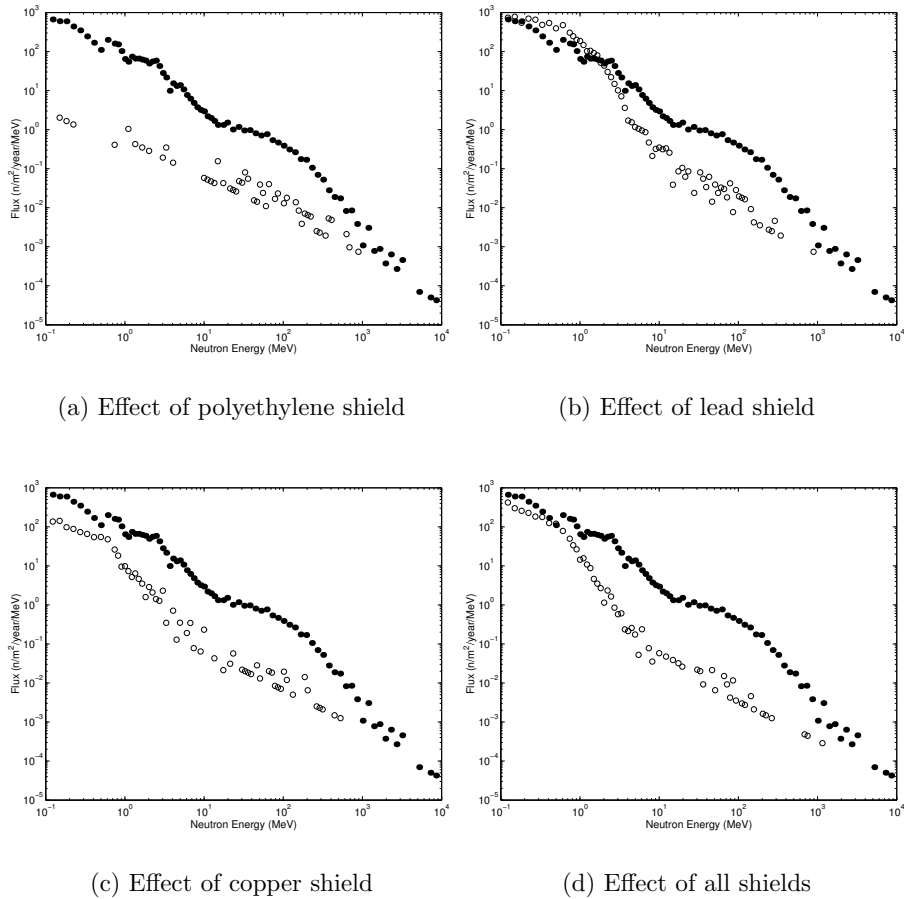


Fig. 4.16 Effect of shielding materials used in CRESST shown by the flux at the boundary between the shield and the detector area inside the shield (open circles). As a comparison the flux of neutrons entering the hall including back scattering is shown (filled circles).

4.6.6 Recoil Spectrum and Count Rate

It would be ideal to follow muons and all their cascade products down to the detector level to finally get the spectrum and count rate of neutron-induced

recoils in the detector crystal. Unfortunately, it needs long computing time to obtain sufficient statistic in this case. Another difficulty is the fact that FLUKA does not treat individual nuclear recoils as has been discussed in subsection 4.6.1.

The problem is actually can be divided into two, namely the recoil spectrum and the count rate induced by high energy neutrons from the rock and those induced by neutrons produced by muons in the experimental setup. Therefore, two separate simulations has been performed and are discussed below.

4.6.6.1 *Recoil Spectrum and Count Rate Induced by High Energy Neutrons from the Rock*

The flux of neutrons entering the experimental hall (including back scattering), that has been obtained with FLUKA and discussed in the previous subsection, was used as input for MCNPX and transported further down to the detector level to get the recoil spectrum. The experimental setup with 50 cm polyethylene shield was placed inside the hall. In the experimental setup these high energy neutrons produced additional neutrons. This procedure is actually similar to what has been done in the second series of simulations of high energy neutrons using the Dementyev's spectrum, as previously discussed in subsection 4.5.2. But this time the surrounding rock was replaced with vacuum, to prevent neutrons from being scattered back by the rock.

Other hadrons (pions and protons) entering the hall were not transported, because of their low fluxes (see Figure 4.5). Recoil spectrum produced by muon-induced neutrons in the rock is shown in Figure 4.17. The

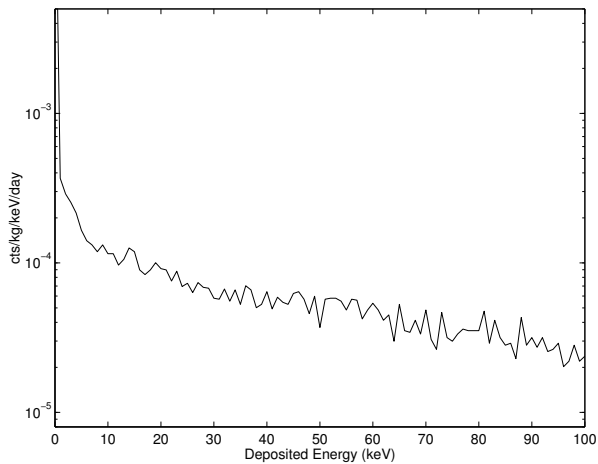


Fig. 4.17 Recoil spectrum induced by high energy neutrons from the rock obtained from the simulation in this work.

count rate at $(15 - 25)$ keV is 8.81×10^{-4} cts/kg/day. This rate is in a good agreement with the rate obtained with Dementyev's spectrum for the setup with 50 cm polyethylene, which is 8.94×10^{-4} cts/kg/day as shown in Table 4.4. The result is higher than the rates for low energy neutrons from activity of the surrounding rock and concrete with the same polyethylene thickness, *i.e.* 9.96×10^{-5} cts/kg/day for the simulation with the measured spectrum and 1.64×10^{-5} cts/kg/day for simulation calculated spectrum (see Table 3.16).

4.6.6.2 Recoil Spectrum and Count Rate Induced by Neutrons Produced by Muons in the Experimental Setup

To determine the contribution of muon-induced neutrons in the experimental setup, muons following the LVD best fit were generated at the hall's surface and the experimental setup with 50 cm polyethylene shield was placed inside the hall. Muons were transported inside the hall and through the experimental setup. The rock surrounding the experimental hall was replaced by vacuum, to avoid muon-induced neutron production therein.

Neutrons produced by muons in the experimental setup and entering the experimental cavity (passing through the boundary between the inner surface of the copper shield and the experimental cavity) were then transported further with MCNP to get the recoil spectrum in the detector crystal.

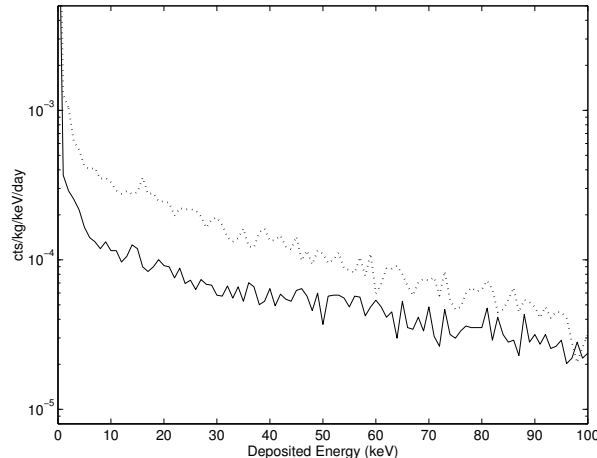


Fig. 4.18 Recoil spectrum induced by high energy neutrons produced by muons in the experimental setup (dotted line). For comparison, recoil spectrum induced by high energy neutrons from the rock is shown (solid line).

In Figure 4.18 the recoil spectrum induced by neutrons produced by muons in the experimental setup is shown by the dotted line and the solid line is the recoil spectrum obtained from the simulation of high energy neutrons from the rock, which is shown for comparison.

The count rate at (15 – 25) keV is 2.78×10^{-3} cts/kg/day. Compared to the rate of low energy neutrons from the activity in the rock and concrete for the setup without moderator, this rate is about 50 times smaller (see Table 4.4). But the rate is higher than that of low energy neutrons moderated with 30 cm polyethylene. With 50 cm polyethylene this result is even higher than the rate of high energy neutrons from the rock, let alone the rate from low energy neutrons from the rock and concrete using the same thickness of polyethylene.

This study, thus, shows the importance of muon-induced neutron background for CRESST phase II, where the use of 50 cm polyethylene is planned. It indicates the necessity of a muon veto for the experiment to cope with the muon-induced neutrons in the experimental setup. Nevertheless, high energy neutrons from the rock seem more difficult to get rid of, because fast neutrons can travel far from the associated muon track as shown by the LVD measurements [Agl99] and reach the detector from large distances.

Chapter 5

The Long Term Perspective for CRESST and Future Experiments

The long term perspective of WIMP searches is to test as large as possible a part of the allowed region of supersymmetry parameter space for neutralino dark matter. In this Chapter the long term goals of CRESST and some future dark matter projects are discussed.

5.1 Long Term Perspective for CRESST

In a detector system with an accurately determined background suppression factor, the sensitivity to the WIMP cross section σ continues to improve as $\sigma \propto 1/\sqrt{Mt}$ [Gai96], where M is the detector mass and t is the measuring time. This holds also for the CRESST scintillation light method.

The experimental volume of the present installation of CRESST can house up to 100 kg of target mass. With a 100 kg detector, the sensitivity shown in Figure 5.1 is expected to be reached in one year of measuring time. Increasing the exposure to about 300 kg years, improving background suppression to about 99.99 % above 15 keV and lowering the background to 0.1 count/kg/keV/day would enable CRESST to cover most of the MSSM parameter of SUSY with neutralino dark matter. But it is obvious from the results of the present work, that these goals would not be achieved without neutron shielding and muon veto (see also discussion in the next Chapter).

In addition to improving limits on dark matter, it is also important to have ways for the positive verification of a dark matter signals as well as elucidation of its nature. CRESST verifies a suspected dark matter signal through the following effects:

- (i) Varying the mass of the target nucleus leads to a definite shift and rescaling in the recoil energy spectrum, which depends on the mass of WIMPs. Hence, the WIMPs mass can be determined directly. Observation of the correct behavior will significantly increase the confidence in a positive signal. It is a great advantage, that the CRESST technology can be applied to different target materials. Simultaneous light

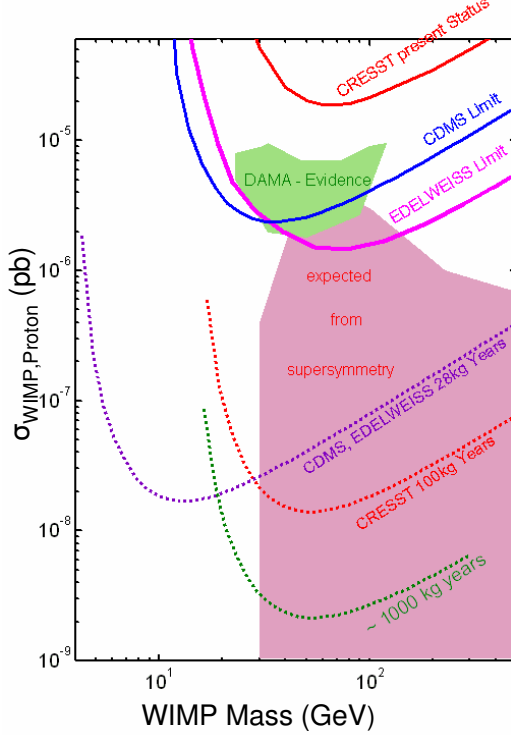


Fig. 5.1 The projected sensitivities of CRESST and some other experiments.

- and phonon measurement is also possible with a variety of materials, e.g. CaWO₄, PbWO₄, BGO.
- (ii) As aforementioned in Chapter 1, a positive signal can also be verified by an annual modulation of the spectral shape and the rate caused by the motion of the Earth around the Sun. The large mass potential of the present CRESST installation should be able to see such an effect in the future.
 - (iii) One important task of WIMP detection is to determine their nature, e.g. for SUSY the gaugino and higgsino content, which gives rise to different strength of the spin dependent interaction. By using different target materials significant steps in this direction can be taken.
 - (iv) The simplest halo model, *i.e.* an isothermal sphere with Maxwellian velocity distribution is arguable. In fact, many investigations indicate that the velocity is distributed anisotropically and that the local density may not be smooth, but clumpy [Gre02]. The high resolution of low temperature detectors allow an accurate determination of the recoil spectrum. Once the WIMP mass can be determined, the velocity distribution in halo can also be calculated. The escape velocity in our

Galaxy limits the highest recoil energy that can be observed. Therefore, the total mass of our Galaxy (and hence also the total mass of dark matter if WIMP is the only dark matter) can be determined by the measurement of the recoil spectrum.

Further phases of the project with a very increased total detector mass will require certain improvements and innovation in the technology, optimization of neutron shielding and muon veto. In addition, a collaboration with European experiments should also be expanded and strengthened.

5.2 Upgrading of Current Experiments

Other current direct searches will also be upgraded in the next phases of the experiments. CDMS II will have 42 detectors for a total mass of $\sim 7\text{ kg}$. It is currently deployed at a depth of 2080 m w.e. in the Soudan mine and should run through 2006. The projected limit is shown in Figure 5.1.

EDELWEISS will be upgraded to 35 kg. It will involve 28 germanium bolometers, a new large volume cryostat, improvement of gamma and neutron shieldings, and a muon veto. The projected limit is also shown in Figure 5.1.

ZEPLIN will be moving to a two-phase (liquid-gas) operation, allowing scintillation and ionization to be measured simultaneously, with a xenon target mass of 30 kg.

All of these experiments (and also CRESST II with 10 kg detector mass) promise about two orders of magnitudes improvement in the next few years, with a target sensitivity of the order of $2 \times 10^{-8}\text{ pb}$.

These experiments, if successful, will then have to be upgraded to tonne-scale experiments. This upgrading is necessary to either confirm the existence of a signal with high statistic, or to sample lower cross section SUSY models. By using different target nuclei, this will allow the determination of the WIMP mass and type of interaction if candidate for WIMP interactions are detected.

5.3 Future Direct Detection Projects

Several 100-kg to tonne-scale dark matter experiments are in planning or proposed, with smaller-scale test versions already running or currently under construction. Many of these experiments allow discrimination of electron recoils from nuclear recoils. If the number of detected WIMP events is large enough and excellent stability of the experimental energy response, efficiency, and background is maintained, it may be possible to detect the annual modulation of the WIMP signal. Detecting the annual modulation would help confirm the discovery, while a lack of annual modulation in the

rate of events could improve an experiment's upper limit by indicating that most of the events detected are not due to WIMPs. Some future projects are discussed below.

The GENIUS project [Bau99b] plans to operate an array of 40-400 highly purified germanium detectors ($100 \text{ kg}^{-1} \text{ t}$) immersed directly in liquid nitrogen. The aim of GENIUS is to reduce the background of the germanium crystals by about three orders of magnitude with respect to current best measurements by removing almost all materials from the immediate vicinity of the detectors and operating the crystals directly in a cold liquid of extreme purity.

The expected sensitivity of GENIUS for the spin-independent WIMP-nucleon cross section for an exposure of 100 kg y and a background level of 10^{-2} counts/kg/keV/y is about 10^{-9} pb . At present a Test Facility is running in Gran Sasso. Its primary goals are to show that 'naked' Ge detectors work reliably in liquid nitrogen over a long period of time (at least one year) and to test material selections for the various experimental components to sensitivities of 1 count/kg/keV/y.

The primary purpose of MAJORANA [Maj02] would be to search for neutrinoless double beta decay. However, it would also be sensitive as a WIMP detector. The experiment's basic concept is to operate multiple Ge diodes in one cryostat system in order to provide a high amount of self-shielding. The WIMP detection method is based on measuring the ionization signal in conventional, segmented Ge diodes.

The planned exposure of MAJORANA is 5000 kg years , allowing increased sensitivity by searching for the predicted annual modulation of the event rate and energy spectrum. Assuming a flat background of $0.005 \text{ counts/kg/keV/day}$ between threshold (1 keV) and 20 keV ionization energy, the expected sensitivity of MAJORANA for spin-independent WIMP-nucleon cross section *via* annual modulation extent down to about 10^{-9} pb .

CryoArray [Gai01], using the same technology as CDMS, would use a large array of germanium and silicon detectors cryogenically cooled to $\sim 25 \text{ mK}$. To reach its goal of sensitivity to 10 WIMP interactions per year, which is corresponding to a WIMP-nucleon cross section of 10^{-10} pb , CryoArray needs relatively modest improvements over CDMS, as long as the experiment is sited deep enough so that the fast neutron background become negligible. The photon background needs to be reduced by $\sim 25 \times$, through the combination of better material screening and better self-shielding.

The ZEPLIN IV project, with ZEPLIN II as prototype, is a proposal for a tonne two-phase (liquid and gas) Xenon detector [Cli01]. The goal is to measure both scintillation and electroluminescent photons, allowing discrimination between electron and nuclear recoils.

ZEPLIN II is under construction at UCLA and will be installed at the Boulby mine, in England. The plan is to design the one tonne ver-

sion, ZEPLIN IV, using the same principle as ZEPLIN II. The projected sensitivity of ZEPLIN IV is about 5×10^{-9} pb for a raw background of 2 counts/kg/keV/day and 360 days of exposure.

XENON is a proposal for a modular liquid Xenon experiment with 10 TPCs (Time-Projection Chambers), each containing 100 kg of active Xe target (see [Xen02] and reference therein). XENON would be a two-phase Xenon experiment, detecting both primary and proportional scintillation signals. The electrons produced in a nuclear or electron recoil are drifted to the gas phase where they induce proportional scintillation light in a strong electric field.

The extrapolated sensitivity of XENON with 1 tonne target material and 3 years of exposure is 4×10^{-10} pb for a background of 3.9×10^{-2} counts/t/keV/day with 99.5% nuclear recoil discrimination and a visible energy threshold of 4 keV (corresponding to 10 keV recoil energy in liquid Xenon) [Xen02]. A prototype with 7 kg of active material to test all design aspects and technical innovations, and to demonstrate the high background-rejection efficiency and low energy threshold is foreseen.

The DRIFT (Directional Recoil Identification From Track) experiment [Sno00] uses a negative-ion TPC. The negative ions are created by the slightly electronegative gas attaching to the electrons produced by a recoil track. Since negative ions diffuse much less than electrons do, no external magnet is needed to prevent diffusion, and sub-mm resolution is obtainable even after drifting the ions for meters. Measurements of the range of the recoil together with the total ionization caused should allow near-perfect rejection of background photons and electrons.

A cubic prototype with 2-mm resolution and 250 g of CS₂ gas is currently running at the Boulby mine. A second version with 0.5-mm resolution and increased pressure (and hence mass) is being proposed. DRIFT III would be a larger-scale version of the second generation experiment, with 100 m³ gas at 160 torr, for a total active mass of ~ 100 kg. The relatively low mass (compared to other future experiments mentioned before) would likely limit the experiment's sensitivity to a WIMP-nucleon cross section of 10^{-9} pb (corresponding to 10 counts/year), depending somewhat on the Z of the gas ultimately used.

The primary advantage of the DRIFT experiment is that it should provide the direction of the recoil. In such an experiments which is recoil-direction sensitive, the diurnal modulation due to the Earth's rotation can be made use. This diurnal modulation results in $\sim 10\%$ daily asymmetry, significantly larger than the size of an annual modulation, and less susceptible to possible systematic effects. Moreover, this directional information could potentially be used to get some information about the distribution of WIMPs in the Galaxy.

Chapter 6

Summary and Outlook

A host of astrophysical measurements now provides a reliable inventory of the content of the Universe. Measurements of the first acoustic peak in the angular power spectrum of the Cosmic Microwave Background (CMB) have given compelling evidence that the Universe is very near to flat, *i.e.* $\Omega \approx 1$, consistent with the prediction from inflation. Moreover, independent observations yield consistent results for the total densities of baryonic and non-baryonic matter, as well as for the amount of the so-called dark energy. A consistent inventory of the Universe is: dark energy density $\Omega_\Lambda \approx 0.7$, total matter density $\Omega_m \approx 0.3$, and baryonic density $\Omega_b \approx 0.04$. The fact that stars and other observed luminous matter account for only $\sim 1\%$ of the total density means that most of the baryonic matter consists of unknown, dark components.

A large number of candidates has been proposed for both baryonic and non-baryonic dark matter. The most famous candidates are MACHOs in the baryonic sector and neutralinos (WIMPs) in the non-baryonic sector.

WIMPs have been searched for by employing various techniques that basically can be divided in indirect and direct searches. Indirect searches look for particles produced by WIMP annihilation in celestial objects. Direct searches look for WIMP elastic scattering off nuclei in a detector, where the main observable is the energy in the range of some keV to ~ 100 keV deposited by the recoiling nucleus. Direct searches can be divided according to their ability to distinguish nuclear recoils from electron recoils.

DAMA, a direct search, has reported a possible evidence for the annual modulation, which can be a signature of WIMPs. This evidence is unfortunately not supported by other recent experiments employing different techniques.

CRESST phase I has shown the operation of 262 g sapphire in the milli-Kelvin range under low background condition. It improves the existing limit for the low WIMP-masses for spin-dependent interaction.

The use of light-phonon detector in the second phase of CRESST, which enables discrimination between electron recoils and nuclear recoils, will leave the neutron flux in Gran Sasso as the main background for the experiment.

This neutron background will in turn limit the sensitivity of the experiment. It is obvious that CRESST II and other current and future direct dark matter searches have to cope with neutron background to reach high sensitivity.

Neutrons present at the experimental setup come from different origins: radio activity of the vicinity (rock and concrete) and material used in the setup, and from cosmic ray muons that produce neutrons in the rock and in the experimental setup. The bulk of the flux of neutrons in the experimental site is given by neutrons from radioactivity in the rock and concrete.

Calculations and simulations have been done to recheck the results of neutron flux measurements reported by several author and to get more detailed information on the energy spectrum. Above 1 MeV the present work is in agreement with the measurement reported by Belli *et al.* [Bel89]. The present work has shown that low energy neutrons entering the Gran Sasso halls mainly come from the concrete layer, and no significant difference was found in the total flux of neutrons in different halls.

Both measured [Bel89] and calculated/simulated flux indicate the necessity of a neutron moderator for CRESST II. A neutron moderator of 50 cm polyethylene is planned for CRESST II, and an improvement in the sensitivity by a factor of more than three orders of magnitude is expected.

It has been shown in the present work, that variation in the water content of the concrete layer could result in a variation of the count rate in the detector. But without monitoring the variation of the water content in the concrete layer throughout the year, it is hard to say whether this effect can have something to do with the modulation observed by DAMA.

The present work indicates that neutrons from radioactivity of the lead shield as low as 0.1 ppb of ^{238}U induce about five times more background counts in the detector than low energy neutrons from outside (from the rock and concrete) after being moderated by 50 cm polyethylene.

Muon flux and energy spectrum at the depth of Gran Sasso have been determined with the MUSIC and SIAM codes in the present work. A flat mountain surface was assumed as an approximation, but a further study to take the detail mountain profile of Gran Sasso into account is planned for the near future.

Simulations to determine the rate of muon-induced neutron production of materials relevant for CRESST have been performed with FLUKA. The highest production rate is found in lead, $\sim 4.3 \times 10^{-3} \text{ n}/\mu\text{/}(g/cm^2)$. This result is in agreement with the measurement by Gorshkov [Gor73] but disagrees with the result reported by Bergamosco [Ber73]. An extrapolation from several experiments [Ber73] and theoretical predictions however suggest a product of multiplication and cross section, $\bar{m}\sigma$, about three times lower than Bergamosco's result. An agreement between neutron production reported by Gorshkov and the result of the present work with Bergamosco's

result is reached if the neutron production rate reported by Bergamosco is divided by three.

The energy spectrum of high energy neutrons produced by muons in the rock (including back scattering) entering the hall obtained in the present work is in a good agreement with simulation result reported by Dementyev *et al.* [Dem99]. The count rates obtained with the two spectra are also in agreement. However, the count rates are nine times higher compared to the rate from low energy neutrons from activity of rock and concrete after being moderated by 50 cm polyethylene.

Muons present in the hall can enter detector setup and produce neutrons. The effect of the polyethylene, lead, and copper shields in CRESST has been investigated. The count rate in the detector induced by neutrons from this origin is 2.78×10^{-3} cts/kg/day at 15-25 keV, about 25 times higher than the rate from low energy neutrons from the rock in the same energy range.

To summarize the results of this study on the neutron-induced background, the contributions of the different neutron sources to the count rate at 15-25 keV in a 100 kg CaWO₄ detector per year are shown in Table 6.1. All the cases shown are obtained using a simple setup. Taking the count rate obtained with the measured low energy neutron flux from the rock [Bel89] after being moderated by 50 cm polyethylene as a unit, the contributions of the other sources are shown as multiplication factors of the unit in Table 6.1. It is obvious that neutrons produced by muons in the shield will dominate the background rate in CRESST if a 50 cm polyethylene shield is used.

Table 6.1 Contributions of different neutron sources to the count rate at 15-25 keV in CaWO₄ detector.

Neutron origin	Count Rate (15-25 keV) cts/100kg/y	Multiplication Factor
Low energy neutrons from fission and (α, n) in the rock: (i) no moderator	5000	1250
(ii) Pb/Cu + 50 cm PE	4	1
Low energy neutrons from fission of 0.1 ppb ²³⁸ U in the lead	20	5
High energy neutrons produced by muons in the rock	30	8
High energy neutrons produced by muons in the shields	100	25

Higher and higher sensitivity is pursued by current experiments and several new projects are proposed. In Figure 6.1 the projected sensitivities of some experiments are shown together with the present sensitivities of some running experiments. Contributions of different neutron sources on the recoil signal in CRESST are shown, to indicate the levels at which they will limit the sensitivity of CRESST. They are not shown as sharp lines, just to indicate that the contributions are based on the present status of simulations and may change if new simulations that may be done in the future show improved results. Suppressions of background by the use of a muon veto are also shown.

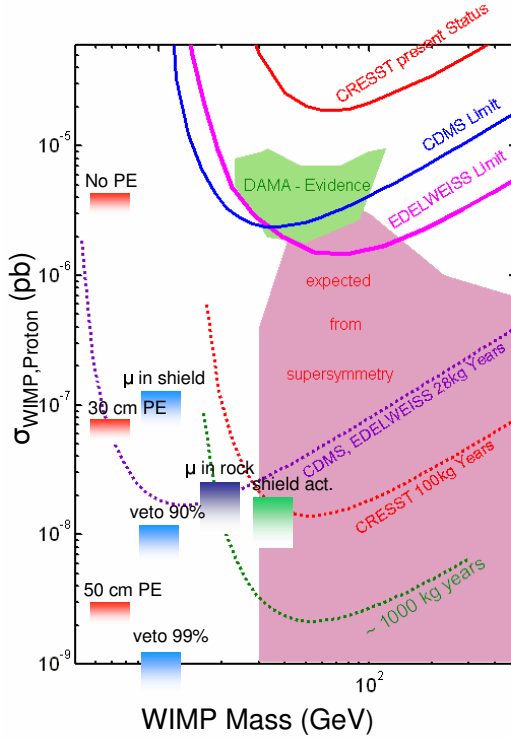


Fig. 6.1 The projected sensitivities of some experiments and limitation of the CRESST sensitivity by neutron background under different conditions.

It is shown in Figure 6.1 that without muon veto, the sensitivity of CRESST will be limited to be around 10^{-7} pb, hence the goal of CRESST II of some 10^{-8} pb would be endangered. But Table 6.1 shows that muon veto would bring a reduction factor of only three unless high energy neutrons from the rock and low energy neutrons from ^{238}U in the lead shield can be overcome.

It is expected that background induced by high energy neutrons produced

by muons in the rock can be reduced, if multiple scattering is taken into account. To show this possibility, an array of crystals should be used in the simulations instead of a single crystal. Neutrons scattered in more than one crystal can be rejected as background, because WIMPs do not scatter multiply. In addition to lower energy neutrons, photons are also produced in spallation reactions of high energy neutrons in the lead and copper shield. If these neutrons arrive together with photons in the crystals, they can also be discriminated. Such a simulation could be done in the future with the codes and tools used in this work to ascertain, whether multiple scattering can solve the problem of high energy neutrons from “outside”.

There was an idea to use liquid scintillator, instead of polyethylene, as neutron moderator. A liquid scintillator is not only less expensive, but at the same time can serve as a muon veto. Unfortunately, this idea has to be put aside or at least postponed, after an accident with liquid scintillator happened at the experiment BOREXINO in Gran Sasso.

Alternatively, the lead shield should be placed outside the polyethylene shield, as is applied in ZEPLIN. Simulations show that this setup is effective in suppressing the neutron flux induced by muons in the lead [Kud03d].

It is obvious, that protection against neutron background will be one of the key issue for the next generation of direct detection of dark matter. Therefore, this topic is now intensively studied and discussed by many groups, including ETNo μ Siq (European Team for Neutron and μ Simulation and Qualification), a working group of the CRESST, EDELWEISS and UKDM collaborations.

List of Figures

1.1	Rotation curve for the spiral galaxy NGC6503	5
1.2	DAMA Modulation	18
1.3	Limits on the WIMP-nucleon cross section for scalar interactions as a function of the WIMP mass	19
2.1	Transition curve of a super conducting thermometer	24
2.2	Schematic view of the arrangement used for the simultaneous light and phonon detection	25
2.3	Pulse height in the light detector versus pulse height in the phonon detector	26
2.4	Layout of the dilution refrigerator and cold box	27
2.5	Energy spectrum of the CRESST I measurement at Gran Sasso	28
2.6	Equivalent WIMP-proton cross section limit for spin dependent interaction as a function of WIMP mass from the CRESST I measurement	29
2.7	Equivalent WIMP-proton cross section limit for spin independent interaction as a function of WIMP mass from CRESST I measurement	30
2.8	Expected WIMP-nucleon cross section limits for scalar interactions as a function of WIMP mass for CRESST II	32
3.1	Mean neutron energy <i>vs.</i> rate from the ICARUS neutron flux measurement	37
3.2	Energy spectrum of neutrons from spontaneous fission of 1 ppm ^{238}U	38
3.3	Energy spectra of neutrons from (α, n) reactions	46
3.4	Typical depths of neutrons from (α, n) and fission reactions in hall A rock and in dry concrete	47
3.5	Comparison of a simulated and a calculated recoil spectrum of W hit by 10 MeV neutrons	49
3.6	Simple geometry with Pb/Cu shields used in the simulations.	50

3.7	Recoil spectrum of sapphire in CRESST phase I obtained from simulation with the simple Pb/Cu shields setup	50
3.8	Recoil spectrum of CaWO ₄ in CRESST phase II with the simple Pb/Cu shield setup	51
3.9	Recoil spectrum in CaWO ₄ in a setup with Pb/Cu and 50 cm of polyethylene	53
3.10	Spectra of low energy neutrons from the rock/concrete used in the simulations	53
3.11	More realistic setup with polyethylene used in the simulations	54
3.12	Recoil spectra obtained with a measured spectrum for a realistic setup	55
3.13	Variation in the count rate due to the change of humidity in the concrete (simple setup without neutron moderator)	56
3.14	Variation in the count rate due to the change of humidity in the concrete (simple setup with 50 cm polyethylene)	56
3.15	Recoil spectrum due to neutrons produced by spontaneous fission in the lead shield	58
4.1	Energy loss dE/dx of high energy muons in standard rock . .	64
4.2	Mean energy of the vertical muon flux	67
4.3	Vertical muon intensity <i>vs.</i> depth in standard rock	69
4.4	Neutron production rate as a function of the mean muon energy	72
4.5	Energy spectrum of muon-induced hadrons in the rock entering the Gran Sasso hall	73
4.6	Angular distribution of neutrons entering the experimental hall	74
4.7	Recoil spectrum induced by high energy neutrons (Dementyev's Spectrum) for the simple setup with 50 cm polyethylene.	76
4.8	Spectrum of neutrons when entering hall (Dementyev's spectrum) and at the outer surface of the experimental setup (after scattered inside the hall)	76
4.9	Recoil spectra induced by high energy neutrons (Dementyev's spectrum) started at the surfaces of the laboratory hall . . .	77
4.10	Neutron production from 270 GeV muons as a function of the atomic weight A of materials relevant for CRESST . . .	82
4.11	Geometry used in the full simulations of muon-induced neutrons	85
4.12	Flux of muon-induced neutrons entering the Gran Sasso hall obtained from simulations in this work	86
4.13	Comparison of the flux of muon-induced neutrons entering the Gran Sasso hall	86
4.14	Angular distribution of neutrons entering the hall obtained in this work	87
4.15	Energy distribution of neutrons above 1 MeV entering the hall from the roof, the walls and the floor	88

4.16	Effect of shielding materials used in CRESST shown by the flux at the boundary between the shield and the detector area inside the shield	89
4.17	Recoil spectrum induced by high energy neutrons from the rock obtained from the simulation in this work	90
4.18	Recoil spectrum induced by high energy neutrons produced by muons in the experimental setup	91
5.1	The projected sensitivities of CRESST and some other experiments	94
6.1	The projected sensitivities of some experiments and limitation of the CRESST sensitivity by neutron background . . .	102

List of Tables

1.1	Maximum recoil energies for neutron-induced and WIMP-induced events.	21
3.1	Detection methods for the neutron flux measurements at Gran Sasso.	36
3.2	Neutron flux measurements at LNGS reported by different authors.	36
3.3	Correction for σ in the ICARUS neutron flux measurement.	37
3.4	Mass Stopping power of elements at 8 MeV.	41
3.5	Chemical composition of LNGS rock.	41
3.6	^{238}U and ^{232}Th activities in LNGS rock.	41
3.7	Chemical composition of LNGS dry concrete.	42
3.8	α -Emitters in the ^{238}U and ^{232}Th chains.	42
3.9	Neutron yields from (α, n) interactions in hall A rock.	43
3.10	Neutron yields from (α, n) interactions in hall C rock.	43
3.11	Neutron yields from (α, n) interactions in dry concrete (8% water content).	44
3.12	Neutron yields from (α, n) interactions in wet concrete (16% water content).	45
3.13	Neutron energy of elements for different α -energies, averaged over “open” isotopes.	45
3.14	Neutron flux in hall A and hall C.	48
3.15	Flux of neutrons entering the CaWO_4 crystal with energies above 70 keV.	52
3.16	Neutron background count rates in the 15-25 keV energy range in CaWO_4 for different thicknesses of polyethylene.	52
4.1	Average muon range R and energy loss parameters calculated for standard rock.	66
4.2	Comparison of parameters of standard rock with Gran Sasso rock.	66

4.3	Neutron production rates by spallation of high energy neutrons in lead.	74
4.4	Count rates at 15-25 keV in CaWO ₄ induced by high energy neutrons (Dementyev's spectrum) sampled at the outer surface of the Pb shield.	75
4.5	Count rates at 15-25 keV in CaWO ₄ induced by high energy neutrons (Dementyev's spectrum) sampled at the hall surface.	77
4.6	Neutron production rates from 270 GeV muons in several materials.	82
4.7	Neutron production rate from muons with the LVD best fit spectrum in several materials.	83
4.8	Neutron production rate from muons with Gaisser's parametrization in several materials.	83
4.9	Measured neutron production in the CERN NA55 experiment.	84
6.1	Contributions of different neutron sources to the count rate at 15-25 keV in CaWO ₄ detector.	101

Bibliography

- [Abr02] Abrams, D. *et al.*, CDMS-Collaboration, Phys. Rev. D (2002) 122003; astro-ph/0203500.
- [Agl89] Aglietta, M. *et al.*, Nuovo Cim. Soc. It. Fis. C 12 (1989) 467.
- [Agl95] Aglietta, M. *et al.*, (LVD Collaboration), Astropart. Phys. 3 (1995) 311.
- [Agl98] Aglietta, Phys. Rev. D 58 (1998) 092005.
- [Agl99] Aglietta, M. *et al.*, in Proc. 26th Intern. Cosmic Rays Conf., V.2 (1999) 44; hep-ex/9905047.
- [Agl99b] Aglietta, *et al* (The LVD-Collaboration), Phys. Rev. D 60 (1999) 112001.
- [Ahl87] Ahlen,S.P., *et al.*, Phys. Lett. B 195 (1987) 603.
- [Alc00] Alcock, C. *et al.*, Astrophys. J. 542 (2000) 257; Alcock, C. *et al.*, astro-ph/0001272
- [Alc00b] Alcock, C. *et al.*, Astrophys. J. 542 (2000) 281.
- [Ale88] Aleksan, R. et al., DphPE. 88-09, June (1988).
- [All91] Allesandrello, A. *et al.*, Nucl. Inst. Meth. in Phys. Res. B61 (1991)106.
- [Amb95] Ambrosio, M. *et al.*, (MACRO-Collaboration), Phys. Rev. D 52 (1995) 3793.
- [And87] Andreev, Yu. M., Gurentzov, V.I. and Kogai, I.M., in Proc. 20th Int. Cosmic Rays Conf., Vol. 6, (Moscow), (1987) 200.
- [Ang02] Angloher, G. *et al.*, CRESST-Collaboration, Astropart. Phys. 18 Vol. 1 (2002) 43.
- [Ant97] Antonioli, P. *et al.*, Astropart. Phys. 7 (1997) 357.

- [Ant99] Antonioli, P., Kudryavtsev, V.A., Korolkova, E.V. and Spooner, N.J.C., Phys. Lett. B 471 (1999) 251.
- [Arn99] Arneodo, F. *et al.*, Il Nuovo Cim. 112 A, N.8 (1999) 819.
- [Bae98] Baer, H. and M. Brhlik, Phys. Rev. D 57 (1998) 567.
- [Bau98] Baudis, L. *et al.*, Nucl. Inst. Meth. in Phys. Res. A 418 (1998) 348.
- [Bau99] Baudis, L. *et al.*, Phys. Rev. D 59 (1999) 022002.
- [Bau99b] Baudis, L. *et al.*, Nucl. Inst. Meth. in Phys. Res. A 426 (1999) 425.
- [Baz99] Bazarko, A.O., hep-ex/9906003.
- [Bel48] Belenkiĭ, S.Z., Cascade Processes in Cosmic Rays, OGIZ-Gostekhizdat Publ., Moscow, (1948).
- [Bel85] Bellotti, E. *et al.*, INFN/TC-85/19, October 1985.
- [Bel89] Belli, P. *et al.*, Il Nuovo Cim. 101 A, N.6 (1989) 959.
- [Bel91] Bellini, G. *et al.*, Borexino Proposal to Gran Sasso Laboratory, (1991) 184.
- [Bel96] de Bellefon, A. *et al.*, EDELWEISS-Collaboration, Astropart. Phys. 6 (1996) 35.
- [Bel02] Belli, P., to appear in Proceedings of IDM2002 Conf., 4th Int. Workshop on Identification of Dark Matter, York-England, 2002.
- [Ben02] Benoit, A. *et al.*, EDELWEISS-Collaboration, Phys. Lett. B 545 (2002) 43; astro-ph/0206271.
- [Ben03] Bennet, C.L. *et al.*, http://lambda.gsfc.nasa.gov/product/map/pub_papers/firstyear/basic/wmap_basic_result.pdf
- [Ber73] Bergamosco, L, Costa, S. and Picchi, P., Il Nuovo Cim. 13A, N.2 (1973) 403.
- [Ber89] Berger, Ch. *et al.*, Phys. Rev. D 40 (1989) 2163
- [Ber97] Berezinsky, V., Cold Dark Matter, Invited talk at the Int. Workshop “Non-Accelerator New Physics”, July, 1997, Dubna, Rusia.
- [Ber98] Bernabei, R. *et al.*, Phys. Lett. B 424 (1998) 195.
- [Ber00] Bernabei, R. *et al.*, ROM2F/2000/01.

- [Ber00b] Bernabei, R. *et al.*, DAMA-Collaboration, Phys. Lett. B 480 (2000) 23.
- [Bez73] Bezrukov, L.B. *et al.*, Yad. Fiz. 17 (1973) 98 (Sov. Journ. Nucl. Phys., 17 (1973) 51).
- [Bez81] Bezrukov, L.B. and Bugaev, E.V., Yad. Fiz. 33 (1981) 1195.
- [Bil89] Bilokon, H., *et al.*, Nucl. Inst. and Meth. in Phys. Res. A 303 (1989) 381.
- [Boe00] Boehm, F. *et al.*, Phys. Rev. D 62 (2000) 092005.
- [Bot98] Bottino, A., Dark Matter, 5th School on Non-Accel. Part. Astro., Trieste, 1998.
- [Bra99] Bravini, M. *et al.*, CRESST Collaboration, Astro. Part. Phys. 12(1999) 107.
- [Bri92] Briel, U. G., Henry, J. P., and Boehringer, H., Astron. and Astrophys. 259 (1992) L31.
- [Bri97] Briesmeister, J.F., Ed., “MCNP-A General Monte Carlo N-Particle Code, Version 4B”, LA-12625-M, Los Alamos National Laboratory (March 1997).
- [Bri02] Brink, P., to appear in Proceedings of IDM2002 Conf., 4th Int. Workshop on Identification of Dark Matter, York-England, 2002.
- [Bul82] Bulanenko, V.I., Frolov V.V., and Tsenter É.M., At. Energ. 53 (1982) 160.
- [Cas95] Castagnoli, C. *et al.*, Phys. Rev. D 52 (1995) 2673.
- [Cas97] Castagnoli, C. *et al.*, Astropart. Phys. 6 (1997) 187.
- [Cas98] Caso, C., Particle Data Group, “Review of Particle Physics”, The European Physical Journal C3 (1998) 1.
- [Cat86] Catalano, P.G. *et al.*, Mem. Soc. Geol. It., 35 (1986) 647.
- [Cdm02] CDMS-Collaboration, astro-ph/0203500
- [Ceb99] Cebrian, S. *et al.*, Astropart. Phys. 10 (1999) 361.
- [Cha02] Chazal, V. *et al.*, Nucl. Inst. Meth. in Phys. Res. A 490 (2002) 334.
- [Cli01] Cline, D.B., Wang, H., and Seo, Y., astro-ph/0108147.

- [Coo93] Cooper, S. *et al.*, Proposal to the Gran Sasso Laboratory for a Dark Matter Search using Cryogenic Detector, MPI-PhE/93-29, November 1993.
- [Cre01] CRESST-Collaboration, Proposal to the Gran Sasso Laboratory for a Second Phase of the CRESST Dark Matter Search.
- [Cri95] Cribier, M. *et al.*, Astropart. Phys. 4 (1995) 23.
- [Cri97] Cribier, M., Astrpart. Phys. 6 (1997) 129.
- [Cro87] Crouch M., in Proc. 20th Int. Cosmic Rays Conf., Vol. 6, (Moscow), (1987) 165.
- [DeM92] De Marzo, C, Nucl. Inst. Meth. in Phys. Res. A 314 (1992) 380.
- [Dem94] Dementyev, A.V., Sobolevsky, N.M., SHIELD-a Monte Carlo Hadron Transport Code, in Proc. of Specialist' Meeting "Intermediate Energy Nuclear Data: Models and Codes", Paris, May 30-June1, 1994. NEA OECD, Paris, 237; Dementyev, A.V., Sobolevsky, N.M., Stavissky, Y.Y., Nucl. Inst. Meth. in Phys. Res. A 374 (1996) 70.
- [Dem99] Dementyev, A., *et al.*, Nucl. Phys. B (Proc. Suppl.) 70 (1999) 486. Nucl. Inst. Meth. in Phys. Res. A 314 (1992) 380.
- [Dek99] Dekel, A., astro-ph/9911501.
- [DeP93] De Pascale, M.P., *et al.*, J. Geophys. Res. 98 (1993) 3501.
- [Dod01] Dodelson, S. *et al.* (SDSS Collaboration), Astrophys. J. 572 (2001) 140.
- [Don98] Donato, F., Fornengo, N., and Scopel, S., Astropart. Phys. 9 (1998) 247.
- [Dra02] Drain, D., to appear in Proceedings of IDM2002 Conf., 4th Int. Workshop on Identification of Dark Matter, York-England, 2002; astro-ph/0206271.
- [Dru86] Drukier, A., Freese, K. and Spergel, D., Phys. Rev. D 33 (1986) 3495.
- [Eit00] Eitel, K., New J. Phys. 2 (2000) 1.
- [Ell91] Ellis, J. and Flores, R.A., Phys. Lett. B 263 (1991) 259.
- [Eng89] Engel, J. and Vogel, P., Phys. Rev. D 40 (1989) 3132.
- [Eng95] Engel, J., Phys. Rev. C52 (1995) 2216.

- [Eni87] Enikeev, R.I. *et al.*, Yad. Fiz. 46 (1987) 1492 [Sov. Journ. Nucl. Phys., 46 (1987) 883].
- [Fas00] Fasso, A., Ferrari, A. and Sala, P.R., in Proceedings of the Monte Carlo 2000 Conference, (Lisbon, October 23-26, 2000), Eds. A.King, F.Barao, M.Nakagawa, L.Tavora, P.Vaz, Springer-Verlag, Berlin (2001) 159; Fasso, A., Ferrari, A., J.Ranft and Sala, P.R., ibid. 995.
- [Fei68] Feige, Y., Oltman, B.G., and Kastner, J., Journal of Geophys. Research Vol. 73, No. 10 (1968) 3135.
- [Fie00] Fields, B.d., Freese, K., and Graff, D.S., Astrophys. J. 534 (2000) 265.
- [Fog03] Fogli, G.L., Lisi, E., Marrone, A., Montanino, D. and Rotunno, A.M., Phys. Rev. D 67 (2003) 073002; hep-ex/0212127.
- [Fre88] Fresse, K., Frieman,J. and Gould, A., Phys. Rev., D 37 (1988) 3388.
- [Fre01] Freedman, W.L. *et al.*, Astrophys. J. 553 (2001) 47.
- [Fus02] Fushimi, K., to appear in Proceedings of IDM2002 Conf., 4th Int. Workshop on Identification of Dark Matter, York-England, 2002.
- [Gai90] Gaisser, T.K., “Cosmic Rays and Particle Physics”, Cambridge University Press, (1990)
- [Gai96] Gaitskell, R., Barnes, P.D., DaSilva, A., Sadoulet, B. and Shutt, T., Nucl. Phys. B (Proc. Suppl.) 51B (1996) 279.
- [Gai01] Gaitskell, R. astro-ph/0106200.
- [Gai03] Gaitskell, R. and Mandic, V., available at <http://dmtools.berkeley.edu/limitplots/>
- [Ger02] Gerbier, G., private communication.
- [Ger03] Gerbier, G., private communication.
- [Gol01] Golwala, S., Ph.D. Thesis, Univ. of California, Berkeley, available at <http://cosmology.berkeley.edu/preprints/cdms/golwalathesis/>
- [Gon99] Gondolo, P., and J. Silk, Phys. Rev Lett. 83 (1999) 1719.
- [Gor73] Gorshkov, Atom. Energy. Vol. 34 No. 3 (1973) 210.

- [Gra99] Graff, D.S., Freese, K., Walker, T.P., and Pinsonneault, M.H., *Astropys. J. Lett.* 523 (1999) l77.
- [Gre66] Greisen, K., *Phys. Rev. Lett.* 16 (1966) 748.
- [Gre01] Grego, L. *et al.*, *Astrophys. J.* 552 (2001) 2.
- [Gre02] Green, A., to appear in Proceedings of IDM2002 Conf., 4th Int. Workshop on Identification of Dark Matter, York-England, 2002.
- [Gri88] Griest, K., *Phys. Rev. D* 37 (1988) 2703.
- [Gri90] Griest, K., Kamionkowski, M., and Turner, M.S., *Phys. Rev. D41* (1990) 3565.
- [Gro01] Groom, D.E., Mokhov, N.V., and Striganov, S.I., “Muons stopping power and range tables,” *Atomic Data and Nuclear Data Tables* 78 (2001) 183.
- [Gur76] Gurentsov, V.I. *et al.*, *Sov. J. Nucl. Phys.* 23 (1976) 527.
- [Hag02] Hagiwara, K. *et al.*, *Phys. Rev. D66* (2002) 010001-1.
- [Hal01] Halverson, N.W. *et al.*, *astro-ph/0104489*.
- [Hea89] Heaton, R., Lee, H., Skensved, P, and Robertson, B.C., *Nucl. Inst. Meth. in Phys. Res. A276* (1989) 529.
- [Hea90] Heaton, R., Lee, H., Skensved, P, and Robertson, B.C., *Nucl. Geophys.* 4 N.4, (1990) 499.
- [Hea02] Heaton, R., private communication.
- [Hei98] Heisinger, B., PhD. Thesis, Technische Universität München, 1998.
- [Hel56] Helm, R.H., *Phys. Rev.* 104 (1956) 1466.
- [Her95] Hertenberger, R., Chen, M., and Dougherty, B.L., *Phys. Rev. C* 52 (1995) 3449.
- [Hu97] Hu, W., Sugiyama, N., and Silk, J., *Nature* 386 (1997) 37.
- [Iba99] Ibata, R.A. *et al.*, *Astrophys. J.* 524 (1999) L95.
- [Jun96] Jungman, G., M. Kamionkowski, and K. Griest, *Phys. Rep.* 267 (1996) 195.
- [Kha95] Khalchukov, F.F. *et al.*, *Il Nuovo Cim.* 18C, N.5 (1995) 517.
- [Kok71] Kokoulin, R.P. and Petrukhin, A.A., in “Proceedings of the XII

- Intern. Conference on Cosmic Rays”, Vol. 6 (Hobart 1971) 2436.
- [Kol90] Kolb, E.W. and Turner, M.S., The Early Universe, Addison Wesley Company, 1990.
- [Kot69] Kotov, Y.D. and Logunov, V.M. in “Proceedings of the XI Intern. Conference on Cosmic Rays”, (Budapest 1969).
- [Kud99] Kudryavtsev, V.A. *et al.*, Phys. Lett. B 452 (1999) 167.
- [Kud00] Kudryavtsev, V.A. *et al.*, Phys. Lett. B 494 (2000) 175.
- [Kud03a] Kudryavtsev, V.A., private communication.
- [Kud03b] Kudryavtsev, V.A., private communication.
- [Kud03c] Kudryavtsev, V.A., private communication.
- [Kud03d] Kudryavtsev, V.A., Talk in Tecnomusiq Meeting, Paris, January 2003.
- [Lag91] Lagutin, A.A. *et al.*, in Proceeding of the 22nd Intern. Conf. on Cosmic Rays, Vol. 2 (Dublin 1991) 752.
- [Lee01] Lee, A.T. *et al.*, Astrophys. J. 561 (2001) L1.
- [Lip91] Lipari, P., Phys. Rev. D 44 (1991) 3543.
- [Lit52] Littler, D.J., Proc. Phys. Soc. London A 64 (1951) 638; A 65 (1952) 203.
- [Loh85] Lohmann, W., *et al.*, “Energy Loss of Muons in the Energy Range 1-10000 GeV”, Preprint CERN 85-3, 40.
- [Lvd94] LVD Collaboration, Nucl. Phys. (Proc. Suppl.) B35 (1994) 240.
- [Mad01] Madland, D., private communication.
- [Maj02] <http://majorana.pnl.gov>
- [McK01] McKinney, G., private communication.
- [Meu99] Meunier, P. *et al.*, Appl. Phys. Lett. 75 (1999) 1335.
- [Moh98] Mohr, J. *et al.*, Astrophys. J. 517 (1998) 627.
- [Mor01] Morales, A. *et al.*, Phys. Lett. B 532 (2002) 8; hep-ex/0110061.
- [Net02] Netterfield, C.B. *et al.*, Astrophys. J. 571 (2002) 604.
- [Oot99] Ootani, W. *et al.*, Phys. Lett. B 461 (1999) 371; hep-ex/9903034.
- [Pad01] Padin, S. *et al.*, Astrophys. J. 549 (2001) L1.

- [Pec77] Peccei, R.D. and Quinn, H.R., Phys. Rev. Lett. 38 (1977) 1440.
- [Pee93] Peebles, P.J.E., Principles of Physical Cosmology, Princeton University Press, Princeton, NJ, 1993
- [Per99] Perlmutter, S. *et al.*, Astrophys. J. 517 (1999) 517.
- [Per01] Percival, W.J. *et al.*, MNRAS 327 (2001) 129.
- [Pre02] Previtali, E., to appear in Proceedings of IDM2002 Conf., 4th Int. Workshop on Identification of Dark Matter, York-England, 2002.
- [Prö95] Pröbst, F. *et al.*, J. Low Temp. Phys. 100 (1995) 69.
- [Pry02] Pryke, C. *et al.*, Astrophys. J. 568 (2002) 26.
- [Raf95] Raffelt, G., hep-ph/9502358.
- [Ren97] Renault, C. *et al.*, Astron. & Atophys. 324 (1997) 69.
- [Rho93] Rhode, W., PhD. Thesis Univ. Wuppertal, 1993.
- [Rie98] Riess, A.G. *et al.*, Astron. J. 116 (1998) 1009.
- [Rin88] Rindi, A., Celani, F., Lindozzi, M. and Miozzi, S., Nucl. Inst. Meth. in Phys. Res. A272 (1988) 871.
- [Ros56] Rossi, B., "High Energy Particles", Prentice-Hall, Englewood-Cliffs, (1956).
- [Ros68] Rosenthal, I.L., Sov. Phys. Uspekhi 11 (1968) 49.
- [Rya66] Ryazhkaya, O.G, and Zatzezin, G.T., Proc. of the IX Intern. Conf. on Cosmic Rays, Vol.3, (London 1966) 987; Bezrukov *et al.*, L.B., Sov. Journ. Nucl. Phys., 17 (1973) 98.
- [Sal97] Salucci, P. and Persic, M., in ASP Conf. Ser. 117: Dark and Visible Matter in Galaxies and Cosmological Implication, (Brigham Young University, Provo, UT, 1997) p.1.
- [Sei98] Seidel, W. *et al.*, CRESST-Collaboration, J. Low Temp. Phys. 93 (1998) 247.
- [Sel96] Seljak, U. and Zaldarriaga, M., Astrophys. J. 469 (1996) 437.
- [Shi02] Shiozawa, M., to appear in Proceedings Neutrino2002 Conf., Munich-Germany, 2002.
- [Smi02] Smith, N.J.T. *et al.*, to appear in Proceedings of IDM2002 Conf., 4th Int. Workshop on Identification of Dark Matter, York-

- England, 2002.
- [Sno00] Snowden-Ifft, D., Martoff, C., and Burwell, J., Phys. Rev. D 61 (2000) 101301/1.
- [Sob70] Sobolevsky, N.M., The Code for Simulation of Nucleon-Meson Cascade in a Matter Using the Monte Carlo Method, JINR B1-2-5458, Dubna, 1970; Barashenkov, V.S., Sobolevsky, N.M., Toneev, V.D., Atom. Energy. 32 (1972) 123, 217.
- [Spo00] Spooner, N. *et al.*, UKDM-Collaboration, Phys. Lett. B 473 (2000) 330.
- [Ste84] Sternheimer *et al.*, Atomic Data and Nucl. Data Tables 30 (1984) 261.
- [Sto01] Stompor, R. *et al.*, Astrophys. J. 561 (2001) L7.
- [Tur99] Turner, M.S. and Tyson, J.A., Rev. Mod. Phys. 71 (1999) 145.
- [Tur02] Turner, M.S. astro-ph/0106035.
- [Tys95] Tyson, J. A. and Fischer, P., Astrophys. J. Lett. 446 (1995) L55.
- [Uda97] Udalski *et al.*, Acta Astronomica 47 (1997) 319.
- [Wal02] Waller, S., Diploma Thesis, Technische Universität München, 2002.
- [Wan01] Wang, Y.-F., *et al.*, Phys. Rev. D 64 (2001) 013012.
- [Wel02] Wellish, H.-P., private communication.
- [Wes79] West, D., Ann. Nucl. energy 6 (1979) 549.
- [Whi93] White, S.D.M., *et al.*, Nature 366 (1993) 429.
- [Xen02] <http://www.astro.columbia.edu/~lxe/XENON>
- [Yah86] Yahil, A., Walker, T., and Rowan-Robinson, M., Astrophys. J. Lett. 30 (1986) L1.
- [Zat66a] Zatsepin, G.T. and Ryazhkaya, O.G, in Proceedings of the IX International Conf. on Cosmic Rays, Vol.3 (London 1966) 987.
- [Zat66b] Zatsepin, G.T. and Kuzmin, V.A., Sov. Phys. JETP Lett. 4 (1966) 78.

Acknowledgments

Expressing appreciation for the assistance and support given to an author in the finishing of his thesis is customary. I express my appreciation here not because it is customary to do so, but because if it were not for the following individuals and foundations, I would not be able to finish this thesis. They are “special”, and I thank them sincerely for the roles they played in bringing this thesis into completion.

First of all I would like to thank my *Doktorvater* Prof. Dr. Franz von Feilitzsch for giving me the opportunity to work at the institute and to participate in the CRESSST project. I have had the benefit of working in an international collaboration and gained priceless knowledge and experience. I want also to gratefully note his kindly concern for my works as well as my life as a foreign student.

My special thanks go to my *zweiter Betreuer* Dr. Josef Jochum, who will soon be Prof. Dr. Jochum, for his excellent supervision. His endless constructive input have had a major impact on this thesis. It was really a privilege for me to work with him. His willingness to discuss and readiness to help were of great value and are much appreciated.

I am grateful to the *Deutscher Akademischer Austausch Dienst* (DAAD) for the financial support during the course of my PhD programm.

Thanks to all members of the CRESSST collaboration, especially to Dr. Yorck Ramachers for helping me in getting started with the MCNP Code, Christina Cozzini at Max Planck Institut für Physik for informing some important data on the Gran Sasso rock and Federica Petricca at the same institute for showing how to get the FLUKA Code.

I thank all members of ETNo μ Siq (European Team for Neutron Simulation and Quantification) for any cooperation and discussion on the topic of neutron-induced background. I would like to thank Dr. Gilles Gerbier at the CEA-Saclay for the discussion on the low energy neutrons. Dr. Vitaly Kudryavtsev at the University of Sheffield deserves special thanks for his visit in Garching to help me with simulation of muon-induced neutrons and for giving me the permission to use some of the codes he wrote.

The data on the concrete in the experimental halls of the Gran Sasso Laboratory have been made available for the help of many persons. Christian Grieb has helped in getting some concrete samples from several places at the laboratory. Dr. Mathias Laubenstein has given me some old concrete samples from his “treasure”, which happened to be part of the concrete below the new location of the CRESST setup. Dr. Walter Potzel has introduced me to Dr. Harald Hilbig from the laboratory of the *Lehrstuhl für Baustoffkunde und Werkstoffprüfung* at the department of civil engineering, who then analyzed the concrete samples. *Herzlichen Dank!*

I must also thank Dr. Gregg McKinney at the Los Alamos National Laboratory for helping with fixing the error in MCNP4B in writing PTRAC, Dr. Sandra Parlati at the LNGS for helping with rebuilding MCNP4B on a Gran Sasso machine. I thank Dr. Winfried Zwermann at the *Gesellschaft für Anlagen- und Reaktorsicherheit* (GRS) in Garching for showing several tricks in simulations with MCNP. Thanks to Dr. Marianne Göger-Neff, Tobias Lachenmeier and Stefan Waller for installing MCNPX and FLUKA, and administrating the computer system at the institute.

I would also like to thank Prof. Dr. Nolte for the discussion on the production of low energy neutrons and also for giving me a copy of important papers on neutrons and muons.

I thank Dr. Robert Heaton for giving me his unpublished calculations on the neutron yield in several elements. Thanks to Bryce Moffat for introducing me to him.

I also owe a debt of gratitude to the *Leids Kerkhoven-Bosscha Fonds* (LKBF) in the Netherlands for the travel grants I received for attending several conferences relevant to my thesis.

I am indebted to Dr. Wolfgang Rau for providing me with insightful and useful comments on an earlier draft of the thesis and also for correcting my poor English. Michael Stark and Jean-Côme Lanfranchi have helped with German translation of my annual reports to the DAAD and therefore indirectly secured my “*Kohle*”. Thanks a lot, guys!

I am also thankful to the E15 secretary Beatrice van Bellen as well as the SFB secretary Alexandra Füldner for their support in administrative matter. I thank Beatrice also for helping with some German and English translations.

Thanks to my roommate in office Michael Huber for giving several tips to deal with the daily life in Munich. Thanks also for all other “Cryos” for any kind of help.

My brothers and sisters in the *Bibelkreis* “*Integrität*” deserve many thanks for all of their brotherly love, support and prayers. Special thanks to Vicky Samuel and Josia Rastandi for lending me her CPU and his scanner, that were so helpful for me.

I thank my friend since high school Cecilia Nugraheni at the *Lehrstuhl für Informatik* of the Ludwig Maximillian Universität for several tips in L^AT_EX and of course for our unceasing friendship.

My sincere thanks to my mother, father, sister, brothers and in-laws, whom I always long for during my stay abroad, for their constant prayer, love and encouragement.

The last and very special thanks go to my beloved husband Ageng, who understands me like no other, for his unconditional support and incredible patience during the long period of finishing this thesis.

*I do not feel like an allien in this universe.
- Freeman Dyson,
Disturbing the Universe -*